

Structural investigation and macroscopic properties of amorphous metals

Dissertation zur Erlangung des Doktorgrades an der Fakultät
für Mathematik, Informatik und Naturwissenschaften
Fachbereich Physik der Universität Hamburg

vorgelegt von

Jana Gamcová

aus

Sabinov, Slowakische Republik

Hamburg

2018

Deckblatt

Gutachter/innen der Dissertation:	Mgr. Jana Gamcová
Zusammensetzung der Prüfungskommission:	Hermann Franz Christian Schroer Wilfried Wurth Ralf Rohlsberger
Vorsitzende/r der Prüfungskommission:	Daniela Pfannkuche
Datum der Disputation:	08.10.2018
Vorsitzender Fach-Promotionsausschusses PHYSIK:	Prof. Dr. Wolfgang Hansen
Leiter des Fachbereichs PHYSIK:	Prof. Dr. Michael Potthoff
Dekan der Fakultät MIN:	Prof. Dr. Heinrich Graener

Analytical page

Author	Jana Gamcová
Title	Structural investigation and macroscopic properties of amorphous metals
Language	English
Type of work	PHD thesis
Pages	121
Acquisition Title	PhD
University	Hamburg University
Faculty	Fakultät für Mathematik, Informatik und Naturwissenschaften
Place of realization	DESY-Deutsches Elektronen Synchrotron
Supervisor	Wilfried Wurth
Co-Supervisor	Ralf Rohlsberger
Co-Supervisor	Hermann Franz
Consultant	Jozef Bednarčík
Consultant	Ondrej Milkovič, Gaurav Mohanty and Štefan Michalik
Date of submission	2018
Date of Defence	08.10.2018
Keywords	X-ray, nano-indentation, strain-fields

Affidavit

I hereby declare that I wrote this thesis on my own and without the use of any than the cited references and aids.



Jana Gamcová

In Košice: 12.02.2018

Eidesstattliche Versicherung

Hiermit versichere ich an Eides statt, die vorliegende Dissertationsschrift selbst verfasst und keine anderen als die angegebenen Hilfsmittel und Quellen benutzt zu haben. Die eingereichte schriftliche Fassung entspricht der auf dem elektronischen Speichermedium. Die Dissertation wurde in der vorgelegten oder einer ähnlichen Form nicht schon einmal in einem früheren Promotionsverfahren angenommen oder als ungenügend beurteilt.



Jana Gamcová

Košice den 12.02.2018

Abstract

The structural investigation at the nano- and micro- level is the main tool to understand the behaviour of matter and to prepare new materials with even more superior properties. A novel in-situ synchrotron X-ray nano-diffraction approach for characterization and visualization of strain fields induced by nano-indentation applied to amorphous materials is introduced. The combination of those complementary methods offers the opportunity to obtain a quite complete picture about the atomic structure of investigated systems and the distribution of the strain fields. This method combines controlled deformation of a sample during constant observation of its structure (by X-ray). This offers us a direct way to correlate mechanical and structural properties of materials. This will patch a hole in the field of brittleness research of BMGs and so contributes to a better understanding of deformation processes. Several experiments on different experimental stations were performed.

- Ex-situ nano-indentation experiments have shown that spatially resolved X-ray matrix scans with a nano-meter sized beam can identify the positions of the indents and quantitatively describe the strain state after nano-indentation.
- In-situ nano-indentation experiments were performed using a monochromatic highly focused sub-micron X-ray beam on bulk metallic glass during nano-indentation. Performing fine grid scans on the BMG sample beneath the indenter revealed the elastic strain field in the deformation zone. It represents, to the best of our knowledge, the first experimentally observed map of elastic strains in a bulk metallic glass sample during nanoindentation obtained using real in-situ load-conditions.

Contents

Abstract	5
Contents	6
Goals of the dissertation thesis	9
Introduction	10
Part 1 Theoretical background	11
1.1 Bulk Amorphous Metals	12
1.1.1 History of Metallic Glasses and their reinvention to BMG	13
1.1.2 Criteria for creating BMG	16
1.1.3 Thermodynamic characterization of BMG	18
1.1.4 Properties of Metallic Glasses	20
1.1.4.1 Magnetic Chemical and Acoustic properties of BMG	20
1.1.4.2 Mechanical properties of BMG	21
1.1.5 Investigation in the field of BMG and industrially applications	25
1.2 Indentation	29
1.2.1 Test procedure and factors affecting the nanoindentation	30
1.2.2 Tip geometry	32
1.2.3 Strain, classification and Deformation Tensor from the mechanical viewpoint	34
1.3 Introduction to Finite Element Method analysis	37
1.4 Synchrotron Radiation and X-ray diffraction	39
1.4.1 Kinematical scattering on non-crystalline materials	41

Part 2 Evaluation Theory	45
2.1 Integration procedure	46
2.2 Fitting procedure	48
2.3 The influence of deformation on the diffraction pattern of an amorphous sample	50
2.4 Calculation of Deformation Tensor from the diffraction pattern of an amorphous sample	51
2.5 X-ray diffraction experiments	53
Part 3 Experiments	55
3.1 Samples	56
3.2 Experimental stations	57
3.3 Ex-situ experiment at end-station P06	58
3.4 Ex-situ experiment at end-station P02	62
3.5 ALEMNIS SEM – nanoindenter	69
3.6 In-situ experiment at end-station P03	71
3.7 In-situ experiment at end-station ID11	79
Discussion	87
Conclusion	98
Zusammenfassung	100
Outlook	101

Ausblick	103
Appendix	
A Acknowledgement	105
B Bibliography	106
C Nomenclature	111
D Brief user manual for SEM ALEMNIS Nanoindenter	114

Goals of the dissertation thesis

The main goal of the Dissertation Thesis was to find an appropriate method to study the correlation of mechanical and structural properties of amorphous materials. The method is demonstrated on Bulk Metallic Glasses (BMG). Employed methods are *X-ray diffraction* and *indentation*. Using X-ray photon beams in the nano- and micro- range we investigated structural changes occurring during the controlled deformation of a material with atomic resolution in micro-scale volumes. Such measurements are a big step in the field of understanding the relation between mechanical and structural properties of any material.

The partial tasks of PHD thesis were:

1. to perform X-ray diffraction measurements during the indentation on BMG
2. to develop a method for X-ray data evaluation and the correlation of structural and mechanical properties of the investigated material
3. to establish in-situ indentation experiments at beamlines at PETRA III, DESY - Hamburg as a common set-up which is available to PETRA III users

To demonstrate the potential and excellence of the proposed connection of indentation and diffraction technique bulk metallic glasses (BMG) were investigated. In the selection procedure of concrete prototypical samples emphasis was placed on highly relevant and nowadays investigated materials. An important criterion in the selection was also to follow the current focus of scientific work at DESY in the field of amorphous materials. Therefore, experiments were done on Zr-based BMG. This material was also selected for its practical reasons. Good knowledge how to prepare the optimal sample for the planned experiment

(exact chemical composition, shape of the sample, ...) as well as for the fundamental knowledge of the calculation of deformation zone under the loading element by Finite Element Method (FEM).

Introduction

There is a variety of interpretations of the meaning of the main key words of the presented thesis “amorphous”, “glass” and “metallic glass”. The term “amorphous” defines a non-crystalline body. “Glass” is a “hard, brittle substance that is cooled rapidly to prevent crystallization” [1]. By analogy, the term “metallic glass” usually refers to a metallic alloy rapidly quenched in order to “freeze” its structure from the liquid state. A metallic glass is therefore a metastable alloy, which lacks the symmetry typical for crystalline materials and at room temperature it shows an amorphous liquid-like structure.

The mechanical properties of metallic glasses are in many cases superior to those of their crystalline counterparts. Metallic glasses exhibit outstanding strength, elastic strain and elastic energy storage that, together with their superior corrosion resistance, make them interesting candidates in many structural applications (sporting goods, precision gears, optical mirror devices, fuel cells...).

However, despite their high fracture strength, after yielding most metallic glasses tend to fracture in a brittle manner, with almost total lack of plasticity, restricting their use in many applications.

Deformation in metallic glasses does not occur through slip systems and dislocation modes as in crystalline materials. Instead, metallic glasses suffer work softening as a consequence of extreme localization of plastic strain into narrow shear bands. The formation of multiple shear bands, so that strains are not concentrated in one or few shear bands, can avoid the premature failure observed in metallic glasses.

The correlation of mechanical and structural properties of BMG is the main topic of the work presented in this Thesis.

Part 1

Theoretical Background

This chapter, divided into three main sub-chapters, offers theoretical insight to the methods employed in this PHD work. The first sub-chapter will explain the structural state of amorphous metals and the principal conditions that must be fulfilled in order to retain the amorphous structure. The second sub-chapter will discuss synchrotron radiation sources, their history and necessities for the description of mechanical properties not only of amorphous materials. The last sub-chapter will offer an introduction to the indentation method, its pitfalls and unavoidableness in the field of mechanical properties of materials.

1.1 Bulk Amorphous Metals

A great number of amorphous alloys with different mechanical, chemical and thermodynamical properties has been produced within half a century since the first synthesis of an amorphous metallic phase in the Au-Si system by rapid solidification in 1960 [2]. Today, there are many ways how to divide BMGs into different groups/systems according certain criteria [3].

“Glass”, in this work, refers to an amorphous solid formed by rapid cooling of a liquid. A glass may be considered as a solid with frozen-in liquid structure. It means, glasses are structurally characterized by the absence of long-range order, but short-range order is present and may or may not be similar to that found in the crystalline counterpart. Thus a glass lacks three-dimensional atomic periodicity, which is characterized by a limited number of diffuse halos in X-ray, electron and neutron diffraction and low diffraction contrast in high-resolution electron microscopy [1]. Amorphous materials are not in an equilibrium state with respect to crystalline phase(s) and transform to the latter through nucleation and growth. Glasses are generally formed if upon cooling of a melt crystal nucleation and/or growth are avoided. At a temperature called glass transition temperature T_g the liquid freezes to a rigid solid without crystalline order. The physical, microscopic or atomistic transition occurs at temperature much above T_g . When the liquid alloy is cooled in a quasi-static manner, keeping thermodynamic equilibrium, at a melting temperature T_m it will become a crystalline solid. On fast cooling between T_{liq} and T_g the liquid behaves as an undercooled liquid and is thermodynamically and kinetically metastable. The main parameters, which characterize the glass-forming ability of the glassy state are the reduced glass transition temperature $T_{rg} = T_g/T_{liq}$ and the supercooled liquid region $\Delta T_x = T_x - T_g$, where T_x is the onset temperature of first-stage crystallization and T_{liq} is the terminal melting temperature [1].

The history of BMG, thermodynamic approaches for characterization of BMGs and their properties will be briefly described in the following lines.

1.1.1 History of Metallic Glasses and their reinvention to Bulk Metallic Glasses

Metallic amorphous alloys are comparative newcomers to the amorphous materials group. The formation of the first metallic glass of $\text{Au}_{75}\text{Si}_{25}$ was reported by Duwez at Caltech, USA, in 1960 [4]. He developed the rapid quenching techniques for cooling metallic liquids at very high rates of 10^5 – 10^6 K/s. In 1969, Chen and Turnbull formed amorphous spheres of ternary Pd-M-Si (with M = Ag, Cu, or Au) at critical cooling rates of 10^2 K/s to 10^3 K/s, specifically $\text{Pd}_{77.5}\text{Cu}_6\text{Si}_{16.5}$ with a diameter of 0.5 mm [5]. Turnbull in 1969 stated, that a liquid with $T_g/T_m = 2/3$ becomes very slow in crystallization and can only crystallize within a very narrow temperature range [6]. Such a liquid can be easily undercooled at a low cooling rate into the glassy state. This so-called Turnbull criterion is one of the rules for predicting the glass forming ability (GFA). To achieve the minimum cooling rate necessary for keeping the melt amorphous without precipitation of any crystals during the solidification has played an important role in the development of various MGs including BMGs. Early approaches towards fabrication of BMGs were mostly empirical in nature, but researchers gradually began to understand that the correct choices of elemental constituents would lead to amorphous alloys exhibiting critical cooling rates slower and slower which means that large pieces of metallic glasses can be fabricated. If one arbitrarily defines the millimeter scale as “bulk”, the first bulk metallic glass was prepared by Chen in 1974 [7]. His group used simple suction-casting methods to form one-millimeter-diameter rods of Pd–Cu–Si metallic glass at a cooling rate of 10^3 K/s. In the same year they obtained a critical casting thickness of 1 mm in Pd-M-P (M = Ni, Co, Fe) and a slightly greater thickness with $\text{Au}_{55}\text{Pb}_{22.5}\text{Sb}_{22.5}$. In the early 1980s, Turnbull and his group produced glassy ingots of $\text{Pd}_{40}\text{Ni}_{40}\text{P}_{20}$ with a diameter of 5 mm using surface etching followed by heating and cooling cycles. By processing in a boron oxide flux, they increased the critical casting thickness to 1 cm [8]. This started the development of a variety of solid-state amorphization techniques, which are based on completely different mechanisms from rapid quenching, mechanical alloying and diffusion induced amorphization in multilayers, ion beam mixing, hydrogen absorption to inverse melting. Employing these

techniques a variety of metallic glasses in the form of thin films or powders were obtained. Also, the expensive elements like Pd, Pt and Au in BMGs started to be replaced by less expensive and more compatible with nature ones like Zr, Ti, Ni and La. Progress has been most significant in the eighties, when Akihisa Inoue, of Tohoku University's Institute for Materials Research, and William L. Johnson of Caltech discovered strongly glass forming multicomponent La-, Mg-, Zr-, Pd-, Fe-, Cu-, and Ti-based alloys with large undercooling and low critical cooling rates of 1 K/s to 10^2 K/s. These critical cooling rates allow an increase in the critical casting thickness to more than 1 cm by conventional moulding. In 1988, Inoue discovered that La-Al-M (M = Ni, Cu) is highly glass-forming while investigating the mixing of rare earth materials such as lanthanides with Al and ferrous metals [9]. Using Cu moulds, they cast glassy $\text{La}_{55}\text{Al}_{25}\text{Ni}_{20}$ up to 5 mm thick and glassy $\text{La}_{55}\text{Al}_{25}\text{Ni}_{10}\text{Cu}_{10}$ up to 9 mm thick. In 1991 the same group developed glassy Mg-Cu-Y and Mg-Ni-Y alloys with the largest glass-forming ability obtained in $\text{Mg}_{65}\text{Cu}_{25}\text{Y}_{10}$ and they developed a family of Zr-based Zr-Al-Ni-Cu alloys having a high glass-forming ability and thermal stability. The critical casting thickness in these alloys ranged up to 15 mm for the alloy $\text{Zr}_{65}\text{Al}_{7.5}\text{Ni}_{10}\text{Cu}_{17.5}$ [10] [11]. The development of numerous new alloys demonstrated that bulk metallic glass compositions were not a laboratory curiosity and could be quite interesting for engineering applications. The Johnson group from Caltech started the search for bulk metallic glass compositions in the nineties. In 1993, Peker and Johnson developed, as part of a US Department of Energy and NASA funded project to develop new aerospace materials, the quinary alloy $\text{Zr}_{41.2}\text{Ti}_{13.8}\text{Cu}_{12.5}\text{Ni}_{10}\text{Be}_{22.5}$ [$=(\text{Zr}_3\text{Ti})_{55}(\text{Be}_9\text{Cu}_5\text{Ni}_4)_{45}$], commonly referred to as Vitreloy 1 (Vit1), with a critical casting thickness of up to 10 cm [12]. This work together with the work of the Inoue group can be considered as the starting point for the use of bulk glassy materials in structural applications. In the next 10 years the properties of the alloy Vit1 were investigated extensively. In 1997, the Inoue group re-visited the $\text{Pd}_{40}\text{Ni}_{40}\text{P}_{20}$ alloy and replaced 30% Ni by Cu [13]. As a result, they developed an alloy with a critical casting thickness of 72 mm. The Pd-Cu-Ni-P family is the metallic system with the highest glass-forming ability known to date. Vit1 was the first commercial BMG. Variants include Vit2 ($\text{Zr}_{46.75}\text{Ti}_{8.25}\text{Cu}_{7.5}\text{Ni}_{10}\text{Be}_{27.5}$). More recently, Kündig at ETH Zürich has been investigating $\text{Zr}_{52.5}\text{Ti}_5\text{Cu}_{17.9}\text{Ni}_{14.6}\text{Al}_{10}$ Vitreloy 105 (Vit105) – one of the best glass-forming alloys. In April 2003 research aimed at increasing the concentrations of light elements such as Ti, Al, and Mg in environmentally safe, Be-free Zr-based alloys. The formation of such BMGs requires no fluxing or special processing treatments and can form bulk glass by conventional metallurgical casting methods. Some simple binary alloys such as CaAl, PdSi, CuZr and

CuHf BMGs with diameter up to 2 mm were produced [14] [15] [16] [17] [18]. The results show that ordinary and simple alloys could possess unusual high GFA, and the formation mechanism and criteria for the binary BMG may be different from that of multicomponent BMGs. The development of multicomponent alloys with exceptional glass forming ability continues. The progress depends to a large extent on the in-depth understanding of the formation mechanism and improvement of the preparation techniques. Hand in hand with the development of BMGs different studies of their mechanical properties were carried out.

1.1.2 Criteria for creating BMG

Starting with the first metallic glass developed by Duwez and others, the critical casting thickness increased by more than three orders of magnitude in the last 40 years. Currently, research in the area of bulk metallic glasses is growing significantly. Many groups are searching for new alloy compositions and investigate the mechanical, structural, thermophysical, and magnetic properties of these alloys.

The key empirical criteria [19] for slow crystallization kinetics and, therefore, a stable supercooled liquid state and high glass-forming ability are still ambiguous because different BMGs families have rather different properties. In general, BMG consist of three or more elements. The glass-forming ability in BMGs tends to increase as more components are added to the alloy. That is called the “confusion principle” which implies that a larger number of components in an alloy system destabilizes competing crystalline phases which may form during cooling. This effect frustrates the tendency of the alloy to crystallize making the melt more stable relative to the crystalline phases. Another criterion is the mismatch of atomic radii between individually elements in BMG. When the difference in radii is greater than 12% [20] it leads to a higher packing density and smaller free volume in the liquid state and requires a greater volume increase for crystallization. For example, the addition of beryllium, which is much smaller in size than zirconium, into a Zr-based alloy increases the GFA significantly and enlarges the thermal stability and hardness of the Zr-based BMG [21]. Negative heat of mixing between the main elements increases the energy barrier at the liquid-solid interface and decreases atomic diffusivity. This retards local atomic rearrangements and the crystal nucleation rate, extending the supercooled liquid temperature range. Using an alloy composition close to a deep eutectic forms a liquid stable at low temperatures. Slower crystallization allows a decreased critical cooling rate and enables stable bulk metallic glass formation and fabrication by conventional casting techniques [22].

The abovementioned ratio $T_{rg} = T_g / T_m$ is a key parameter for glass formation, and the homogeneous nucleation rate in the undercooled melt is a strong function of this parameter. If a liquid is cooled below the melting point, the free energy difference between the liquid and a

crystal provides a driving force for crystal nucleation. This results in an energy barrier that a local composition fluctuation needs to overcome in order to form a nucleus. To enable the growth of such a nucleus, atoms within the liquid need to be rearranged [2]. The Turnbull rules show that metallic glass formation can be achieved for T_{rg} as low as 0.62 [23].

The liquid behavior of bulk metallic glasses results in a reduced rate of both crystal nucleation and growth, and thus contributes greatly to the extraordinary glass-forming ability. Apart from T_{rg} , another extensively used parameter for GFA is $\Delta T_x = (T_x - T_g)$, which is equal to the difference between the onset temperature of the first crystallization (T_x) and the glass transition temperature (T_g). However, the comparison of GFA based on T_{rg} and ΔT_x do show significant discrepancies in some alloy systems. A refined parameter using T_x , T_g and the liquids temperature T_{liq} , $\gamma = T_x / (T_g + T_{liq})$ - gave better reference for judging the GFA among metallic glasses [19].

1.1.3 Thermodynamic characterization of BMG

There is a big effort to formulate an atomistic theory for describing the liquid - glass transition. Most material science treatments of the liquid – glass transition use two classical phenomenological approaches, the Free Volume Model and the Adam-Gibbs Theory.

Free Volume Model

In 1959 Cohen and Turnbull proposed the Free Volume Model derived from the theory of liquids [23]. Within the Free Volume Model particles are modelled like hard spheres moving in a cage formed by their nearest-neighbours. The volume inside the cage is partly occupied by the volume of the spheres and the remaining part is the free volume in which the particle and its neighbours can move. The "solid state" is characterized by particles which are imprisoned (immobilized) in their cages. In contrast the "liquid state" is characterized by free volume which is delocalized and diffusive motion is not restricted by neighbours at any time. Cohen and Turnbull postulated that the glass transition is connected to the localization of the free volume, and below a critical free volume transport is prohibited. The biggest imperfection of this theory is the fact that no local free energy is needed for free volume redistribution, so the modelled system is obviously in equilibrium, in contradiction to experiment. The suitability of the Free Volume Model was overestimated, since models of hard spheres with higher density still resemble a liquid state. In fact, the density of a liquid undergoing a liquid-glass transition is only changed by 6-10%, in contradiction to change of density of a solid undergoing a solid-glass transition is around 100 % [24]. Nevertheless, the concept of a confining cage made of neighbouring particles is instructive and is also used in later theories.

Adam and Gibbs Theory

In 1965 Adam and Gibbs introduced their theory based on the concept of cooperatively- rearranging-regions [25]. In a high-density and low-temperature state, particles

cannot move without others cooperating (to create or to fill a gap by moving a certain particle among other particles forming cooperatively rearranging regions) which means that the configurational degrees of freedom are reduced. Each cooperatively rearranging region consists of a number of particles sufficient for cooperative movement, and is supposed to have two possible configurational states. Each cooperatively-rearranging-region is able to change its configuration independently of its environment due to energy fluctuations. These assumptions lead to the conclusion that the size of the cooperatively rearranging regions is growing upon temperature decrease.

1.1.4 Properties of Bulk Metallic Glasses

BMGs are famous for their unique mechanical, physical and chemical properties [3]. These exceptional and unique qualities follow from the combination of certain properties of metallic alloys and intrinsic properties of glasses. This combination exhibits new properties, totally different in comparison to those achieved in the crystalline counterparts.

1.1.4.1 Magnetic, Chemical and Acoustic properties of BMG

Metallic glasses based on ferromagnetic elements usually also show ferromagnetic properties. Amorphous alloys exhibit soft magnetic properties.

BMGs have the following advantages in soft magnetic properties [26]:

- high electrical resistivity of 200–250 $\mu\Omega$ cm at room temperature;
- low coercive force below 1 A/m;
- high initial permeability;
- controllable arrangement of domain wall structure achieved by control of casting and/or cooling processes;
- good high-frequency permeability.

On the other hand, the disadvantages of BMGs are:

- high materials cost due to the necessity of using special solute elements to obtain a higher GFA;
- low saturation magnetic flux density due to the addition of large amount of solute elements.

The latter is a serious obstacle for future use for example in power transformers. Therefore, a lot of effort is still needed to develop BMGs with optimum soft magnetic properties. In contrast, BMGs obtained in multicomponent (Nd, Pr)–Fe-based systems have high coercivity [27] [28] [29]. The reason for the high coercivity is attributed to the presence of a relaxed

disordered structure that can be regarded as an ensemble of clusters with large random magnetic anisotropy [30] [31] [32]. High coercivity was not observed in annealed ribbons. Nd-based BMGs can actually be regarded as a type of clustered amorphous material. These BMGs exhibit hard magnetic properties while melt-spun ribbons with the same composition are magnetically soft [33]. The mechanisms responsible for the hard-magnetic properties of the (Nd, Pr)-Fe-based BMGs and the relationship between microstructure and magnetic properties are still not clear. The rare-earth-rich Fe-based metallic glasses, in which clusters may exist, did not show hard magnetic properties at room temperature, irrespective of the quenching rate applied for solidification. Paramagnetic behaviour at room temperature, in case of the presence of Nd–Co clusters is also possible. Since 1995, a series of Fe- and Co-based BMGs with ferromagnetism at room temperature has been developed by copper mould casting or water quenching [26] [34] [35]. The formation and properties of multicomponent Fe-based BMGs have attracted increasing attention because of the fundamental interests in their properties and industrial application potential.

The most important chemical property which renders BMG unique among other materials is their chemical homogeneity. The defect-free structure results in good corrosion resistance to different environments which predetermine them to be very suitable for biological implants [3].

The studies of the acoustic, elastic and thermal properties of metallic glasses can provide important information about the structural and vibrational characteristics [36] [37] [38]. The geometry of conventional metallic glasses, very thin ribbons or wires, makes the studies of the intrinsic nature of the glass and the glass transition as well as the measurements of many physical properties very difficult. The experimental data about acoustic and elastic properties in metallic glasses are scarce, and the vibrational features in metallic glasses are poorly understood. However, BMGs are suitable for measurements of elastic wave propagation. The excellent wave absorption ability of for example Zr-based BMG composites originates from the random dispersion of residual carbon nanotubes and ZrC phase, the formation of new interfaces, and the denser packed structure in the glass matrix of the composites [39]. This work shows that the composites might have potential of application in the field of shielding acoustic sound or environmental noise.

1.1.4.2 Mechanical properties of Bulk Metallic Glasses

Fundamental mechanical properties of bulk glassy alloys play a crucial role in their application area, therefore a lot of studies are focusing on introducing and improving the glassy phase. The glassy alloys have good micro-forming ability in supercooled liquid region and much larger elastic strain and show much lower Young's modulus. The difference in these values between glassy and crystalline alloys exceeds 60% [3]. Despite the lack of plasticity they can be used in many structural applications; metallic glasses manifest elastic deformation of more than 2% before yielding and they can absorb up to 30 times more elastic energy [40]. The significant difference between bulk glassy and crystalline alloys is connected with the difference in the deformation and fracture mechanisms. For studies of the materials mechanical behaviour under load condition, tensile and compression tests are usually used.

A sample with an initial length l_0 and a cross-section A subjected to an applied load P will suffer an elastic deformation followed by a plastic deformation regime until its rupture. The elastic regime can be described by Hooke law:

$$\frac{F}{A} = E \frac{\Delta l}{l_0} \quad \text{or} \quad \sigma = E \cdot \varepsilon$$

where E is the (elastic) Young modulus and Δl is the variation of the sample length during the testing. The ratio $F/A = \sigma$ is called stress or strength and it has the dimension of a pressure. The relative elongation $\Delta l/l_0 = \varepsilon$ is called strain. The tensile/compressive or Young's modulus E is usually measured at very low strains where the stress is proportional to the strain [41] [42].

Permanent, non-elastic deformation begins at the maximum engineering stress named elastic yield strength σ_e . The yield point is the first load at which the specimen yields, where the specimen cross-sectional area begins in tensile test to decrease or increase in case of compression test and a modification in strain occurs without a modification in stress. The maximal stress which a material can withstand before failing is named ultimate strength or fracture strength σ_f . The characteristic values of the strain for the yield point and fracture point are named yield strain ε_e and fracture strain ε_f , respectively [41] [42]. *Figure 1* shows a prototypical stress-strain curve.

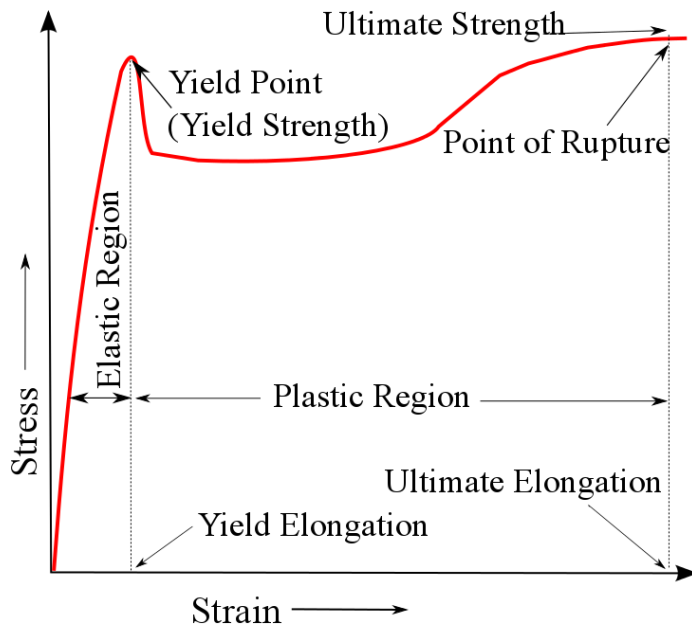


Figure 1:
Stress-strain curve displaying linear elastic region and plastic region characterized by yielding and finally fracturing.

Yield Point (strength)	Yield point is the first point (load) at which the specimen yields. This is when the specimen's cross-sectional area begins to change.
Modulus of Elasticity	The ratio of stress to strain within the elastic region of the stress-strain curve
Yield Elongation	The strain at the yield point
Elastic Region	The portion of the curve before the yield point
Plastic Region	The portion of the curve after the yield point
Ultimate (tensile) strength	Ultimate tensile strength is the maximum stress a material can withstand before failing,
Ultimate elongation	The total elongation just before fracture

The resistance of a metal to plastic deformation is named hardness and it is usually determined by indentation. Hardness is one of the most intuitive properties of materials. Its precise definition depends on the method of the measurement, which will determine the scale of the hardness obtained [1]. Indentation testing is describing in more details in Chapter 1.2

Indentation.

With the development of techniques like indentation, pressure is becoming an important processing variable just like temperature or chemical composition for condensed matter studies. Pressure can cause a large change of atom spacing and chemical bonding and has been found to be a powerful tool for affecting and controlling the nucleation and growth in metallic glasses [43] [44]. For example, since pressure can promote local atomic rearrangements, BMGs can be crystallized under high pressure to very fine-grained nanostructured material. Extensive studies of the crystallization behaviours under high pressure have been performed for gaining insight into the mechanism of the nucleation and growth processes in BMGs [45] [46] [47] [48] [49] [50]. The pressure treatment conditions, such as heating or cooling rate, annealing time at each annealing temperature should be considered when comparing different crystallization behaviours of the BMG under high pressure. Applying high pressure during the solidification process of a glass-forming alloy can therefore improve the GFA, and provide a useful way to study the formation mechanism of BMGs [43] [48].

Plastic deformation in metallic glasses is generally associated with inhomogeneous flow in highly localized shear bands. The localization of shear is associated with possible strain-softening mechanisms and thermal softening as well as the absence of strain-hardening (work hardening) mechanisms. The high elastic strain limit combined with a high yield strength and fracture toughness make metallic glasses ideal for applications where the storage of high densities of elastic energy is needed. This property has led to the use of bulk metallic glasses in golf-club heads, high-performance springs, etc [51].

1.1.5 Investigation in the field of BMG and industrial applications

Compared with the numerous reports on alloy compositions and properties, there are only a few published results on industrial processing of BMGs [3] [22] [51] [52] [53]. In most of the commercially available BMG products, vacuum die-casting is used for producing the desired shapes of the components. BMG usually requires fast cooling for retaining the amorphous structure, therefore their casting to very thin and intricate shapes as well as very large work pieces are difficult and very expensive. In addition to casting, forming BMG parts through viscous flow in the supercooled liquid state is also a viable process. Due to the high formability of BMG, like Zr-based BMG, not only common small machine components can be fabricated, but micro-machine components can be made through micro-forming as well. With the unique and unconventional characteristics BMG materials are adopted for application in various fields. One of the great advantages of BMGs is the ease of formation of complicated shapes. For example Zr-based BMGs found application in industry 3 years after their invention [3].

Table 1.

Properties of BMG with appropriate application field [3] [22] [51] [54]

Property	Application field
High reflection ratio	jewelry, optical precision materials
Different formability	jewelry, electronic components, medical and surgery tools, machinery structural materials, tool materials, bonding materials, biological implants, surgery tools
High manufacturability	jewelry, medical and surgery tools, machinery structural materials, cutting materials, tool materials, bonding materials, biological implants, surgery tools
High corrosion resistance	jewelry, medical and surgery tools, machinery structural materials, cutting materials, tool materials, bonding

	materials, biological implants, surgery tools
High wear resistance	jewelry, medical and surgery tools, machinery structural materials, cutting materials, tool materials, bonding materials, biological implants, surgery tools
Soft magnetic property	soft magnetic devices which can be easily magnetized and demagnetized
Low energy absorption	sporting goods, machinery structural materials, cutting materials, tool materials, bonding materials, biological implants, surgery tools
High elastic energy	sporting goods, machinery structural materials, cutting materials, tool materials, bonding materials, biological implants, surgery tools
High strength	sporting goods, machinery structural materials, cutting materials, tool materials, bonding materials, biological implants, surgery tools
High hardness	sporting goods, machinery structural materials, cutting materials, tool materials, bonding materials, biological implants
High fracture toughness	sporting goods, machinery structural materials, tool materials, bonding materials, biological implants, surgery tools
High impact fracture energy	sporting goods, machinery structural materials, tool materials, bonding material, biological implants, surgery tools
High fatigue strength	sporting goods, machinery structural materials, bonding materials, biological implants, surgery tools
High hydrogen storage capacity	hydrogen storage materials
High frequency permeability	high magnetostrictive materials
High viscous flow-ability	composite materials
High acoustic attenuation	acoustic absorption materials
Self-sharpening property	penetrator, cutting materials, surgery tools

The most interest in the field of industry is devoted to lightweight and inexpensive Zr-based BMGs, like Vitreloy (Zr-Ti-Cu-Ni-Al), which was developed for structural applications by a California Institute of Technology (CALTECH) research team, now marketed by Liquidmetal Technologies [51]. Zr-based BMGs are being investigated for aerospace applications by the Universities of Virginia (materials discovery) and Connecticut (process development), Pratt & Whitney (materials characterization and design), Boeing (applications), US Air Force and Defence and aerospace [55]. Under a contract of the US Army Research Office, for example, researchers in the USA are developing a manufacturing technology for metallic-glass tank-armor penetrator rounds to replace the current depleted uranium penetrators, which are suspected of biological toxicity [22] [51]. NASA's Genesis spacecraft has received its final piece of science equipment: a solar wind collector made of a new formula of bulk metallic glass. Liquidmetal Technologies has received a series of contracts from US Department of Defence to develop military materials that are stronger, lighter, and more effective at high temperature and stress [52].

From 1997, Zr-based BMGs are used as golf club heads because they are twice as hard and four times as elastic as Ti drivers, 99% of the impact energy from a BMG head is transferred to the ball (compared to 70% for Ti). Vitreloy is used since 2003 also in tennis rackets, because the increased stiffness enhances the energy return with 29% more power [51].

Vitreloy can also be used for watch cases to replace Ni and other metals, which can cause allergic reactions. Luxury watchmakers like TAG Heuer have a special edition "Microtimer Concept Watch" where Vitreloy is used. BMGs can achieve a stunning surface finish which catches the attention of high-end jewelry makers worldwide. The high-performance characteristics and unique properties of BMG can create a metal surface that is both exceptionally hard and scratch resistant, but can be polished to a high luster that is maintained over time [22] [53].

Vitreloy is used in medical applications due to its biocompatibility. It is nonallergenic, has perfect wear-resistance and does not corrode. For example, DePuy Orthopaedics, Inc. is using the material in knee-replacement devices. In 2002, Surgical Specialties began producing ophthalmic scalpel blades using Vitreloy. They are higher quality but less expensive than diamond, sharper and longer lasting than steel, and more consistently manufacturable, since they are produced from a single mold (with micro-scale casting accuracy) ready for use [56].

In order to better integrate the BMG components into the structure of machines and/or other products, the possibility of joining BMGs with another BMG or crystalline materials is desirable. The major contribution in this aspect was the demonstration of welding processes

[57] [58] [59] [60] [61]. The major consideration while welding BMGs is whether the glassy state can be retained after the processes, which usually involves the supply of heat for softening the metallic glasses. The results confirm that with careful control of the process parameters, the joints remain amorphous and the strength is comparable to the bulk of the metallic glass [62].

The development of Fe-based BMGs has reached the final stage for application as soft magnetic materials for common mode choke coils. With the trend of miniaturization of personal electronic devices such as MP3 players and personal digital assistants, there is a pressing need to make the casing thinner while retaining sufficient mechanical strength. Mobile phones and digital still cameras with BMG casing are already developed [51].

1.2 Indentation

Indentation is a technique for measuring the local mechanical properties (initially mostly hardness) of a material. For more than hundred years, engineers and metallurgists have been making hardness measurements of metals as a means of assessing their mechanical properties. The hardness of a material means the resistance of the material to local deformation. Usually a hard indenter tip is pressed into the surface of the material with a known load and size of the tip [63] and the penetration depth is recorded as a function of applied force (load-displacement curve).

Nanoindentation is now a common tool for the measurement of mechanical properties at small scales and may have even greater importance as a technique for experimental studies of fundamental physics. With high-resolution load-displacement readings during a nanoindentation test discrete incidents like phase transformations or nucleation of grains can be detected. In general, the goal of the majority of nanoindentation tests is to extract the elastic modulus and hardness of the specimen material from load-displacement data [63].

1.2.1 Test procedure and factors affecting the nanoindentation

Hardness tests are widely carried out to classify materials. It is mechanical test, easy to perform and can be used to determine the suitability of a material for a given purpose (description of material, checking the uniformity of a product, assessing the success of a heat treatment and so on). As mentioned, the principal goal of nanoindentation testing is to extract elastic modulus and hardness of the specimen material from experimental readings of the applied load P versus depth of the penetration. In a typical test, force and depth of penetration are recorded as load is applied from zero to some maximum force and then from maximum force back to zero.

The indentation elastic modulus E^* is usually determined from the slope dP/dh_{max} of the unloading curve at maximum load. E^* is a function of dP/dh_{max} and the area of contact A [63]:

$$E^* = \frac{1\sqrt{\pi}}{2\sqrt{A}} \frac{dP}{dh_{max}}$$

The indentation hardness H is in general calculated from the indentation load divided by the contact area:

$$H = \frac{P}{A}$$

In practice, nanoindentation testing is performed on a wide variety of substances, from soft polymers to diamond-like carbon thin films. The shape of the load vs. displacement curve [Fig.2] is often found to be a rich source of information, not only for providing a means to calculate modulus and hardness of the specimen material, but also for the identification of phase transformations and cracking.

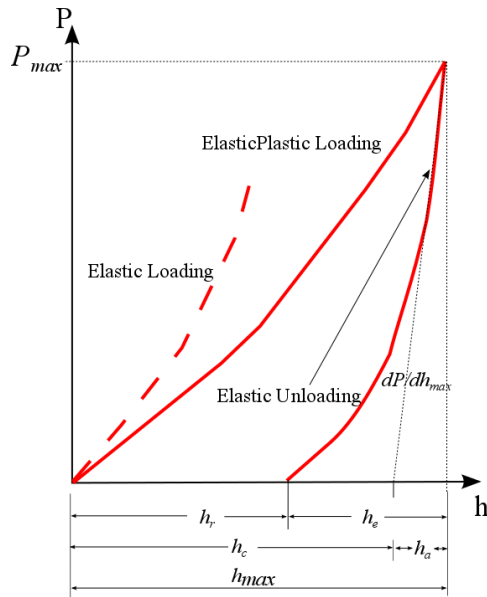


Figure 2:

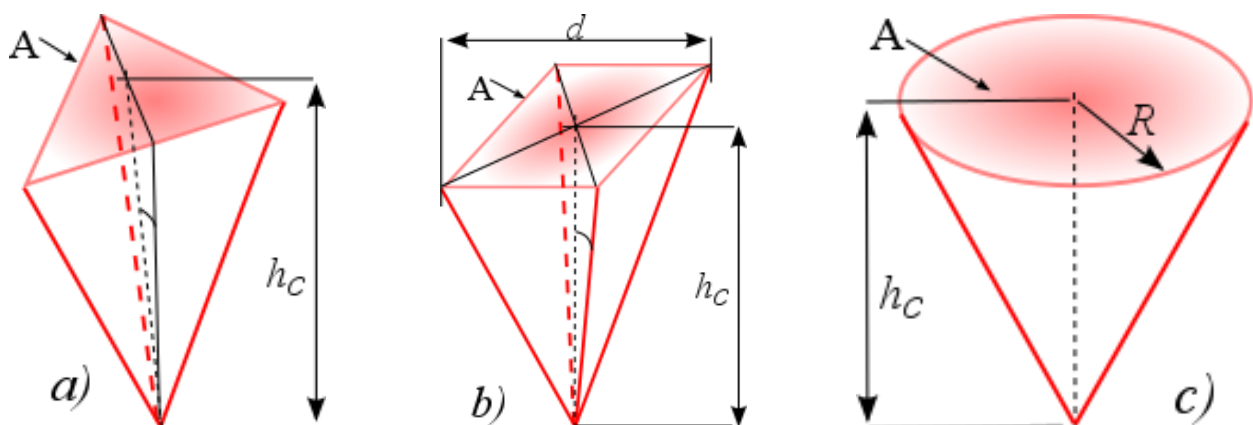
Load vs. displacement curve for elastic-plastic loading followed by elastic unloading. h_r is the depth of the residual impression, h_{max} is the depth from the original specimen surface at maximum load P_{max} , h_e is the elastic displacement during unloading, h_c is the elastic displacement for an equivalent punch, and h_a is the distance from the edge of the contact to the specimen surface at full load.

The indentation test procedure involves a loading sequence followed by unloading. The loading part usually consists of an initial elastic contact, followed by plastic flow or yield. Upon unloading, if yielding has occurred the load vs. displacement curve follows a different path until at zero applied loads, a residual impression is left in the specimen surface. The calculation of hardness and Young's modulus means to estimate the maximum depth of penetration, together with the slope of the unloading curve measured at the tangent to the data point at maximum load. It is important to note that the validity of nanoindentation data depends largely upon the analysis procedure used to process the raw data which are affected by various systematic errors. The most commonly encountered measurements artefacts are briefly explained below. Those errors must be corrected to obtain consistent nanoindentation values [64].

1.2.2

Indenters can generally be classified into three categories – sharp, spherical or blunt. The criteria, upon which a particular indenter is classified are mostly subject of opinion. Nanoindentation hardness tests are generally made with either spherical or pyramidal indenters.

The Berkovich indenter [Fig.3a] is generally used in small-scale indentation studies. The Berkovich indenter, a three-sided indenter, has the advantage that its edges are very easily constructed to meet in a single point. It has a very flat profile, with a total included angle of 142.3° and a half angle of 65.35° , measured from the axis to one of the pyramid flats. The Vickers indenter [Fig.3b] is a square pyramid having opposite faces at an angle of 136° and edges at 148° and a face angle of 68° . The Vickers indenter is particularly useful for the study of very hard materials. The Wedge indenter [Fig.3c] is the most popular indenter geometry for measuring plane strain in brittle materials, like bulk amorphous glasses. It is an indenter of the sharp type and can have different wedge-angles. An indentation made by a wedge can be treated as a two-dimensional problem, provided the length is many times greater than the width, so that end effects are negligible. Conical indenters [Fig.3d] have the advantage to possess axial symmetry. Spherical indenters [Fig.3e] are finding increasing popularity, as this type of indenter provides a smooth transition from an elastic to an elastic-plastic contact. It is particularly suitable for measuring soft materials [63].



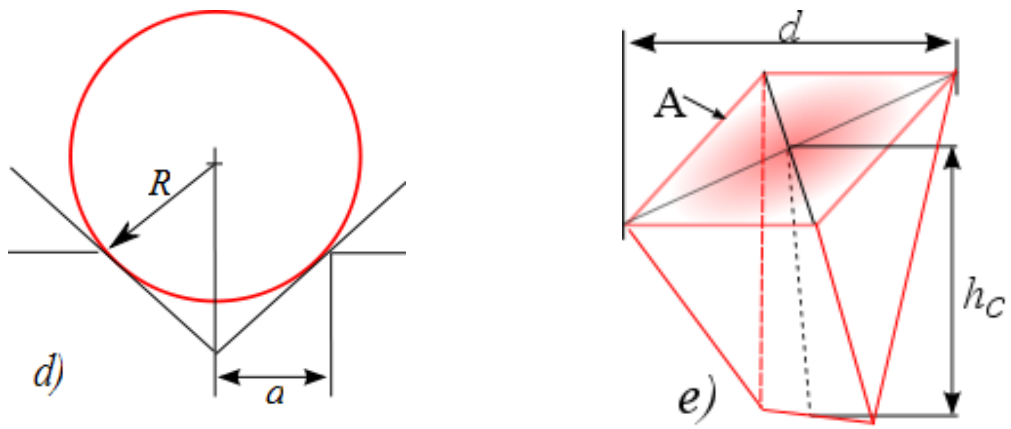


Figure 3: Types of indenters: a) Berkovich, b) Vickers, c) conical d) spherical e) wedge.

1.2.3 Strain, classification and Deformation Tensor from the mechanical viewpoint

Deformation in mechanics is the transformation of a volume element of material from a reference position configuration to a new position configuration, see *Figure 4*. A deformation may be caused by external loads, or changes in an inhomogeneous temperature field or chemical reactions. A strain is a description of deformation in terms of relative displacement of materials. In this work we consider deformation caused by external loads. The relation between external load (stress) and induced strain is expressed in elastic regime by Hooke's law:

$$\varepsilon = \frac{\sigma}{E} \text{ where } \varepsilon = \frac{\Delta l}{l} \text{ and } \sigma = \frac{F}{A}$$

where ε – strain, is the relative elongation (change in length), σ is the mechanical stress, E is the Young modulus or elastic modulus, F is the force which is deforming the material, A is the cross-sectional area. Deformations which are recovered after the external load has been removed are called elastic deformations. On the other hand, irreversible deformations remain even after the external load has been removed. Those are termed plastic deformations. Plastic deformation is characterized by a strain hardening region and rupture of material. During strain hardening the material becomes stronger through the movement of dislocations.

Simply said, stresses produce deformations because real materials are not infinitely rigid. Deformations are measured by strains. Strain is dimensionless and in structural mechanics it is often a very small number compared to one. Integration of strains through space gives displacements, which measure motions of the particles of the body (structure). Conversely, if the displacements are given as data (as will happen with the Finite Element Method), one can pass to strains by differentiation, from strains to stresses using material laws such as Hooke's law for elastic materials, and from stresses to internal forces.

Strain classification:

In general terms, strain is a macroscopic measure of deformation. Truesdell and Toupin, in their famous Classical Field Theories review article in *Handbuch der Physik* [65], introduce the concept as “The change in length and relative direction occasioned by deformation is called, loosely, strain.” [The term “strain” was introduced by W. J. M. Rankine in 1851.].

1. Average strain is taken over a finite portion of the body. Point strain is obtained by a limit process in which the dimension(s) of the body approach zero.
2. Normal strain measures changes in length along a specific direction. It is also called extensional strain as well as dimensional strain. Shear strain measures changes in angles with respect to two specific directions.
3. Mechanical strain is produced by stresses. Thermal strains are produced by temperature changes.
4. Finite strains are obtained using exact measures of the change in dimensions or angles. Infinitesimal (linearized, small) strains are obtained by linearizing the finite strain measures with respect to displacement gradients.

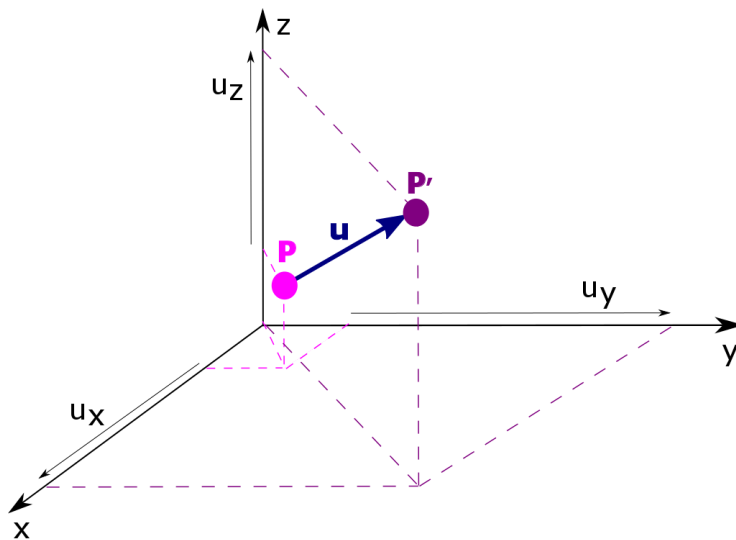


Figure 4:

Displacement of P to P' by displacement vector \mathbf{u} . Displacement vector $\mathbf{u}(x, y, z)$ is given by three elements: $\mathbf{u}(x, y, z) = [\mathbf{u}_x(x, y, z); \mathbf{u}_y(x, y, z); \mathbf{u}_z(x, y, z)]$.

Using X-rays diffraction, the elastic deformation on amorphous materials can be detected. In this work we are interested in the local elastic deformation (caused by indentation) which acts on a volume element. Thus we can define the local strain ϵ by the nine components of the strain tensor. These are directly given in terms of the first derivatives of the displacement components $\mathbf{u}(x, y, z) = [\mathbf{u}_x(x, y, z); \mathbf{u}_y(x, y, z); \mathbf{u}_z(x, y, z)]$. We obtain the normal strain

as the diagonal elements of the strain tensor: $\epsilon_{xx} = du_x/dx$; $\epsilon_{yy} = du_y/dy$; $\epsilon_{zz} = du_z/dz$. The shear strains are contained in the remaining part of the tensor: $\epsilon_{xy} = 1/2(du_x/dx + du_y/dy)$; $\epsilon_{yz} = 1/2(du_y/dy + du_z/dz)$; $\epsilon_{zx} = 1/2(du_z/dz + du_x/dx)$. The normal strains simply represent the fractional change in length of elements parallel to x , y , and z axes respectively. The physical meaning of the shear strains is shown in *Figure 5*. Shear strains measure changes of angles as the material deforms in response to shear stress. To define shear strains it is necessary to look at two directions that form the plane that undergoes shear distortion.

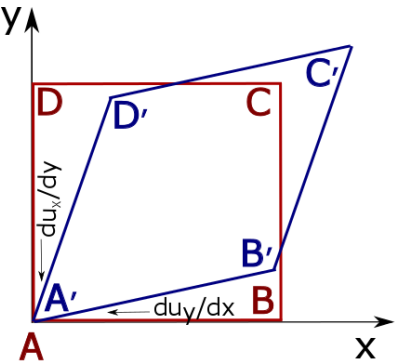


Figure 5:
 A small area element ABCD in the xy plane has been deformed to the shape A' B' C' D' without change of area. The angle between the sides AB and AD, initially parallel to x and y , respectively, represents the shear strains of the tensor: $\epsilon_{xy} = 1/2(du_x/dx + du_y/dy)$.

1.3 Introduction to Finite Element Method analysis

For a long time, the theoretical analysis of mechanical systems has been based on continuous differential equations and took into account basic physical principles such as equilibrium, conservation of energy, conservation of mass, the laws of thermodynamics, Maxwell's equations and Newton's laws of motion. The basic concept of the finite element method (FEM) is the subdivision of the mathematical model into non-overlapping components of simple geometry called finite elements. Here we offer only very short summary of FEM, more or less philosophy of this method, for more detail see [66].

The response of each finite-element is expressed like a finite number of degrees of freedom characterized as the value of an unknown function. The response of the mathematical model is then approximated by that of the discrete model obtained by connecting or assembling the collection of all elements.

A typical finite element analysis using a software system requires the following information: spatial locations of nodal points, elements connecting the nodal points, properties of the material, conditions and restraints of boundaries, loading function details, options of analysis. Because FEM is a discretization method, the number of degrees of freedom is necessarily finite. They are collected in a vector called state vector.

The mechanical properties of a material in a finite element model are obtained by minimizing an energy functional. This energy functional consists of all the energies associated with the particular finite element model. Based on the law of conservation of energy, the finite element energy functional must equal zero. Thus, the basic equation for finite element analysis is: *energy functional/grid point* = 0. The grid point is unknown and has to be calculated. This calculation is based on the principle that if a particle is in equilibrium characterized by a set of forces, then for any displacement, the virtual work is zero. For each finite element the energy functional needs to be calculated.

In stress analysis, the equations for a homogenous solid material can be obtained by minimizing the total potential energy of the system. The total potential energy Π , which consists of partial potential energies of the finite elements can be expressed as:

$$\Pi = \frac{1}{2} \int_{\Omega} \sigma^T \varepsilon dV - \int_{\Omega} u^T b dV - \int_{\Gamma} u^T q dS$$

where σ is vector of the stress, ε is vector of strain, u is the vector of displacements, b is the vector of body force component per unit volume, and q is the vector of applied surface traction. The first term on the right represents the internal strain energy and the rest terms represent potential energy contributions of the body force loads and distributed surface loads. In FEM, the displacements have known values only at the nodal points. The variation within the elements is described by interpolation functions. The total potential energy of the discretized structure will be at the end the sum of the energy contributions of each individual element.

1.4 Synchrotron radiation and X-ray diffraction

Synchrotron radiation was named after its discovery in a General Electric Synchrotron Accelerator built in 1946 and announced in May 1947 by Frank Elder, Anatole Gurewitsch, Robert Langmuir, and Herb Pollock in a letter entitled "Radiation from Electrons in a Synchrotron" [67].

On April 24, Langmuir and I were running the machine and as usual were trying to push the electron gun and its associated pulse transformer to the limit. Some intermittent sparking had occurred and we asked the technician to observe with a mirror around the protective concrete wall. He immediately signaled to turn off the synchrotron as "he saw an arc in the tube." The vacuum was still excellent, so Langmuir and I came to the end of the wall and observed. At first we thought it might be due to Cherenkov radiation, but it soon became clearer that we were seeing Ivanenko and Pomeranchuk radiation.

Pollock

The use of synchrotron radiation has several advantages. Synchrotron radiation (SR) is extremely intense, highly collimated, highly stable in term of wavelength, polarized and the wavelength can be chosen from a broad energy spectrum according a particular measurement. SR is emitted when charged particles are travelling at high velocity and follow a curved trajectory formed for example by a magnetic field. Modern synchrotron radiation sources are dedicated machines, where electrons or positrons are accelerated to speeds close to that of light and circulate in ultrahigh vacuum tubes. The electron trajectory is guided by magnetic fields. Storage rings are made up of several segments. Straight sections are followed by curved sections, where the electrons are directed via a bending magnet into the next straight section. Synchrotron radiation is emitted in these curved sections. In the straight sections quadrupole and sextupole magnets are used for focusing the particle beam. Moreover, arrays of magnets, so called insertion devices, can be positioned to produce alternating magnetic

fields that cause the path of the electrons to oscillate. Each oscillation leads to the emission of synchrotron radiation and by choosing the number, amplitude, frequency and direction of the oscillations, radiation can be tailored for many different applications [68].

The synchrotron X-ray sources of interest for diffraction are bending magnets and insertion devices known as wigglers and undulators. Usually these have their magnetic field in the vertical direction causing deflection of the electrons in the horizontal plane. The radiation is therefore linearly polarized with the electric component lying in the plane of the synchrotron orbit. For bending magnets, radiation is emitted tangentially throughout the whole curved section, resulting in the emission of a broad tangential fan of X-rays. For wigglers, the oscillations are of relatively large amplitude, and these add together incoherently, increasing the flux proportional to the number of magnetic periods. For undulators, the deflection of the electrons is relatively small and comparable to the natural opening angle of the emitted radiation. Radiation from different oscillations interferes, and the beam becomes collimated. Thus using undulators, the radiation is concentrated into a central on-axis cone surrounded by additional weaker rings. The spectral flux density arriving on a sample is therefore very high.

1.3.1 Kinematical scattering on non-crystalline materials

There are several ways how to characterize materials. Generally, from a structural viewpoint we have crystalline materials and non-crystalline materials. Amorphous materials belong to the group of non-crystalline materials. The amorphous diffraction pattern does not consist of Bragg peaks, but diffuse maxima. The difference between characteristic diffraction patterns is shown schematically in *Figure 6*. The development and application of kinematical diffraction theory can be divided accordingly into two parts: scattering off short-range structural order and long-range order. In the following pages we focus our attention on non-crystalline materials including molecules and glasses.

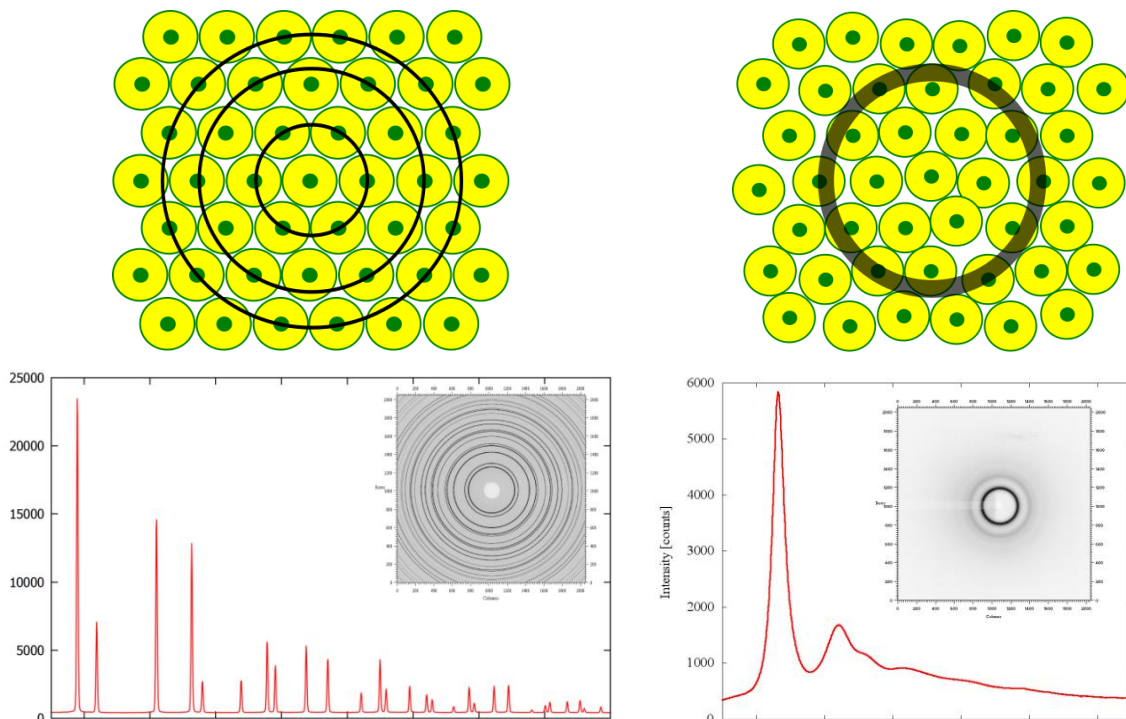


Figure 6: Characteristic diffraction patterns: left- crystalline material (long range order), right- amorphous material (short range order).

The most elementary scattering unit that we shall consider is an electron. Consequently the simplest structure that can be conceived must be comprised of two electrons. The origin is defined to coincide with one electron, and the second is at a position given by the vector \mathbf{r} . Determining the structure of this system therefore means to determine \mathbf{r} . The electrons are

illuminated with a monochromatic X-ray beam, and the elastically scattered radiation is observed along a direction \mathbf{k}' as indicated in *Figure 7*. We will further assume that the source and detector are sufficiently far from the origin that the incident and scattered X-rays may be represented as plane waves. This is the so-called far-field limit, and the resulting diffraction theory is associated with the name of Fraunhofer [69].

The incident wave is specified by its wavevector \mathbf{k} and arrives at the electron at \mathbf{r} after it has scattered from the electron at the origin. The phase lag for the incident wave, ϕ_{in} , is thus 2π times the ratio of z to the wavelength λ , where z is the projection of \mathbf{r} onto the direction of the incident wave. Thus we can write $\phi_{in} = \mathbf{k} \cdot \mathbf{r}$. On the other hand the wave scattered from the electron at \mathbf{r} is *ahead* of the wave scattered from the one at the origin and is given by $\phi_{out} = \mathbf{k}' \cdot \mathbf{r}$. It follows that the resulting phase difference is $\phi = (\mathbf{k} - \mathbf{k}') \cdot \mathbf{r} \equiv \mathbf{Q} \cdot \mathbf{r}$, which defines the wavevector transfer \mathbf{Q} . For elastic scattering $|\mathbf{k}| = |\mathbf{k}'|$. The scattering triangle for inelastic scattering is shown in *Figure 7*. The magnitude of the scattering vector \mathbf{Q} is related to the scattering angle 2θ by [69]:

$$|\mathbf{Q}| = 2k \sin\theta = \left(\frac{4\pi}{\lambda}\right) \sin\theta$$

The scattering amplitude for the two-electron system may be written as:

$$A(\mathbf{Q}) = -r_0(1 + e^{i\mathbf{Q}\cdot\mathbf{r}})$$

where r_0 is the Thomson scattering length (classical electron radius) and it follows that the intensity is:

$$I(\mathbf{Q}) = A(\mathbf{Q})A(\mathbf{Q})^* = r_0^2(1 + e^{i\mathbf{Q}\cdot\mathbf{r}})(1 + e^{-i\mathbf{Q}\cdot\mathbf{r}}) = 2r_0^2(1 + \cos(\mathbf{Q} \cdot \mathbf{r})).$$

Generalizing this simple example, the amplitude scattered from any assembly of electrons may be written as:

$$A(\mathbf{Q}) = -r_0 \sum_j e^{i\mathbf{Q}\cdot\mathbf{r}_j}$$

where \mathbf{r}_j denotes the position of the j^{th} electron. In cases where electrons are described by a continuous distribution the sum is replaced by an integral.

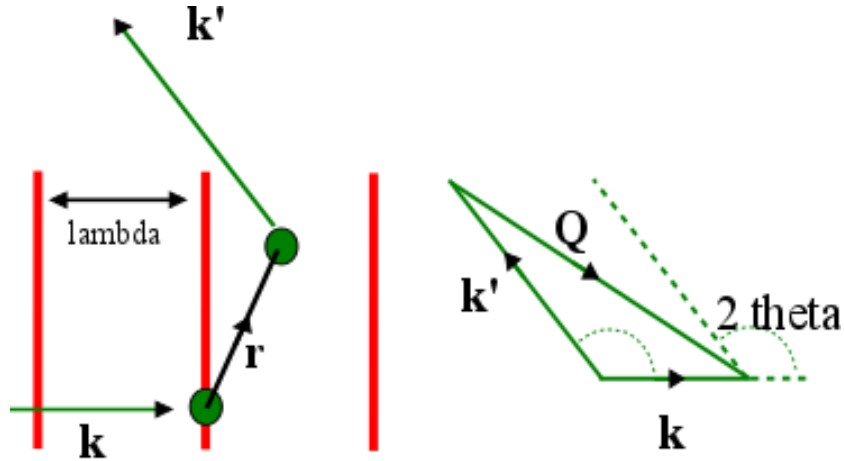


Figure 7: Scattering of a monochromatic X-ray beam by a two-electron system. The incident X-ray is labelled by its wavevector \mathbf{k} , and has wavefronts represented by the vertical lines. Scattered X-rays are observed in the direction \mathbf{k}' . The phase difference between the incident and scattered X-rays is $\phi = (\mathbf{k} - \mathbf{k}') \cdot \mathbf{r} = \mathbf{Q} \cdot \mathbf{r}$, where the wavevector transfer \mathbf{Q} is defined as shown in the scattering triangle to the right [69].

Considering the scattering from an atom, atomic electrons are described as a charge cloud surrounding the nucleus with a number density $\rho(\mathbf{r})$. The charge in a volume element $d\mathbf{r}$, at a position \mathbf{r} is then $-e\rho(\mathbf{r})d\mathbf{r}$, where the integral of $\rho(\mathbf{r})$ is equal to the total number of electrons Z in the atom. To evaluate the scattering amplitude we must weigh the contribution in $d\mathbf{r}$ by the phase factor $e^{i\mathbf{Q}\cdot\mathbf{r}}$, and then integrate over $d\mathbf{r}$, which leads to [69]:

$$f(\mathbf{Q}) = \int \rho(\mathbf{r})e^{i\mathbf{Q}\cdot\mathbf{r}}d\mathbf{r} = \begin{cases} Z & \text{for } \mathbf{Q} \rightarrow 0 \\ 0 & \text{for } \mathbf{Q} \rightarrow \infty \end{cases}$$

where $f(\mathbf{Q})$ is the atomic form factor in units of the Thomson scattering length, $-r_0$. The limiting behavior of $f(\mathbf{Q})$ for $\mathbf{Q} \rightarrow 0$ is obvious, as the phase factor then approaches unity and the total number of electrons is the integral of their number density. In the other limit, when the wavelength of the radiation becomes small compared to the atom there is destructive interference of the waves scattered from the different electrons in the atom.

The next level of complexity we might imagine is to consider scattering from a group of atoms organized into a molecule. Let the atoms be labelled by j (f_j is atomic form factor from

each atom of molecule), so that we can write the scattering amplitude (again in units of $-r_0$) of the molecule as [69]:

$$F^{mol}(\mathbf{Q}) = \sum_j f_j(\mathbf{Q}) e^{i\mathbf{Q}\cdot\mathbf{r}_j}$$

The last step with the describing of the kinematical theory is scattering from glasses. The defining structural characteristic of materials with short-range-order is a degree of randomness in the position of the atoms. The implication of this fact is that any structural order in non-crystalline material, if present at all, can only be described in a statistical sense. Indeed at first glance it might seem surprising to talk about structural order at all in the context of glasses [69]. However, well-defined, short-range structural correlations not only exist in these forms of matter, but as we shall see they can be studied in great detail using X-ray scattering techniques. In the next part we shall see how these structures can be studied.

Part 2

Evaluation Procedures

Evaluation of diffraction patterns not only gives structural properties of a material like grain size, lattice parameter, etc., but by using simple mathematical routines it is possible to extract also mechanical characteristics. Such studies were carried out mostly for crystalline materials. In this chapter the way how to calculate strain and deformation tensor from diffraction patterns is described. Also, a short description of the modelling used is presented.

2.1 Integration procedure

The first evaluation step of the data taken from an isotropic sample in form of 2D frames (2D pictures) is a data reduction process, which converts a two-dimensional frame into a one-dimensional intensity profile; this procedure is called “radial integration”. After radial integration, *Fig. 8*, quantitative and qualitative analysis (such as fitting) can be performed, see *Fig. 9*.

Diffraction images were converted to the radially integrated profiles using the Fit2D [70] program. To perform the radial integration accurately Fit2D requires certain parameters obtained from diffraction of a standard material. The parameters include the coordinates of the centre of the diffraction rings (beam centre), sample to detector distance, angle of the detector to the incident beam (tilt), wavelength of the X-rays, maximum 2θ angle or Q of the scan and number of bins in the output data set.

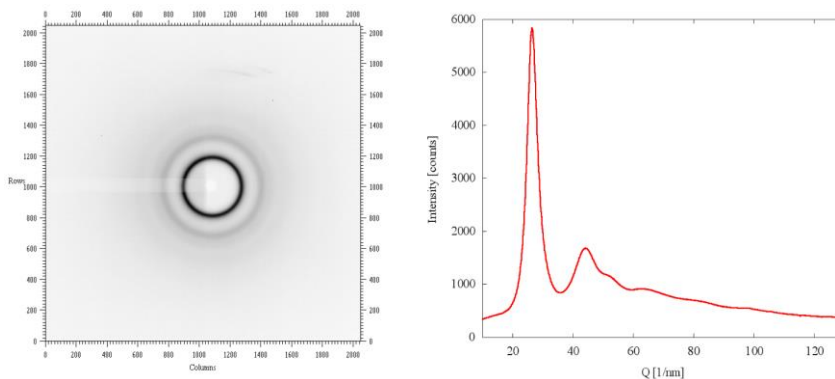


Figure 8:
Process of data evaluation:
left-2D diffraction pattern,
right diffraction pattern after
radial integration.

The sample to detector distance is calibrated using standard materials. X-ray standards/calibrants in powder diffraction are for example LaB_6 and CeO_2 . For the experiments with nano- and micro- X-ray beams it is preferable to use CeO_2 because its grain size is about $4.5 \mu\text{m}$ while the grain size of LaB_6 is about $15 \mu\text{m}$.

The detector is usually adjusted manually orthogonal to the X-ray beam. However, it may not always be possible to align the detector with sufficient accuracy. It is then necessary to calibrate the tilt from the powder rings of the standard sample. Incorrect determination of the sample to detector distance and wavelength causes a shift of peaks in the resulting one-dimensional intensity profile. Neglecting the detector tilt and wrong determination of beam centre causes deformation of the peak-shapes.

2.2 Fitting procedure

The peak shape of amorphous material is usually fit by a non-linear least-squares fit of the pseudo-Voigt function which contains a Gauss function and a Lorentz function:

$$pV(Q) = A[\eta G(Q) + (1 - \eta)L(Q)]$$
$$G(Q) = \exp\left[-\frac{(\ln 2)(Q-Q_0)^2}{w_g^2}\right] \text{ and } L(Q) = \left[1 + \frac{(Q-Q_0)^2}{w_l^2}\right]^{-1}$$

where A is the amplitude of the intensity of a maximum, η is the mixing parameter of the contributions of $G(Q)$ and $L(Q)$ that are Gaussian and Lorentz functions, respectively, $2w_g$ is the full width at half maximum for the Gauss and $2w_l$ is the full width at half maximum for the Lorentz part. Q_0 is the position of the peak maximum.

The radially integrated diffraction images are generally analyzed for peak center, intensity, peak's width mixing parameter and background, see *Figure 9*.

From the fitted variables, we are able to estimate following structure characteristics:

- from the shift in the peak position Q_0 we can calculate the elastic deformation in a material
- from the intensity of the peak we can calculate the behavior of crystal grains and their orientation
- from the full width at half maximum w we can calculate the size of crystal grains and the internal strains, matrix defects, microstrains and size of correlated regions

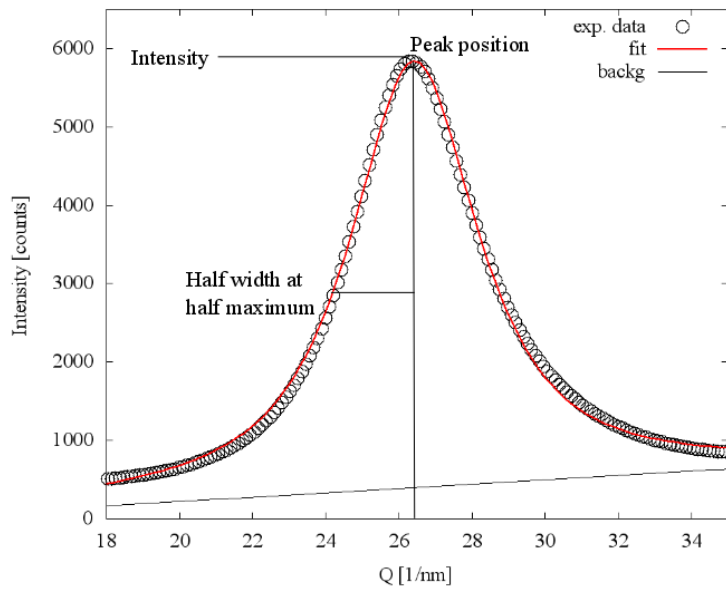


Figure 9:
Integrated diffraction pattern with
fitting curve; experimental points –
black circles, fit - red curve.

2.3 The influence of deformation on the diffraction pattern of an amorphous sample

Poulsen et al. [71] demonstrated that it is possible to obtain information about the internal distribution of strain also for disordered systems if an appropriate analysis of high quality diffraction data is carried out. They used the same simplification as Yavari et al [72] assuming that small changes of interatomic distances in the amorphous material are directly connected with the change of the position of the diffuse maximum.

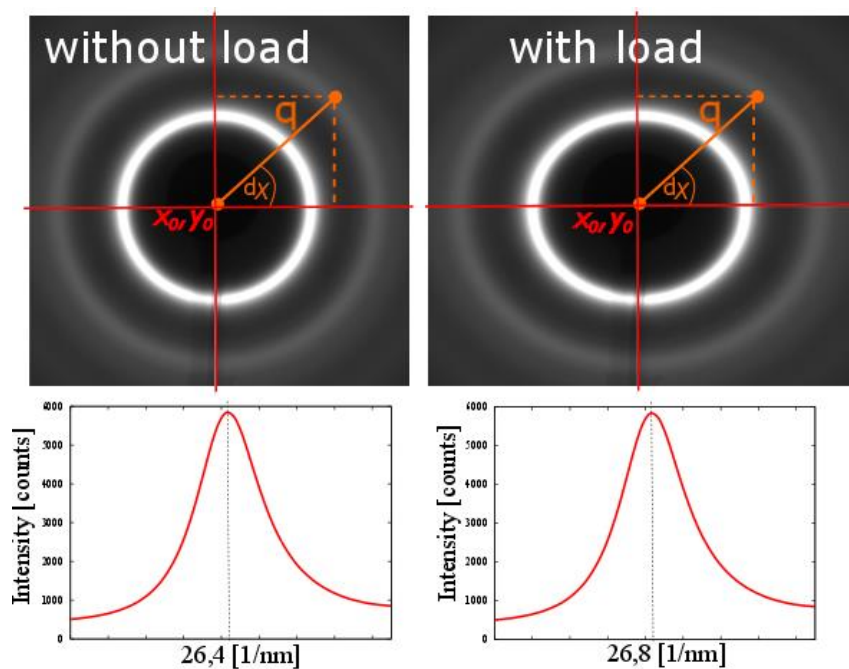


Figure 10: Left column represents 2D and integrated diffraction pattern taken from amorphous material without applied load. On right side with applied load. One can see the influence of load on the position of the diffuse maximum.

The diffraction pattern without applying load is characterized by perfectly symmetric circular rings. During the application of load on the sample, its diffraction pattern changes, symmetric circular rings take an elliptic shape, *Figure 10*. The ellipticity of diffraction rings is connected with the mechanical properties of the investigated material.

2.4 Calculation of Deformation Tensor from the diffraction pattern of an amorphous sample

One of the standard integration procedures which allows defining a certain area of interest within the scattering pattern is the so-called caking procedure, see *Figure 11*. Upon applying load the distance between the centre of a diffraction pattern and a certain position on the ring is different at different azimuthal angles χ .

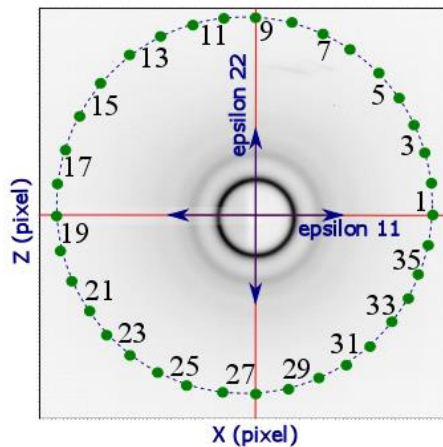


Figure 11: 2D diffraction pattern with sketch of strains direction. Green points define the position of the cakes for integration.

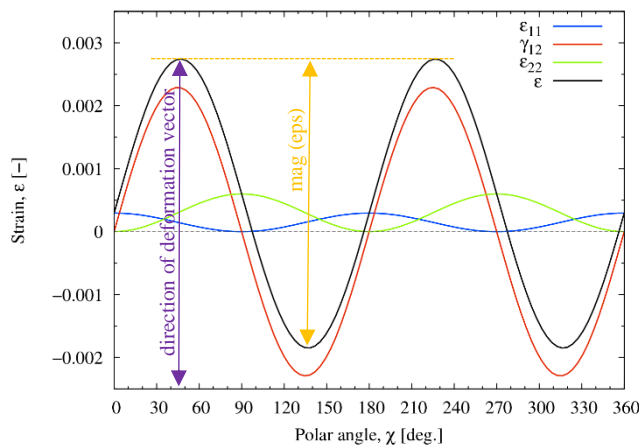


Figure 12: Azimuthal angle dependence of strain (deformation tensor) – black line and its decomposition into three components - ϵ_{11} axial, γ_{12} shear and ϵ_{22} tangential. Mag (eps) is the magnitude (peak – to – valley) and the direction of the deformation vector is given by the maximum value

The diffraction pattern is characterized by polar coordinates (Q , χ). By dividing the χ -range from 0 to 2π into 36 segments one obtains intensity distributions:

$$I_i(Q, \chi_i) = \int_{\chi_i - \pi/36}^{\chi_i + \pi/36} I(Q, \varphi) d\chi$$

with $i = 1 \dots 36$, where $Q = Q(s)$ is defined by: $Q = \frac{4\pi}{\lambda} \sin\left(\frac{1}{2} \arctg \frac{s}{D}\right)$, in which λ denotes the wavelength, D refers to the sample-to-detector distance and s represents the distance from the origin of the polar coordinate system. The relative change of the position of the first peak upon applying an external stress defines the strain [71]:

$$\varepsilon_i(\chi_i, \sigma) = \frac{Q_0(\chi_i, 0) - Q_\sigma(\chi_i, \sigma)}{Q_\sigma(\chi_i, \sigma)}$$

which is angular dependent. The angular variation of the strain can be fitted by the following expression:

$$\varepsilon(\chi_i, \sigma) = \varepsilon_{11} \cos^2 \chi - \gamma_{12} \sin \chi \cos \chi + \varepsilon_{22} \sin^2 \chi$$

where ε_{11} is the axial component, γ_{12} is the in-plane shear component and ε_{22} the tangential component of the tensor of deformation.

2.5 X-ray diffraction experiments

X-ray diffraction (XRD) is universal and non-destructive technique that yields detailed information on the chemical composition, physical properties and atomic structure of matter. XRD is based on observing the scattered intensity of X-ray radiation as a function of scattering angle, polarization and wavelength or energy. In this work the XRD patterns of the samples were recorded in order to determine and visualize strain-fields induced in the material by stress during indentation. Two scattering geometries were used: Bragg-Brentano geometry (reflection mode) and Debye-Scherrer geometry (transmission configuration).

In transmission geometry, the X-ray beam passes through the sample and interacts with the volume in bulk material, see *Figure 13 - left*. X-ray diffraction in transmission geometry is a powerful tool for examining the strain state of the sample averaged over the sample thickness. In reflection geometry, the X-ray beam penetrates the surface of the sample and provides information just from a certain (penetrated) volume of material, see *Figure 13 - right*. X-ray diffraction in reflection geometry is revealing changes in the structure of sample close to the surface.

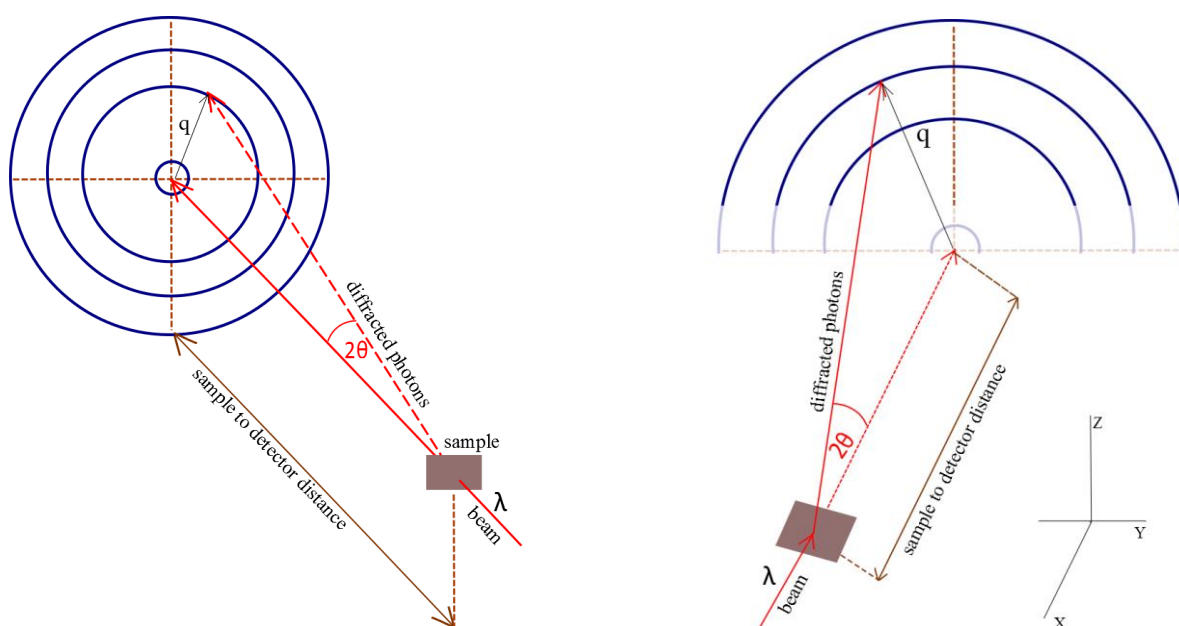


Figure 13: left - transmission mode (Debye-Scherrer geometry); right - reflection mode of XRD measurement

Different experiments and experimental techniques require different types of detectors. For the purposes of our experiments we used two dimensional detectors which are in more detail described in the experimental part of this work. In general we used detectors which combine fast data acquisition speed and accurate diffuse maximum identification capabilities allowing for example the study of the evolution of a diffuse maximum shift.

Part 3

Experiments

The following section is devoted to the characterization of the experimental stations used for the X-ray measurements described in this thesis and the description of the nanoindenter which was used for the in-situ experiments. Due to the fact that we are going to describe four different experiments (realized at different experimental stations, at different geometry and with different aims), we decided to describe each experiment and its realization independently.

3.1 Samples

In our experiments different Zr-based metallic glasses were investigated. The measured samples were prepared at the IFW Dresden (Dresden, Germany) using conventional copper mold injection casting. A summary of the measured samples and the experimental conditions is given in the *Table 2*.

Vitreloy 105 (Vit105) with nominal composition of $Zr_{52.5}Ti_5Cu_{17.9}Ni_{14.6}Al_{10}$ was prepared in the shape of a 50 mm tall rod with a diameter of 3 mm. A sample with a height of 7 mm was cut using a diamond wire. Also, a sample in the shape of a plate 15 mm tall and 10 mm wide with a thickness of 1 mm was prepared. In addition, using high purity raw materials, $Zr_{53}Cu_{18.7}Ni_{12}Al_{16.3}$, $Zr_{51.9}Cu_{23.3}Ni_{10.5}Al_{14.3}$ and $Zr_{50.7}Cu_{28}Ni_9Al_{12.3}$ were prepared and again using a diamond cutter 40 μ m thick, 5 mm wide and 5 mm long slices were cut out.

Table 2

Summary of measured samples and experimental condition

composition	experiment geometry	type of indentation	type of experiment	beamline
$Zr_{52.5}Ti_5Cu_{17.9}Ni_{14.6}Al_{10}$	reflection	Berkovich	ex-situ	P06 - DESY
$Zr_{52.5}Ti_5Cu_{17.9}Ni_{14.6}Al_{10}$	transmission	Vickers	ex-situ	P02.2 - DESY
$Zr_{53}Cu_{18.7}Ni_{12}Al_{16.3}$	transmission	Berkovich	in-situ	P03 – DESY
$Zr_{51.9}Cu_{23.3}Ni_{10.5}Al_{14.3}$	transmission	Berkovich	in-situ	P03 – DESY
$Zr_{50.7}Cu_{28}Ni_9Al_{12.3}$	transmission	Berkovich	in-situ	P03 – DESY
$Zr_{53}Cu_{18.7}Ni_{12}Al_{16.3}$	transmission	wedge	in-situ	ID11 - ESRF

3.2 Experimental stations

Experimental measurements using X-ray diffraction were carried out at the synchrotron radiation sources PETRA III in Deutsches Elektronen Synchrotron - DESY (Germany, Hamburg) and in European Synchrotron Radiation Facility – ESRF (France, Grenoble).



Figure 14: PETRA III, DESY, Hamburg, Germany.



Figure 15: ESRF, Grenoble, France.

The PETRA III storage ring at DESY, *Figure 14*, with a length of 2304 meters, took up operation in 2009. It is the most brilliant and powerful synchrotron radiation light source in the world and offers scientists outstanding experimental opportunities. On one eighth of the ring an experimental hall named after Max von Laue was built that accommodates nine straight sections with a total of 14 undulator experimental stations (year 2014) with 30 instruments [68].

The ESRF storage ring, *Figure 15*, has a circumference of 844.4 meters and offers 46 beamlines (in year 2015). This facility is open to users since the year 1994 [74].

3.3 Ex-situ experiment at end-station P06

A first experiment of pre-indented samples was performed at the P06 (Hard X-ray Micro/Nano-Probe) beamline of PETRA III. The beamline houses two different experimental stations: Nanoprobe and Microprobe. Experiments were carried out using the Nanoprobe end-station. The hard X-ray nanoprobe is based on nano-focusing refractive X-ray lenses. The instrument (sample position) is located 98.2 meters from the undulator source. It is designed to generate a nano-beam with a lateral size of 50 nm and below and supports experiments using transmission, fluorescence, and diffraction contrast [75].

At the P06 beamline Vitreloy 105 (Vit105) with nominal composition $Zr_{52.5}Ti_5Cu_{17.9}Ni_{14.6}Al_{10}$ in the shape of a 7 mm tall rod with a diameter of 3 mm was investigated. The indentation tests were done at the Slovak Academy of Science (Kosice, Slovakia) employing a nanoindenter Agilent G200, see *Figure 16*.

Table 3

Selected properties of $Zr_{52.5}Ti_5Cu_{17.9}Ni_{14.6}Al_{10}$ from literature [79, 80, 81].

experiment geometry	Reflection
type of indenter	Berkovich
hardness	5.95 ∓ 0.621 GPa
elastic modulus	95.9 ± 10 GPa
depth of indent	2,8 μ m

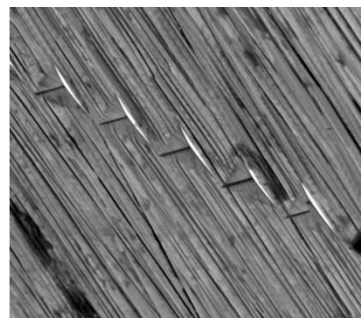




Figure 16: Agilent G200 nanoindenter, with zoom on its sample stage

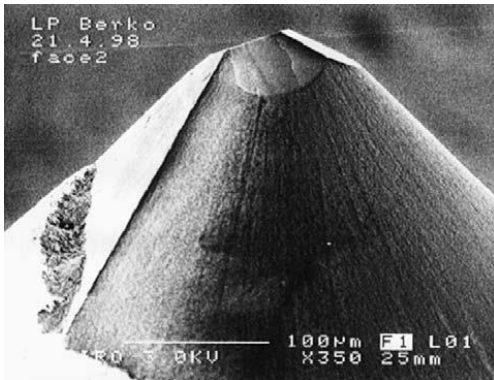


Figure 17: High-magnification SEM scan of the tip of a Berkovich diamond indenter.

Using a Berkovich (three - sided sharp type) indenter (*Figure 17*) a line of indents with a diagonal of $30\ \mu\text{m}$ was created, see *Figure 18*. During the indentation a maximum load of $5\ \text{N}$ was applied. A schematic drawing of the sample surface with the line of indents and the sample shape are depicted in *Figure 19-a*. The scheme of the experiment is schematically shown in *Figure 19-b*. Spatially resolved X-ray diffraction scans (two-dimensional matrix scans) were performed using a nanometer sized monochromatic photon beam with an energy of $15.25\ \text{keV}$ (corresponding to a wavelength of $0.8130\ \text{\AA}$). XRD experiments were done in reflection mode. The size of the beam was $600 \times 600\ \text{nm}^2$ (width \times height). Since the surface of the sample was inclined to the direct beam at 25 degrees, the effective beam footprint on the sample was $600 \times 1400\ \text{nm}^2$. The size of the scanned sample area was $50 \times 50\ \mu\text{m}^2$.

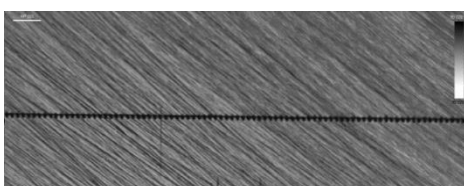


Figure 18: Top surface of the sample with a line of indents produced by a Berkovich indenter.

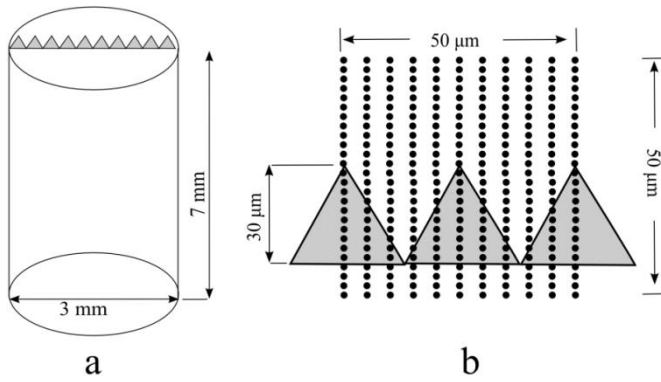


Figure 19:

- a) Sketch of the sample, the line of indents is on the top.
- b) Detailed view of the matrix scan for XRD measurements of the sample surface.

X-ray scanning was realized by translating the sample in X and Y directions with well-defined steps using a HEXAPOD with a resolution of 1 μm . XRD patterns were collected in reflection mode by a CCD camera (MAR 165 pixel size 80 x 80 μm^2). One diffraction pattern was collected for 300 seconds. The sample-to-detector distance was 95 mm. One example of a diffraction pattern obtained during the measurement after its radial integration is shown in Figure 20.

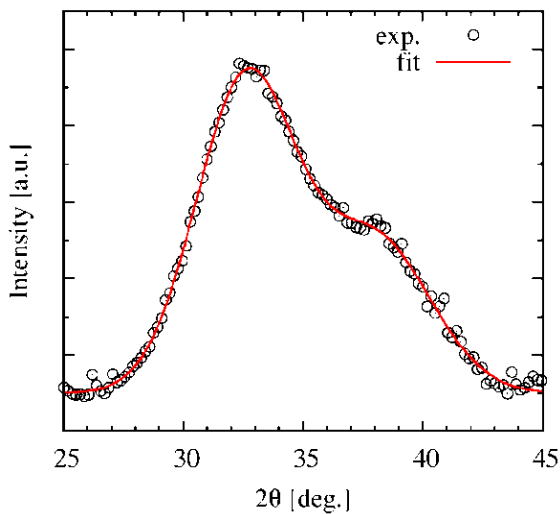


Fig. 20 Integrated 2D diffraction pattern (randomly chosen from diffraction map). Circles are experimental data and the red curve is a fit using two pseudo-Voigt functions.

XRD confirmed that the $\text{Zr}_{52.5}\text{Ti}_5\text{Cu}_{17.9}\text{Ni}_{14.6}\text{Al}_{10}$ sample was in the fully amorphous state. The first and the strongest diffuse peak expected at $2\theta = 19.4^\circ$ could not be detected due to the large absorption of the sample (absorption length is 37 μm at 15.25 keV) and its orientation with respect to the direct beam (the angle between the sample surface and the direct beam was 25 degrees). Therefore we could acquire XRD data only above $2\theta = 25^\circ$. As can be seen in Figure 20, we detected only a small part of the 2θ range which moreover shows a relatively

low intensity compared to the background due to the response of the MAR 165 CCD camera. Therefore it has been decided to calculate the residual strains induced by the nano-indentation from the second diffuse maximum located at $2\theta_0 = 32.6^\circ$. The exact position of the second diffuse maximum was obtained by fitting of the experimental data by a profile function consisting of a linear background and two pseudo-Voight functions. The second function was used to account for the right shoulder at $2\theta = 38^\circ$. As can be seen from the data presented in *Figure 21*, the proposed profile function perfectly matches the experimental XRD pattern.

In the work of Hufnagel et al. [76] the strain ε was calculated from the relative change of the peak position of the first diffuse maximum. As mentioned above, we calculated strains from the change of the peak position of the second diffuse maximum. Diffraction patterns measured on a position far away from indents were used to estimate the position of the maximum without stress θ_0 .

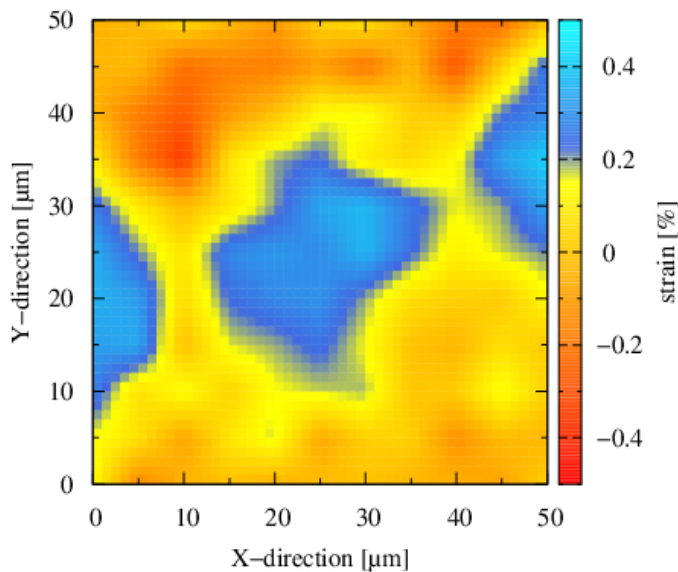


Figure 21:
Map of the residual strain field induced in the indented sample calculated from the peak shifts of the second diffuse maxima.

Figure 21 shows a two-dimensional map of the residual strain field induced in the sample by indentation and determined from 275 XRD patterns (11 columns and 25 rows). The values of strains in *Figure 21* are represented by color. The blue parts of the picture refer to positive strain which is attributed to the positions of the indents. Their shape is distorted due to measuring in reflection geometry and the limited density of measuring points within the matrix scan. Despite of that one can clearly identify the positions and the shape of the indents and quantitatively describe the strain state after indentation. An interesting result of ex-situ mapping of indentations is that we can determine the field of residual strain in BMG material.

3.3 Ex-situ experiment at end-station P02

While the experiment described in the previous chapter was performed in a reflective mode and photons with low energy, the ex-situ experiment described in this chapter was carried out in the transmission mode with energy of photons sufficient to determine such 2D diffraction patterns which allowed us to determine some components of the deformation tensor.

The experiments on pre-indented samples were performed at the P02 beamline of PETRA III. The P02 beamline station covers two different experimental stations in separate hutches; the Extreme Condition Beamline (ECB) P02.2 and the High Resolution Powder Diffraction Beamline - P02.1. The described X-ray experiment was done at ECB [77] and then repeated at High Resolution Powder Diffraction Beamline P02.1 [78].

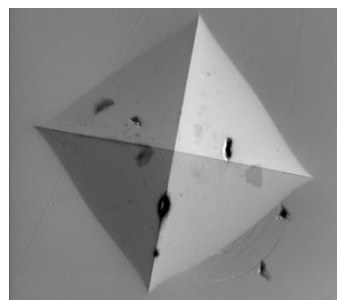
The ECB offers fixed energies at 25.7, 42.9 and 60 keV and focusing in the range of micrometres using KB mirrors or a compound refractive lens system. The High Resolution Powder Diffraction Station Beamline - P02.1 offers a fixed X-ray energy of 60keV and focussing by lenses

The experiment was done using both experimental stations. Because of the same sample and the same indent was investigated, results are described together in one chapter.

Table 4

Selected properties of $Zr_{52.5}Ti_5Cu_{17.9}Ni_{14.6}Al_{10}$ from literature [79, 80, 81]

experiment geometry	transmission
type of indenter	Vickers
hardness	579 Hv
elastic modulus	88,6 GPa
depth of indent (at load 500 N)	50 μ m



In the experiment a sample of the metallic glass Vit105 in the shape of a plate 15 mm tall, 10 mm wide and 1 mm thick, with nominal composition of $Zr_{52.5}Ti_5Cu_{17.9}Ni_{14.6}Al_{10}$ was investigated. The indentation of the sample was done in DESY (Hamburg, Germany) via a micro-indenter Mitsutoyo HV-114, *Figure 22*, using a Vickers, four - side sharp type indenter, *Figure 23*. Four indents with different loads were created, 100, 200, 300 N and the maximum load of 500 N were applied. A schematic drawing of the sample surface with indents and the sample shape are depicted in *Figure 24*.

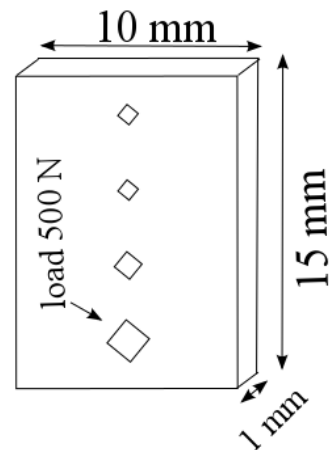
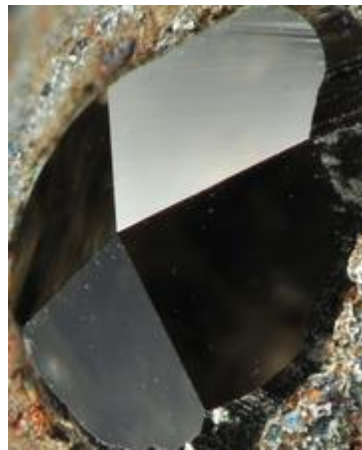


Figure 22: Micro-indenter Mitsutoyo HV-114.

Figure 23: Vickers (four-sides) indenter.

Figure 24: Sketch of sample with indents created by Vicker indenter at loads 100, 200 300 and measured indent at 500 N.

We did the XRD measurement at beamline P02.2 on the indent created by indentation with 500 N load. Moreover, only part of the indent and its vicinity was mapped due to the long integration time required for this experiment. Spatially resolved X-ray diffraction scans (two-dimensional matrix scans) were performed using a micro-meter sized monochromatic photon beam with an energy of 43 keV. XRD experiments were done in transmission mode, the beam size was $1.8 \times 1.9 \mu\text{m}^2$ (width \times height). The size of scanned sample area was $350 \times 600 \mu\text{m}^2$, see *Figure 25*.

The scanning was realized by translating the sample in Y and Z directions with well-defined steps with a resolution of $1 \mu\text{m}$. XRD patterns were collected by a Perkin Elmer 1621 detector (pixel size $200 \times 200 \mu\text{m}^2$). One diffraction pattern was collected for 60 seconds. The sample-to-detector distance was 309.7 mm.

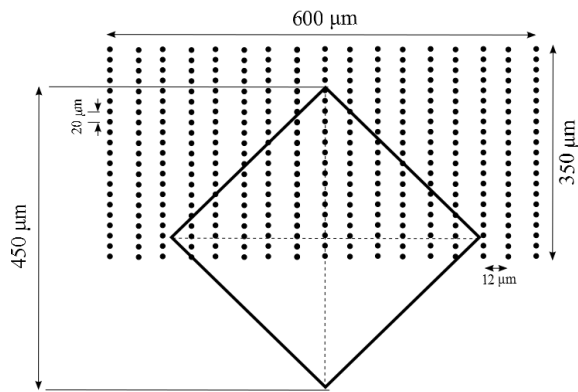


Figure 25:

Sketch of the indented sample with detailed view of the matrix scan for XRD measurements.

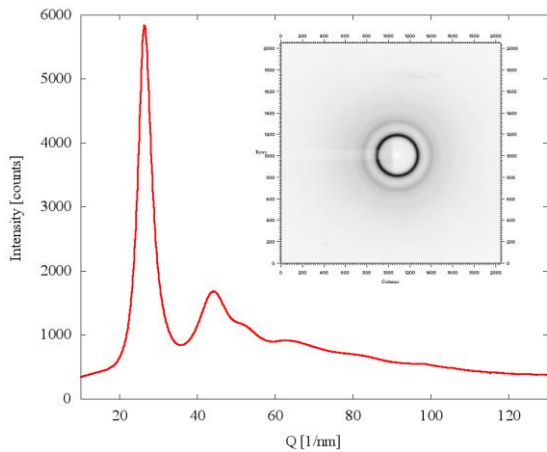


Figure 26:

Integrated 2D diffraction pattern (third column, fourth row). Insert: Diffraction pattern obtained from the 2D-detektor (Perkin Elmer 1621).

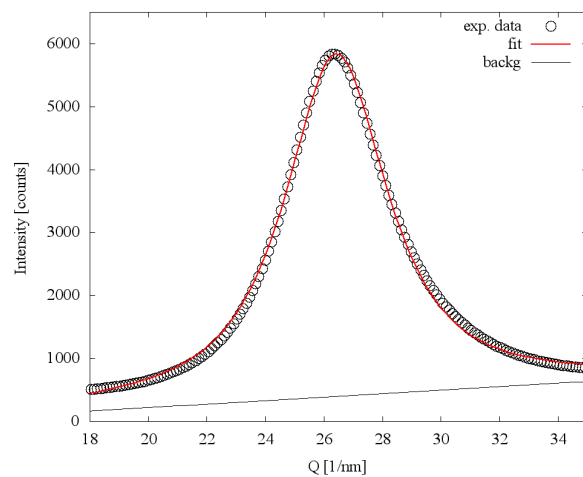


Figure 27:

Integrated 2D diffraction pattern (zoom on first diffuse maximum); experimental points – black circles, fit - red curve.

One should keep in mind that indenting the sample perpendicular to its surface does not only induce strains along normal direction (in which we send X-rays) but due to the indent shape also to other directions. When doing XRD experiments in transmission geometry with X-rays parallel to the normal of the sample surface (X axis) we are preferentially sensitive to the in plane (namely Y-Z plane) correlations. As one can see from the *Figure 12* (it is showing strain variation with azimuth angle χ from one point in the matrix scan of indented sample) the extent of strain anisotropy is relatively large. So assumption that measuring XRD along X-axis would reveal only spherical patterns without any strain is not confirmed.

Figure 28 shows the magnitude (peak-to-valley) of the strain curve $\varepsilon = \varepsilon(\chi)$ determined at every position of the matrix scan within the X-Z plane. This is the three-dimensional map of the residual strain field induced in the sample during the indentation at 500 N. In other words from every position within the Y-Z plane we get a curve similar to the one shown in *Figure*

12. Then we determine the magnitude (the peak-to-valley value) of the strain curve and construct a plot as shown in *Figure 28*. It is interesting to note that plotting the magnitude of the strain curve resembles the morphology of the sample after indentation. Of course, because diffraction peak position is corresponding only to the elastic part of the deformation, the shape of the indent is not a copy of the real imprint to the sample. The maximal obtained strain is 0,0047 observed on the top of indent, where the elastic deformation is maximal. The maximal plastic deformation is of course in the bottom of indent, therefore the values of elastic strains are there minimal – almost zero.

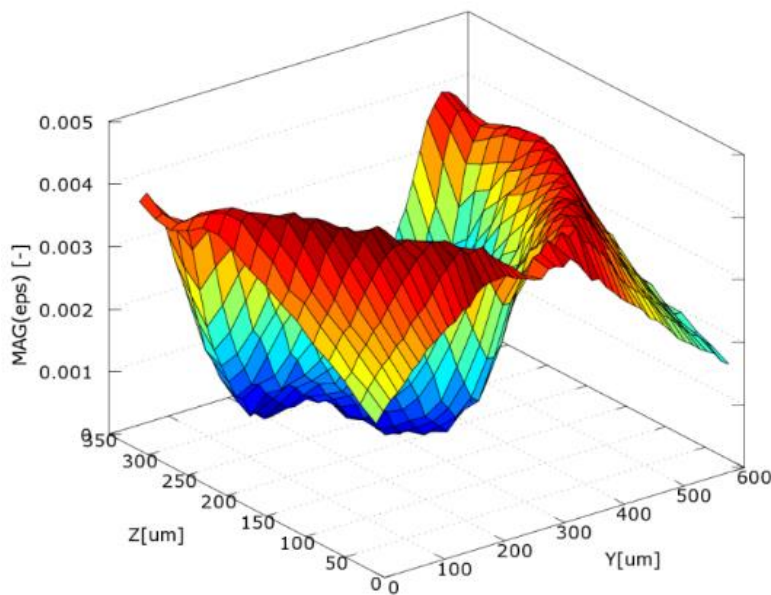


Figure 28:
3D map of peak-to-valley amplitude of strains of $Zr_{52.5}Ti_5Cu_{17.9}Ni_{14.6}Al_{10}$ indented by Vickers indenter at load 500 N.

The experiment was repeated at beamline P02. Spatially resolved X-ray diffraction scans were performed using a micro-meter sized monochromatic photon beam with an energy of 60 keV, in transmission mode, the beam size was $25 \times 25 \mu\text{m}^2$ (width \times height). The size of the scanning sample area was $800 \times 1000 \mu\text{m}^2$, see *Figure 29*. The scanning was realized by translating the sample in Y and Z directions with step size of $\Delta y = 25 \mu\text{m}$ and $\Delta z = 25 \mu\text{m}$. XRD patterns were collected by a Perkin Elmer 1621 detector (pixel size $200 \times 200 \mu\text{m}^2$). One diffraction pattern was collected 10 seconds. The sample-to-detector distance was 326 mm.

XRD confirmed that the $Zr_{52.5}Ti_5Cu_{17.9}Ni_{14.6}Al_{10}$ sample is in the fully amorphous state, see *Figure 26* and *27*. The first and the strongest diffuse peak was detected at $Q = 26.37 \text{ nm}^{-1}$, *Figure 27*. As can be seen, the signal detected from the sample is far more intense than the background (air scattering). Each diffraction pattern was subjected to the caking procedure

and radial integration. The exact position of the first diffuse maximum was obtained by fitting the experimental data using a profile function which consists of a linear background and a pseudo-Voigt function. The amorphous halo has a circular shape for diffraction patterns taken from a non-deformed part of the sample, in contrast to the deformed part, where the amorphous halo has an elliptical character.

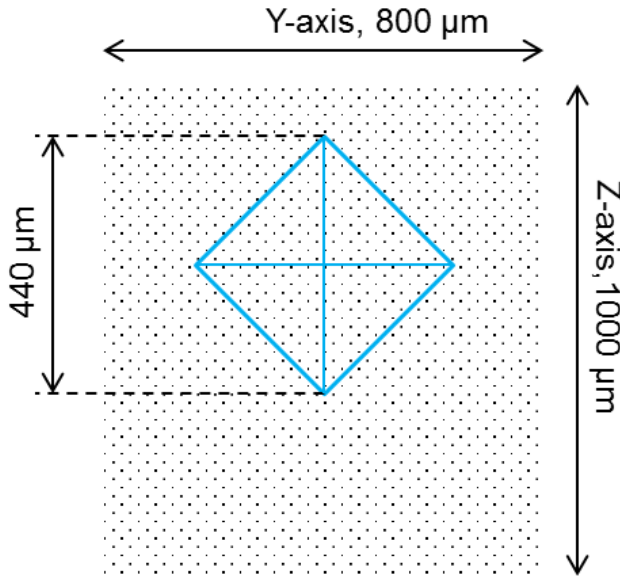


Figure 29:
Sketch of the indented sample with detailed view of the matrix scan for XRD measurements.

From the data obtained it was possible to calculate the axial (ε_{11}), planar (γ_{12}) and tangential (ε_{22}) component of the deformation tensor (see *Chapter 2.4*):

$$\varepsilon(\chi) = \varepsilon_{11} \cos^2 \chi - \gamma_{12} \sin \chi \cos \chi + \varepsilon_{22} \sin^2 \chi$$

From the analysis of the 2D maps, which display deformation tensors calculated from each diffraction pattern, different information like the size of the elastic strain and its direction can be obtained, *Figure 30 a-d*.

From $|\varepsilon|$ one can clearly identify the shape of created strain field. Analysis has to take into account that X-ray is sensitive only on the elastic part of the deformation. As soon as the limits of Hooke's law are exceeded, the real shape of the strain field consists of elastic and plastic deformation, but we visualize just the elastic part. This effect is mostly observable at the location of the centre of the indent (the 0, 0 position in the *Figure 30 a-d*). At this place

total strains are maximal (maximal plastic deformation and minimal elastic deformation), but according to the measured map total strains are minimal.

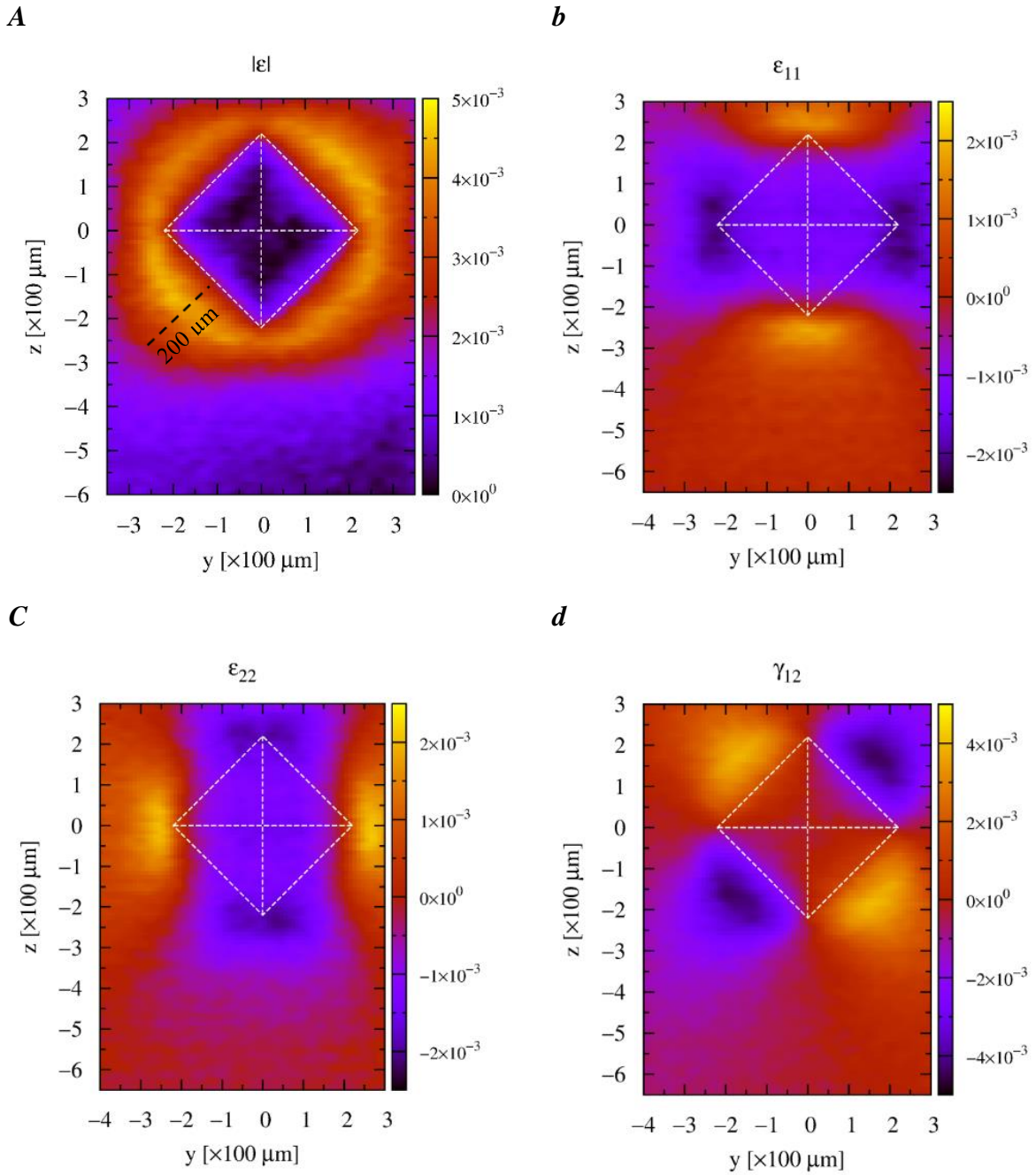


Figure 30 a-d: 2D map of total strain values $|\epsilon|$ and axial (ϵ_{11}), planar (ϵ_{22}) and tangential (γ_{12}) components of deformation tensor, obtained from diffraction data in the indented $Zr_{52.5}Ti_5Cu_{17.9}Ni_{14.6}Al_{10}$ BMGs.

From the ex-situ experiments we derive the deformation tensor components, which is not possible to obtain from other standard techniques dealing with mechanical properties of

materials, expect of theoretically calculated models which are discussed in the chapter *Discussion*.

On the 2D map of total strain values $|\epsilon|$ of $Zr_{52.5}Ti_5Cu_{17.9}Ni_{14.6}Al_{10}$ BMGs, *Figure 30 a*, is nicely seen the shape of the indent. The highest values are around the indent, there is maximal elastic deformation. From this 2D map we can see the impact of indentation on the material. According to literature, the elastic deformation has maximal impact 4 times the depth of the indent. In our case the depth of the indent is $50\ \mu\text{m}$ so the maximal impact of elastic deformation should be $200\ \mu\text{m}$. This distance is depicted by black dashes line in *Figure 30 a*. Axial (ϵ_{11}), planar (γ_{12}) and tangential (ϵ_{22}) components of the deformation tensor, obtained from diffraction data are shown in *Figure 30 b, c, d*. From this experiment we can see that the elastic strain tensor of residual strain is possible to calculate from the diffraction peak position also in amorphous material after nanoindentation. Experiment also demonstrate very high sensitivity of measurement of residual strains by 2D X-ray diffraction with high resolution of sample mapping.

3.4 ALEMNIS SEM nanoindenter

In-situ experiment in this work means that we studied the structural changes of a material during indentation. The aim of these experiments was to study the elastic part of the deformation, the strain-fields occurring in the sample during loading and to obtain new information about the elastic behaviour of a BMG before the collapse.

For indentation of specimens during the experiments we used an ALEMNIS SEM Indenter. The indenter and its functionality, and experiments are described in following section.

The SEM Indenter is a compact test platform for in-situ material characterization. The SEM Indenter has been developed to work inside scanning electron microscopes as well as light microscopes or synchrotron radiation sources. The SEM Indenter includes three long-range stick-slip piezoelectric actuators to position the samples with nano-meter resolution, see *Figure 31*. Indentation can be realized with force or displacement control or combination of both. An ALEMNIS SEM Indenter was used at the PETRA III facility for the first time for purposes of this thesis.

One of the aims of this dissertation thesis was to find an indenter satisfying and respecting beamlines requirements. The highest priority in the selection procedure was given to temporal stability, geometry, dimensions and weight. The stability in time is very important during in-situ experiments because such experiments take time in the order of hours, not minutes, like in case of SEM indentation experiments. The stability of the selected ALEMNIS SEM Nanoindenter was very good, during almost 9 hours the indenter does not fluctuate in load (± 0.06 mN) and the total drift was very low (0.15% from total indentation depth). The geometry of the indenter was very important because the indenter should be used at different beamlines in reflection and transmission mode. This means that we need to have enough space for the incoming and the scattered (outgoing) X-ray beam. Thus the construction of the indenter should be as lean as possible but also stable and strong. The indenter shouldn't have a problem to provide indentation at any position and orientation in space. Its weight is very

important, because for the alignment of a sample (which is in the indenter) to the nano-beam we need to perform movements of the order of micro- or even nano-meters. Stages which are able to perform movements of that precision can carry only limited weight. Regarding specifications it was important to keep high flexibility for various types of measurements.

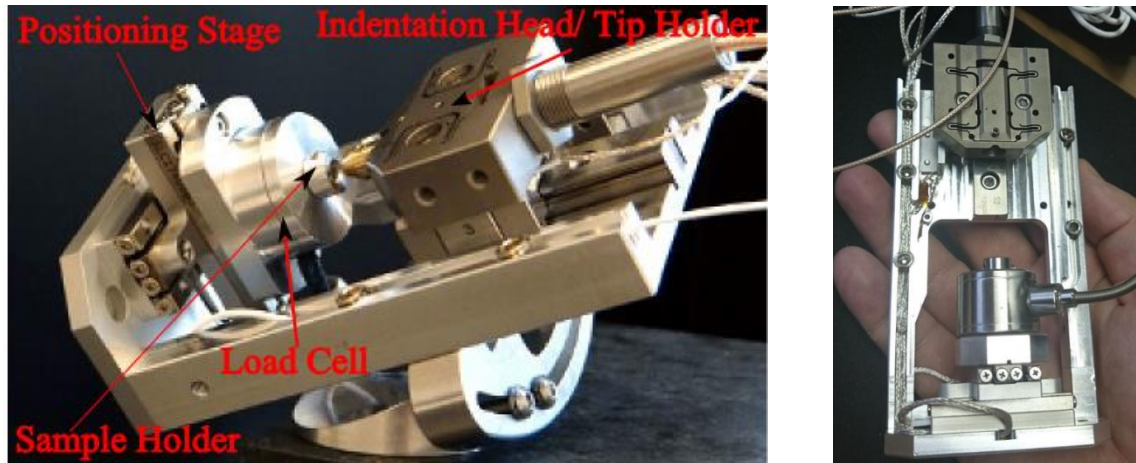


Figure 31 - left: Alemnis SEM indenter with the description of its main components.

Figure 31 - right: Alemnis SEM indenter adjusted for the purposes of PETRA III synchrotron beamlines.

The indenter dimensions are: length 140 mm, width 65 mm and height 60 mm. The weight is 750 g. The geometry of the frame was adjusted for needs of synchrotron radiation beamlines. The maximum indentation load is 5 N (with noise from 4 μ N to 60 μ N). In depth control mode the maximal indentation depth is 35 μ m (with a resolution of 1.8 nm). The micro-positioning-stage system, see *Figure 31*, covers 22 mm in the direction between sample-holder and indenter-tip and in the plane of the sample-holder covers 20 mm. The weight of the sample can be up to 15 g. Attached to the indenter there is an optical camera. The camera is removable (for purposes of using the indenter in a SEM). Using the camera we can more easily find an appropriate place for indentation and subsequently using the included software provides a preliminary characterization of the indentation experiment.

The indenter is very easy to use. The included software was optimized to be intuitive and user friendly. An important fact as this set-up will be used by different users with different requirements for the experiment and different scientific background. The indenter was (for purposes of this thesis) successfully used at beamlines P03 and P02.1 at PETRA III synchrotron in DESY, Hamburg and also at the ID11 beamline in ESRF, Grenoble. The description of experiments and results are content of the following chapters.

3.6 In-situ experiment at end-station P03

P03 is the micro-focus small- and wide-angle X-ray scattering beamline μ SAXS/WAXS at PETRA III. This beamline offers the possibility of a nano-beam, the minimum beam size being 250 nm by 350 nm and the long focal distance optics (up to 15 cm) offers enough clear working distance for installing the ALEMNIS SEM Nanoindenter for purposes of in-situ measurements.

Table 5

Selected properties of $Zr_{53}Cu_{18.7}Ni_{12}Al_{16.3}$, $Zr_{51.9}Cu_{23.3}Ni_{10.5}Al_{14.3}$, $Zr_{50.7}Cu_{28}Ni_9Al_{12.3}$ from literature [79, 80, 81, 82].

experiment geometry	transmission
type of indenter	Berkovich
hardness	550 Hv
elastic modulus	102 GPa
depth of indent	4 μ m

The main objective of this part of the work is to report about the unique combination of nanoprobe tools (nanoindentation and X-ray nanodiffraction) used to obtain a full picture of the elastic strain distribution appearing around an indent during the loading of an amorphous alloy. The strain field occurring beneath the indenter-diamond-tip during the indentation is mapped on the base of the analysis of diffraction patterns produced by a nanoprobe beam.

Three slices of Zr-based amorphous plate samples were investigated. The samples have the composition $Zr_{53}Cu_{18.7}Ni_{12}Al_{16.3}$, $Zr_{50.7}Cu_{28}Ni_9Al_{12.3}$ and $Zr_{51.9}Cu_{23.3}Ni_{10.5}Al_{14.3}$. Samples were carefully placed at once into the sample holder of the nanoindenter and aligned to be perpendicular to the incoming X-ray beam, see *Figure 32, 33 and 34*. The indenter's diamond-tip was positioned at the top of the sample in the middle of its thinnest dimension using the nanoindenters camera. For nanoindentation a Berkovich diamond tip was applied.

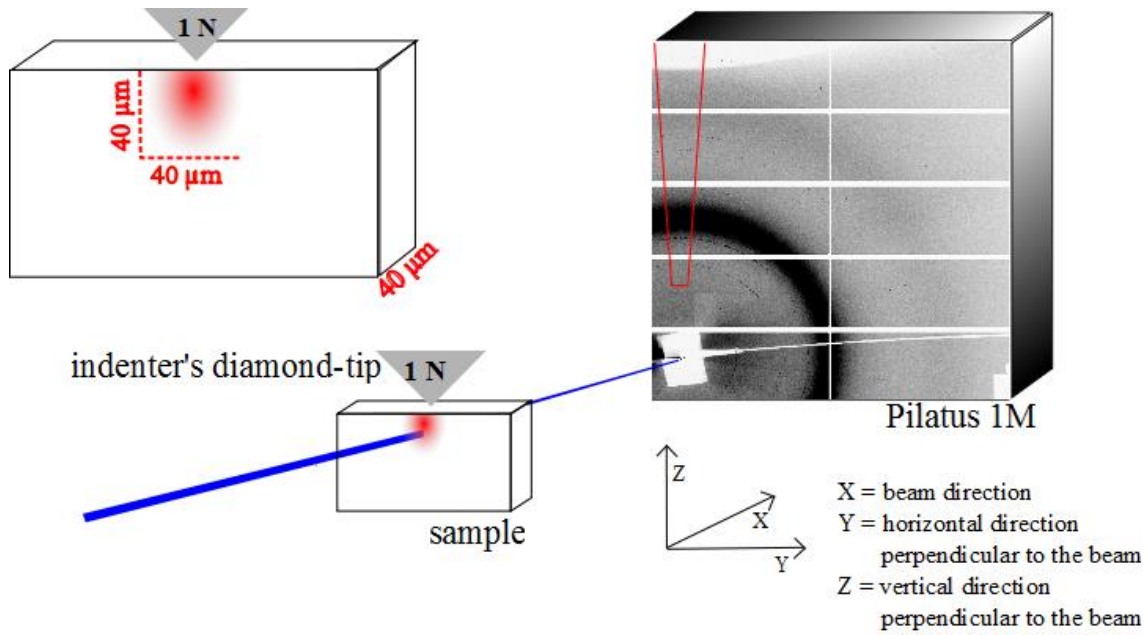


Figure 32: Schematic view of the X-ray nanodiffraction experiment. In the projection on the detector a real diffraction pattern obtained during a measurement is displayed; red lines define the area of integration which is 10° in width.

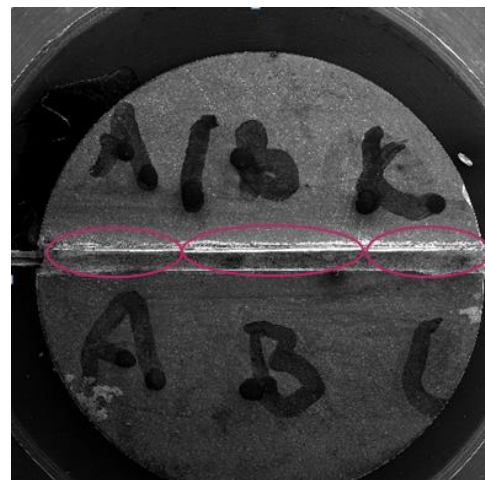
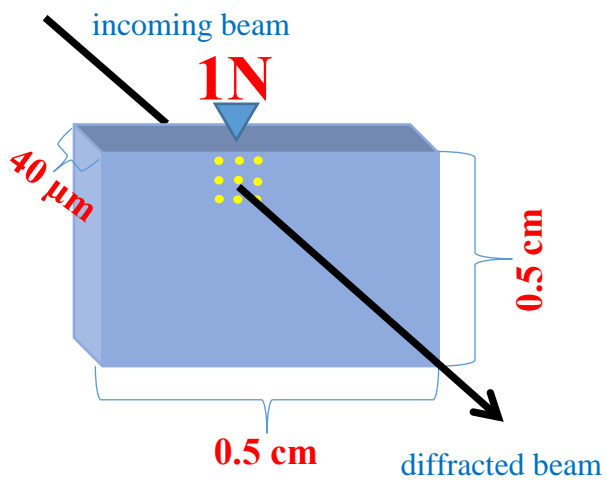


Figure 33: Sketch of the sample and diffraction experiment. The matrix scan for XRD measurement was realised beneath the Berkovich indenter-diamond-tip.

Figure 34: Slices of Zr-based amorphous plate samples placed on the indenter sample holder.

Spatially resolved X-ray diffraction scans were performed during the indentation using a nanometer sized monochromatic beam with an energy of 14.73 keV and a size of $250 \times 350 \text{ nm}^2$ (horizontal \times vertical) focused by Kirkpatrick-Baez mirrors (KB mirrors).

The size of the scanned sample area was $40 \times 40 \text{ }\mu\text{m}^2$ situated right beneath the indenter-diamond-tip. The nanoindentation of all three samples was realized in constant force mode.

This means that the applied force on the tip was kept to be persistent, 1 N, during the whole in-situ XRD experiments. The area beneath the Berkovich diamond tip was scanned with a step-size of 1.33 μm in both directions horizontal and vertical in order to map in detail the structural changes induced by nanoindentation. The total time of the measurement was 8.5 hours. In order to estimate the reference Q_0 value necessary for strain calculation, diffraction profiles were taken from the same area of the sample before applying any force on the Berkovich diamond tip almost touching the sample surface. In this case due to the lack of measurement time, we decided to use much bigger step-size of scanning ($10 \times 10 \mu\text{m}$ (horizontal \times vertical)) compared with the situation when the nanoindentation was realized. Then, the Q_0 value was determined for each sample as the mean value of positions of the first diffuse maximum from the data measured without application of force. The scanning experiments were realized by translating the whole nanoindenter set-up with the sample-holder in the plane perpendicular to the incoming X-ray beam (see *Figure 32*) with well-defined steps using a HEXAPOD with a resolution of 1 micron. XRD patterns were collected in transmission mode, by an area detector (Dectris, PILATUS 1M). One diffraction pattern was collected for 30 seconds. The sample to detector distance was 190 mm. Two-dimensional diffraction data were treated using the program package Fit2D [70]. The radial integration over a range of azimuth angle of 10° determined the diffracted intensity as a function of scattering vector Q . As can be seen in *Figure 36* we detected only a small part of the diffraction ring which was moreover a few times intermitted due to the segmented geometry of the PILATUS detector. Therefore we have decided to follow peak position changes along the direction in which the force was applied. The corresponding cake used for radial integration over an angular range of 10° is shown in *Figure 32* (red polygon). The profile of the principal diffraction peak was then modelled assuming a Gaussian function with a linear background. For each integrated diffraction pattern the shift in position of the first maximum Q_σ under the load of 1 N was determined with respect to the peak position Q_0 measured without load. The relative change of the peak position upon applying an external load σ defines the strain as elaborated in *Part 2*.

A very challenging process during the experiment was the alignment of the samples to be perpendicular to the incoming nanobeam and also the alignment of the indenter-diamond tip to be exactly in the middle of the investigated sample area. The alignment of the tip to the centre of a sample was done using the optical microscope which is included the indenter set-up. The alignment accuracy can be seen in *Figure 35-left*. In *Figure 35-right* one can see the

series of small indents which were created in order to localize the indenter-tip. Positioning of sample and indenter-diamond-tip was done on the base of absorption scans. For the determination of the surface of the sample in the vertical direction, see *Figure 36*, we used the absorption of the sample to determine the location of the surface. To find the area of interest in the horizontal direction was more demanding. The diamond-tip was above the sample and we did several absorption scans of the diamond-tip in horizontal direction at different heights with the goal to see absorption from the diamond. From these absorption scans we calculated those coordinates where the beam is directly beneath the indenter-tip.

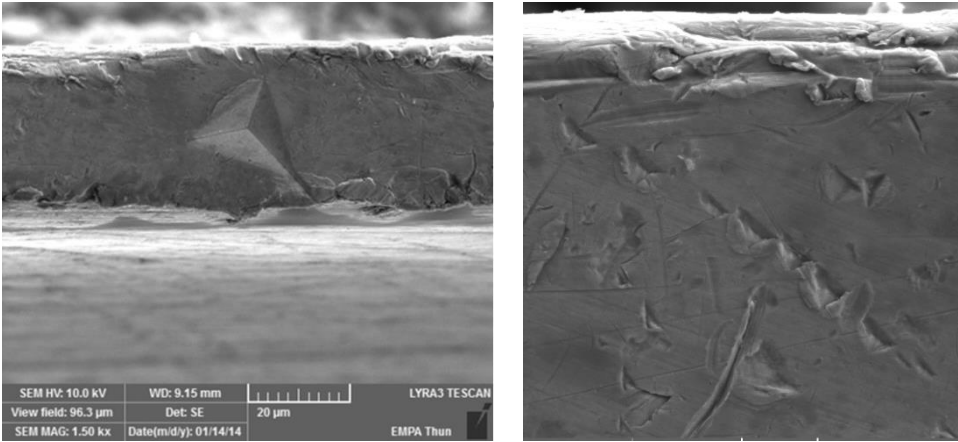


Figure 35 - left: The imprint of the Berkovich indenter-diamond-tip can be clearly seen in the centre of the sample top surface, right: localization of the middle of the sample top surface using a row of small imprints.

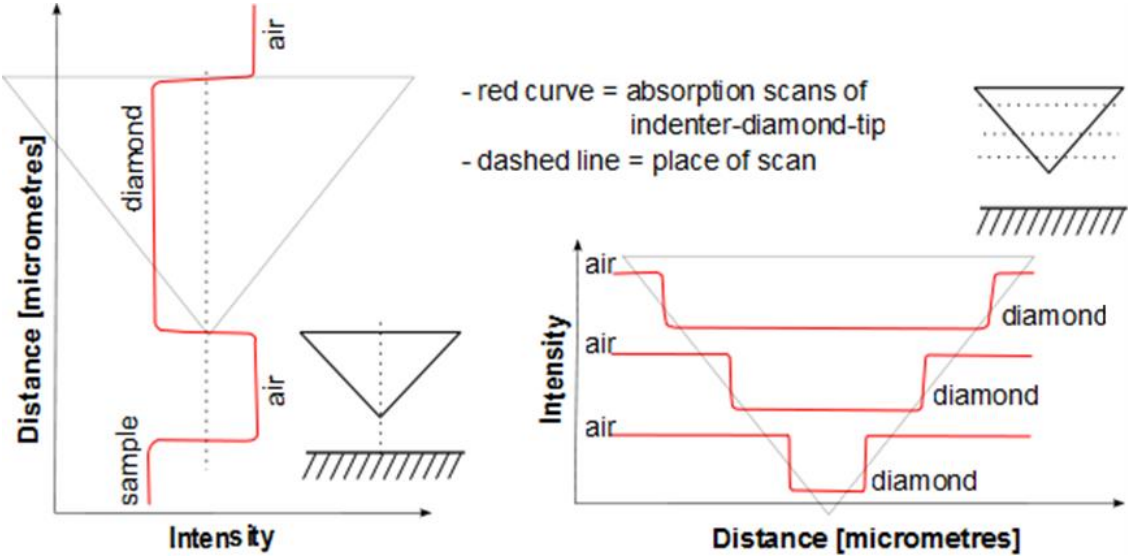


Figure 36: Schematic sketch of the positioning procedure of sample and indenter-diamond-tip to the incoming beam which was done by absorption scans (see text).

After defining the area of interest, in order to estimate Q_0 the matrix diffraction scan of the area of interest was done, *Figure 37-b*. As can be seen, without load the 2D map does not exhibit any significant gradient which could indicate the presence of a strain field induced in the sample. The slight gradient of values is in the interval 0.0005 and -0.0005 and can be connected with inhomogeneity of the sample or the sample was not exactly perpendicular to the beam. The mean value of first-diffuse-maxima positions from all diffraction patterns was determined to be $26.338 \pm 0.0016 \text{ nm}^{-1}$. In *Figure 37-a* the two-dimensional map of strain values obtained from diffraction data in the area of a $40 \mu\text{m} \times 40 \mu\text{m}$ beneath the position of the diamond-tip at the load of 1 N is shown.

A

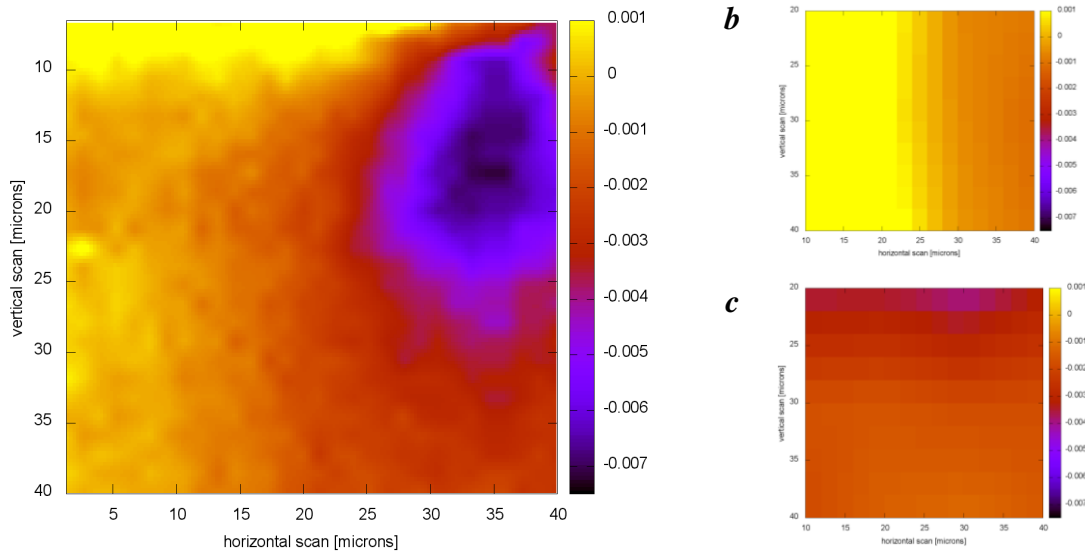
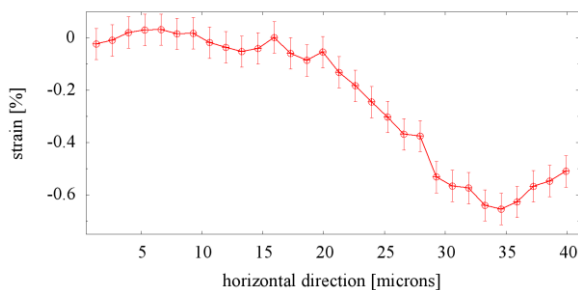


Figure 37: 2D map of strain values obtained from diffraction data in the area of a $40 \mu\text{m} \times 40 \mu\text{m}$ beneath the indenter-diamond-tip in the deformed volume of $\text{Zr}_{53}\text{Cu}_{18.7}\text{Ni}_{12}\text{Al}_{16.3}$ BMGs; a) strain field under load, b) before the indentation and c) after indentation.

A



b

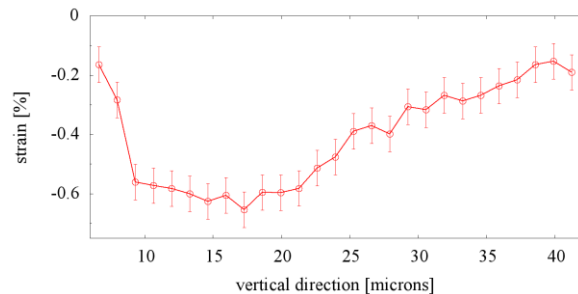


Figure 38-a and 38-b: Position dependence of the strains. Both plots were taken from picture 37-a from fixed Y - or Z coordinates. Left plot: $Y=35 \mu\text{m}$; right plot: $Z=19 \mu\text{m}$.

The centre of the strain field is localized at $Y = 35 \mu\text{m}$, $Z = 19 \mu\text{m}$. *Figures 38 - a* and *38 - b* show the position dependence of strains for fixed vertical ($Z = 19 \mu\text{m}$) and horizontal ($Y = 35 \mu\text{m}$) locations. One can easily see that the most impacted area around the centre of the strain field has a radius of about $2.5 \mu\text{m}$ in horizontal direction and $5 \mu\text{m}$ in vertical direction from the centre of the strain field. Then the influence of nanoindentation (with respect to the reference Q_0) is continuously diminishing, and at the edge of the scan area practically vanishes. The maximal and minimal measured strain values were 0.0014 , -0.0076 , respectively. The same area was measured also after removing the indenter-diamond-tip, *Figure 37-c* in order to map strains remaining in the sample after the indentation. Expect of the residual strains induced by indentation, there is no strain-field present in the sample after removing the indenter-tip.

The second investigated sample had the following composition: $\text{Zr}_{51.9}\text{Cu}_{23.3}\text{Ni}_{10.5}\text{Al}_{14.3}$. From the strain values calculated from a 10^0 cake, like in the above described experiment, we obtained the two-dimensional map of strains shown in *Figure 39-a*. The measured area was $40 \mu\text{m} \times 40 \mu\text{m}$ beneath the position of the diamond indenter. The centre of the strain field is localized at $Z = 35 \mu\text{m}$, $Z = 19 \mu\text{m}$.

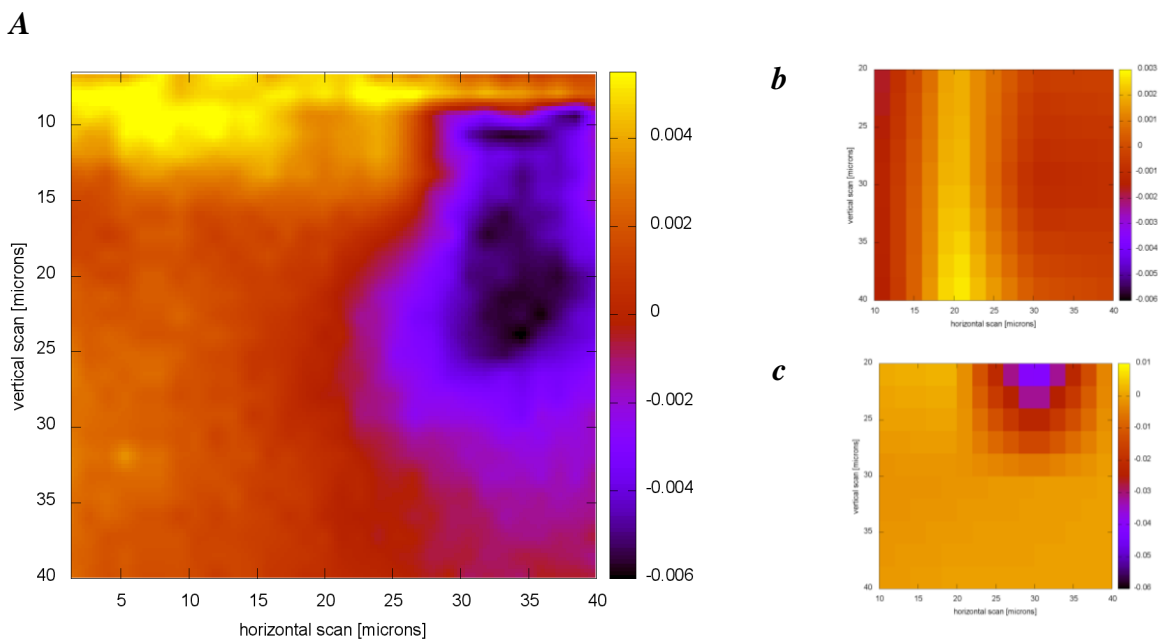


Figure 39 a-c: 2D map of strain values obtained from diffraction data in the area of a $40 \mu\text{m} \times 40 \mu\text{m}$ beneath the indenter-diamond-tip in the deformed volume of $\text{Zr}_{51.9}\text{Cu}_{23.3}\text{Ni}_{10.5}\text{Al}_{14.3}$; a) strain field under load, b) before the indentation and c) after indentation.

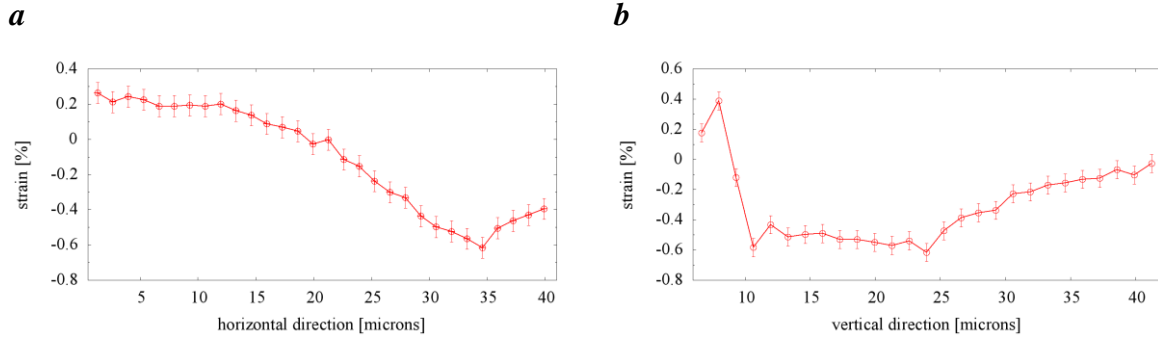


Figure 40: Position dependence of the strains. Both plots were taken from 2D maps picture 42-a for fixed Y- or Z coordinates, a) $Y=35 \mu\text{m}$; b) $Z=19 \mu\text{m}$.

At first glance one can see that the tiny change in sample composition causes a big change in the dimension of strain field. It is twice larger than in the previous case.

The most impacted area around the centre of the strain field has an extension in horizontal direction of $5 \mu\text{m}$ and in vertical direction of $7.5 \mu\text{m}$, Figure 40 a and b. Then the influence of the indent is continuously decaying. The matrix scan was done also before indentation in order to obtain Q_0 for the calculation of strains, Figure 39-b. The mean value of the first-diffuse-maxima positions was determined to be $26.440 \pm 0.0008 \text{ nm}^{-1}$. The behaviour of the sample after removing the indenter-diamond-tip is demonstrated by the 2D-map in Figure 39-c. In this case one can observe, in the place of the indent, a change in the strain values. According to our opinion it is connected with plastic deformation of the material including residual elastic strain.

The last measured sample was $\text{Zr}_{50.7}\text{Cu}_{28}\text{Ni}_9\text{Al}_{12.3}$. Again a two-dimensional map of strain values was obtained from diffraction data in the area of a $40 \mu\text{m} \times 40 \mu\text{m}$ beneath the diamond indenter, see Figure 41 a, b and c. The mean value of first-diffuse-maxima positions from all diffraction patterns was determined to be $25.579 \pm 0.0017 \text{ nm}^{-1}$. The centre of the strain field is localized outside of our 2D map in horizontal position and in vertical position at $Z = 20 \mu\text{m}$. From the location we can quantitatively determine the impact of the strain field created by the Berkovich tip at a load of 1 N.

A

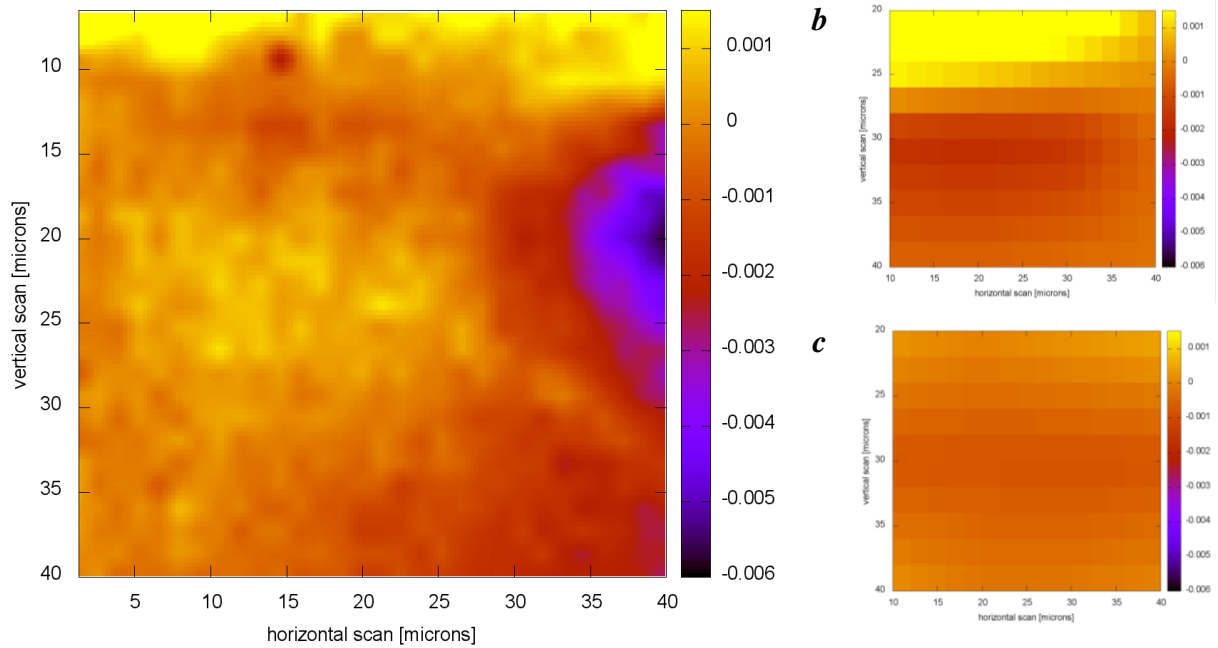


Figure 41 a-c: 2D map of strain values obtained from diffraction data in the area of a $40 \mu\text{m} \times 40 \mu\text{m}$ beneath the indenter-diamond-tip in the deformed volume of $\text{Zr}_{50.7}\text{Cu}_{28}\text{Ni}_9\text{Al}_{12.3}$ BMGs; a) strain field under load, b) before the indentation and c) after indentation.

The strain fields of all three measured samples look very similar, because according to literature these materials exhibit very similar mechanical properties. Differences in shape of strain fields are according our opinion caused mostly by small differences in shape of individual samples.

3.7 In-situ experiment at end-station ID11

ID11 is a multipurpose, high flux and high energy beamline, situated at the European synchrotron radiation facility (ESRF). Main focus area of the instrument is 3D grain mapping, diffraction, and PDF experiments in the field of materials science. The beamline offers a high flux at high photon energy (18-140 keV). The beam dimension can be tuned from a few mm down to 100 nm. A double bent crystal monochromator operating in horizontal Laue geometry is used to select the energy/wavelength of the beam. The light source at ID11 is an in-vacuum undulator. The beamline has two experimental stations EH1 and EH3. To focus the beam, ID11 has an in vacuum transfocator, which consists of 8 cylinders with 1, 2, 4, 8, 16, and 32 Be lenses, 32 and 64 Al lenses, and one with a pinhole. By combining these sets of lenses it is possible to focus throughout the entire energy range in EH3 and up to 70 keV in EH1. The experiments described here were done in EH3. EH3 contains a high resolution diffractometer, situated 94 m from the source. This station was built to carry out experiments with ~1 micron spatial resolution. EH3 has an additional dedicated optical system offering a range of focussing techniques [74].

Table 6

Selected properties of $Zr_{53}Cu_{18.7}Ni_{12}Al_{16.3}$, from literature [82].

experiment geometry	Transmission
type of indenter	Wedge
hardness	550 Hv
elastic modulus	102 GPa
depth of indent	0.8 μm for load 300 mN

Based on the results of the P03 experiment, discussed in the Chapter 3.6, we knew that it is possible to observe changes in the strain field as a function of the applied force on the tip. In contrast to the previous experiment this experiment was performed with a wedge indenter which allows us to neglect the gradient of deformation within the thickness of the material.

The main objective of this experiment was to verify the outputs from the previous in-situ P03 experiments where we combined nanoindentation and X-ray nanodiffraction for obtaining a full picture of strain distribution appearing beneath the indenter during loading of the amorphous alloys. The investigated sample has the shape of a block with nominal composition $Zr_{53}Cu_{18.7}Ni_{12}Al_{16.3}$. Its preparation technique and shape is described in Chapter 3.1. The experimental setup is schematically described in *Figure 42 and 43*.

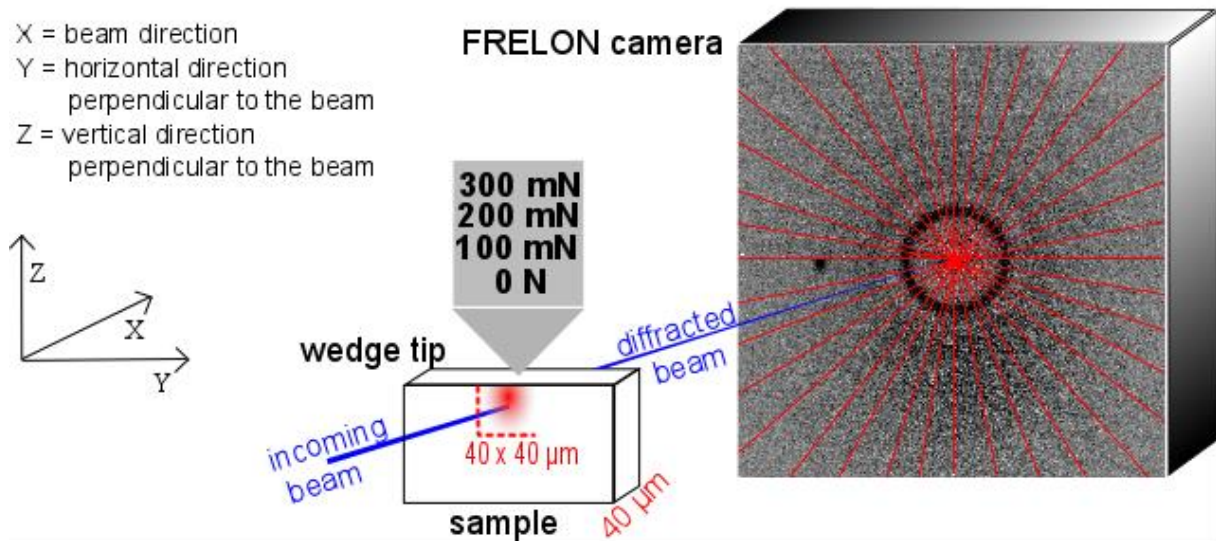


Figure 42: Schematic view of the X-ray nanodiffraction experiment. In the projection on the detector a real diffraction pattern obtained during measurement is displayed. Red lines show the areas for caking.

Spatially resolved X-ray diffraction scans were performed during the indentation using a nanometer sized monochromatic photon beam with energy of 65.435 keV and size $500 \times 500 \text{ nm}^2$. The size of the sample area scanned was $30 \times 30 \text{ μm}^2$ situated right beneath the indenter diamond tip. The scanning experiments were realized by translating the whole nanoindenter set-up with the sample-holder in horizontal and vertical directions lying in the plane perpendicular to the incoming X-ray beam, see *Figure 42*, with well-defined steps of 1 micron. XRD patterns were collected in transmission mode by a FRELON camera with pixel size of $50 \times 50 \text{ μm}$. One diffraction pattern was collected for 30 seconds. Two-dimensional diffraction data were treated using the program package Fit2D [70]. We detected a full picture of the diffraction ring, so the deformation tensors could be calculated according to the procedure describe in the Part 2. The footprint of the wedge indenter on the sample surface can be seen in the *Figure 44*.

After every completed X-ray scan the applied load was increased by about 100 mN keeping the tip permanently touching the sample at the same position, see *Figure 45*. In this way we covered forces from 0 to 300 mN. The reference Q_0 value was determined from the data measured without application of force. Its value was determined to be $26.475 \pm 0.0011 \text{ nm}^{-1}$. The total time of the measurement at one load was 8.5 hours. The depth of the indent was 0,8 μm for a load of 300 mN.

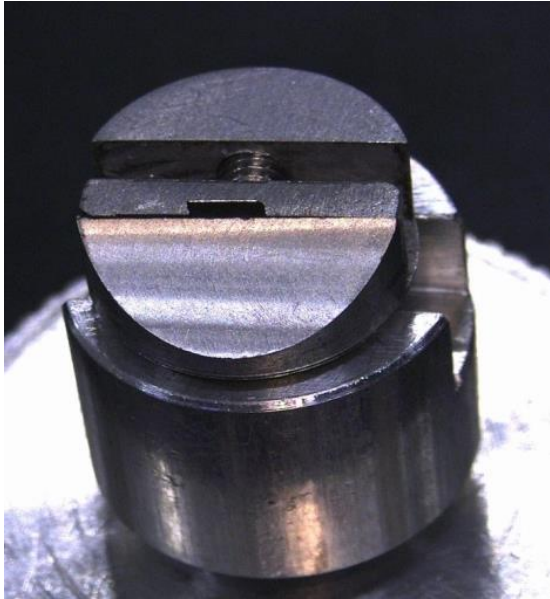


Figure 43:
Slice of Zr-based amorphous plate samples placed in the indenter sample holder.

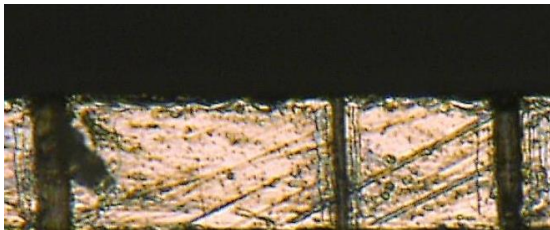


Figure 44:
Top of the sample after indentation by the wedge indenter.

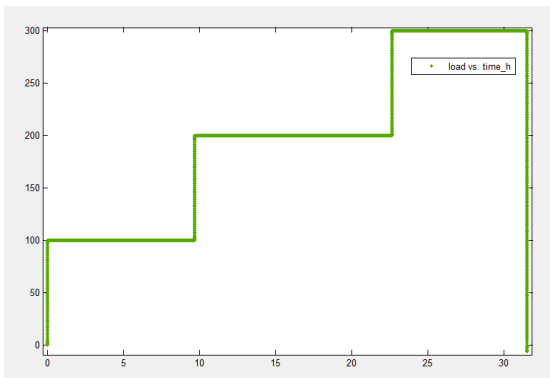


Figure 45:
Load versus time curve of the indentation experiment, where the load was increased about 100 mN after every completed X-ray scan. The horizontal axis shows the experiment time in hours.

The situation is a bit different in comparison to the previously described experiment realized at beamline P03 because we used a wedge indenter-diamond tip. In the case of a quantitative

analysis the variation of strains connected with the sample thickness does not need to be taken into account. So the three dimensional case was reduced to a two-dimensional case.

2D maps of each load are displayed in *Figures 46 – 49*. One can clearly identify not only the position of the elastic deformation field but also its shape. From the calculation of the deformation tensor its range of values was determined and also values for the normal- ε_{11} and ε_{22} and shear- γ components were calculated.

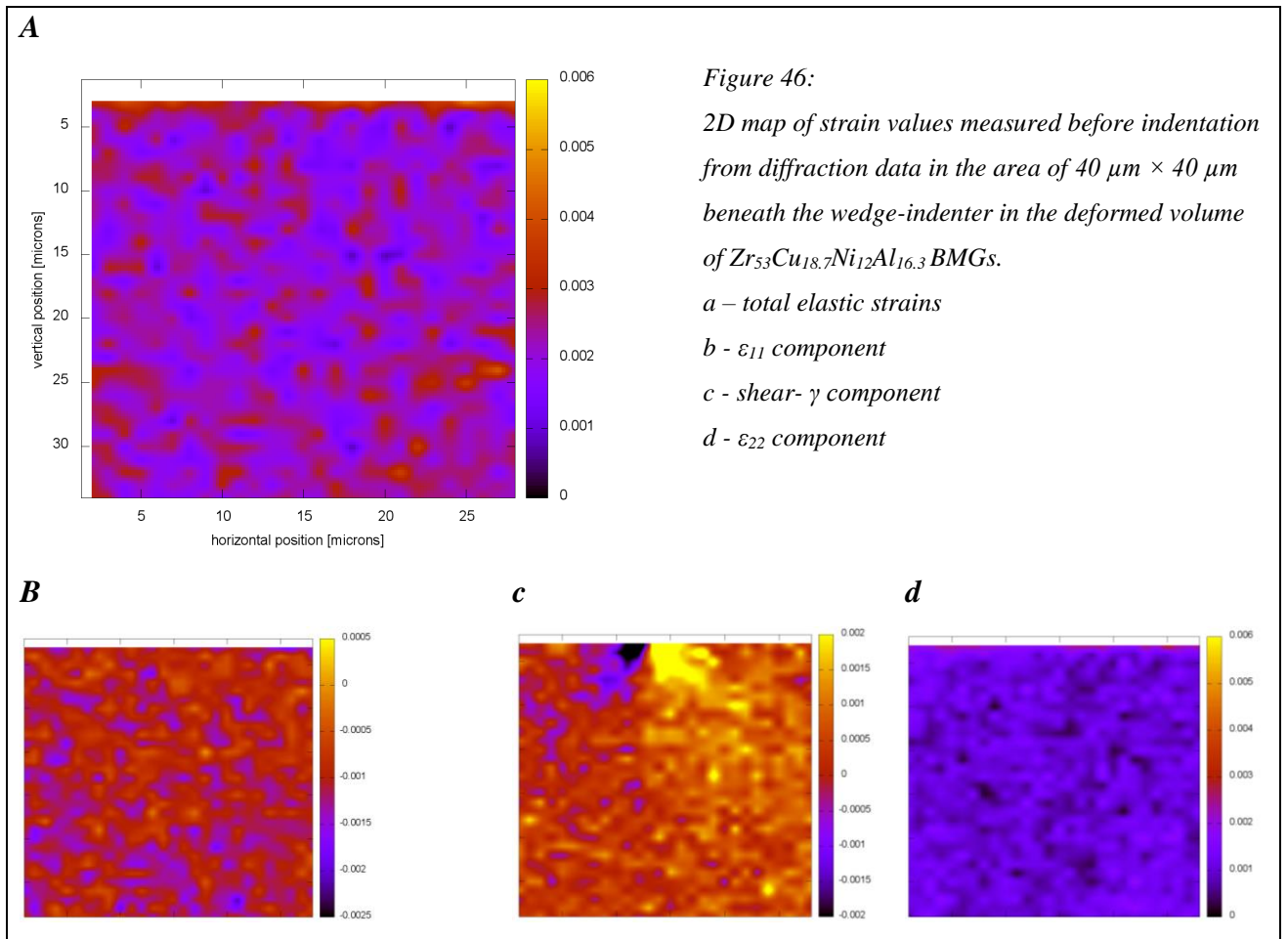


Figure 46 shows 2D maps of strain values and tensor components measured before indentation. All values in each 2D map oscillate around 0.

Figure 47 show 2D maps of strain values and tensor components measured during the indentation at load 100 mN. Two microns from the indented top of the sample are values of the total elastic strains do not oscillate around zero. The interesting feature – at the place of the indent (green arrow in *Figure 47*) are strain values are lower compared to the regions around this position. This is connected with the fact that at the place of the edge of the

indenter tip, which is pressing into the sample, there is maximal plastic deformation and minimal elastic deformation. X-ray diffraction is sensitive to elastic deformation, therefore such behavior. We can observe the gradient of values, with a maximal strain value of 0,0059. The biggest change is observed on 2D map of ε_{22} component which is parallel to applied load and corresponds to compressive deformation.

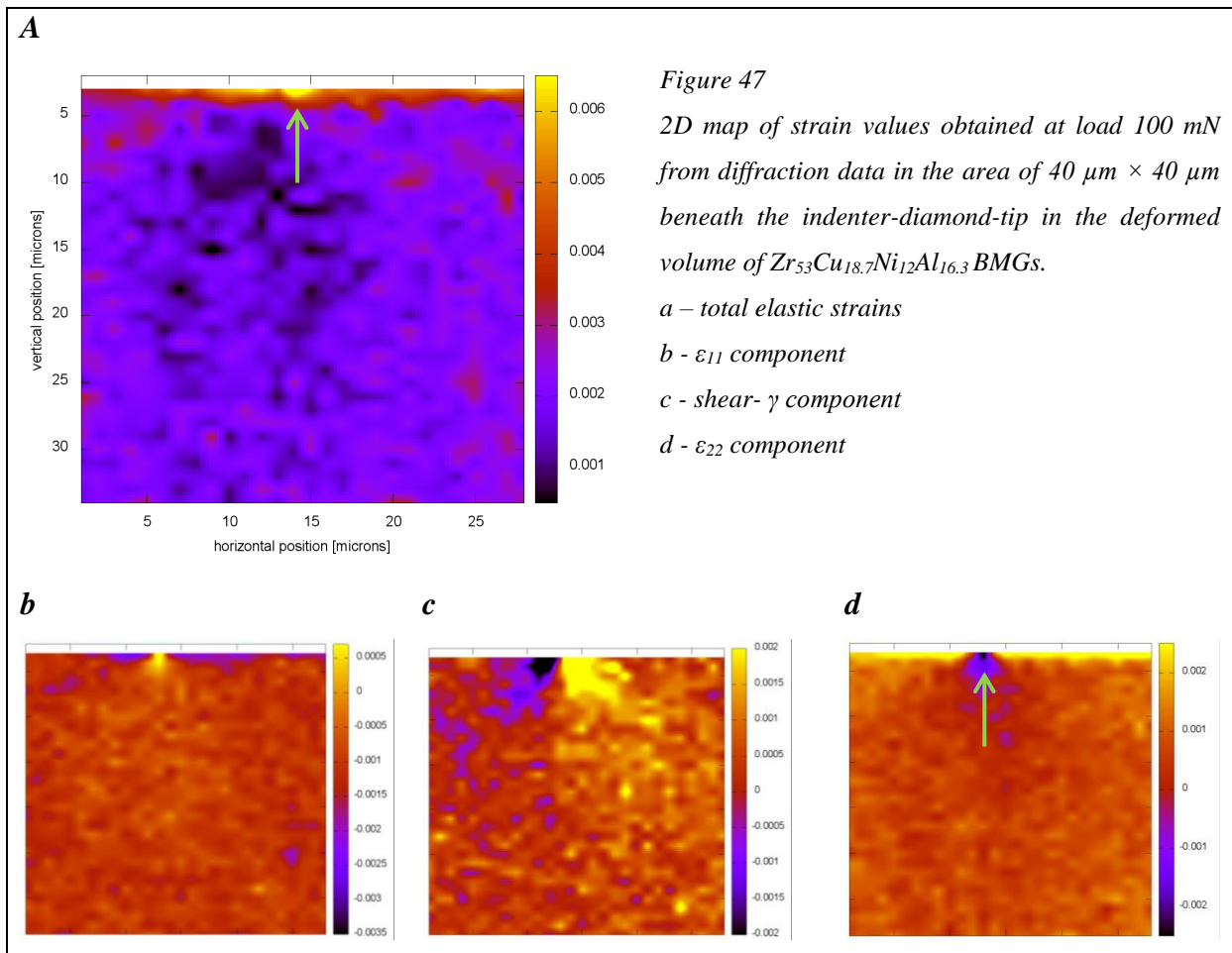
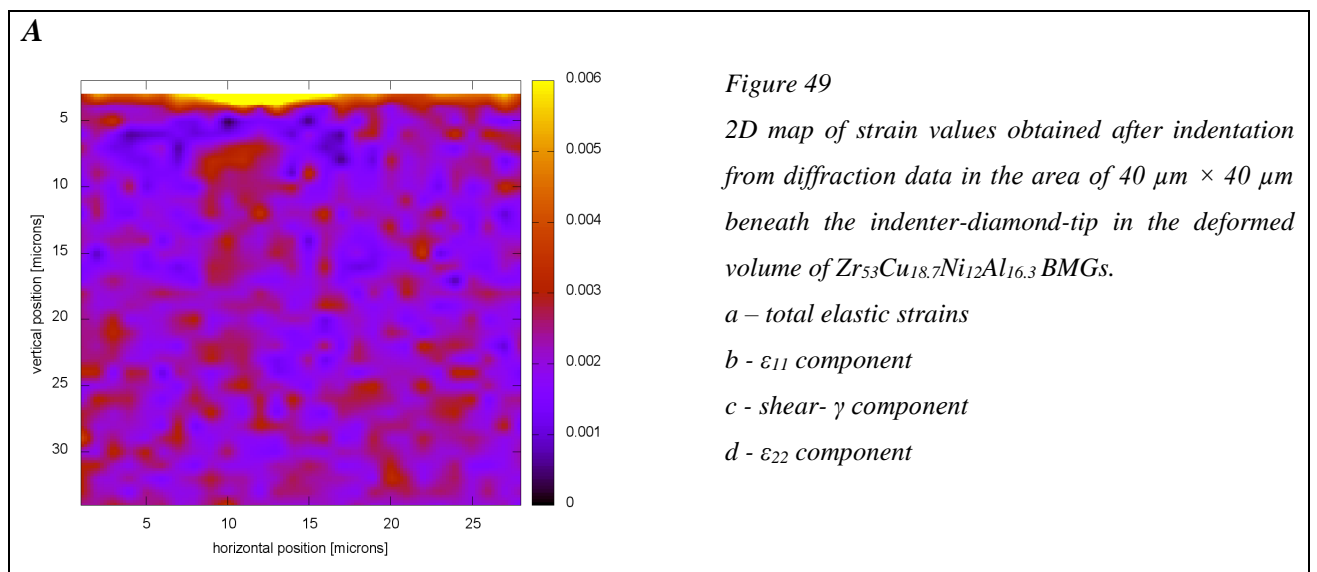
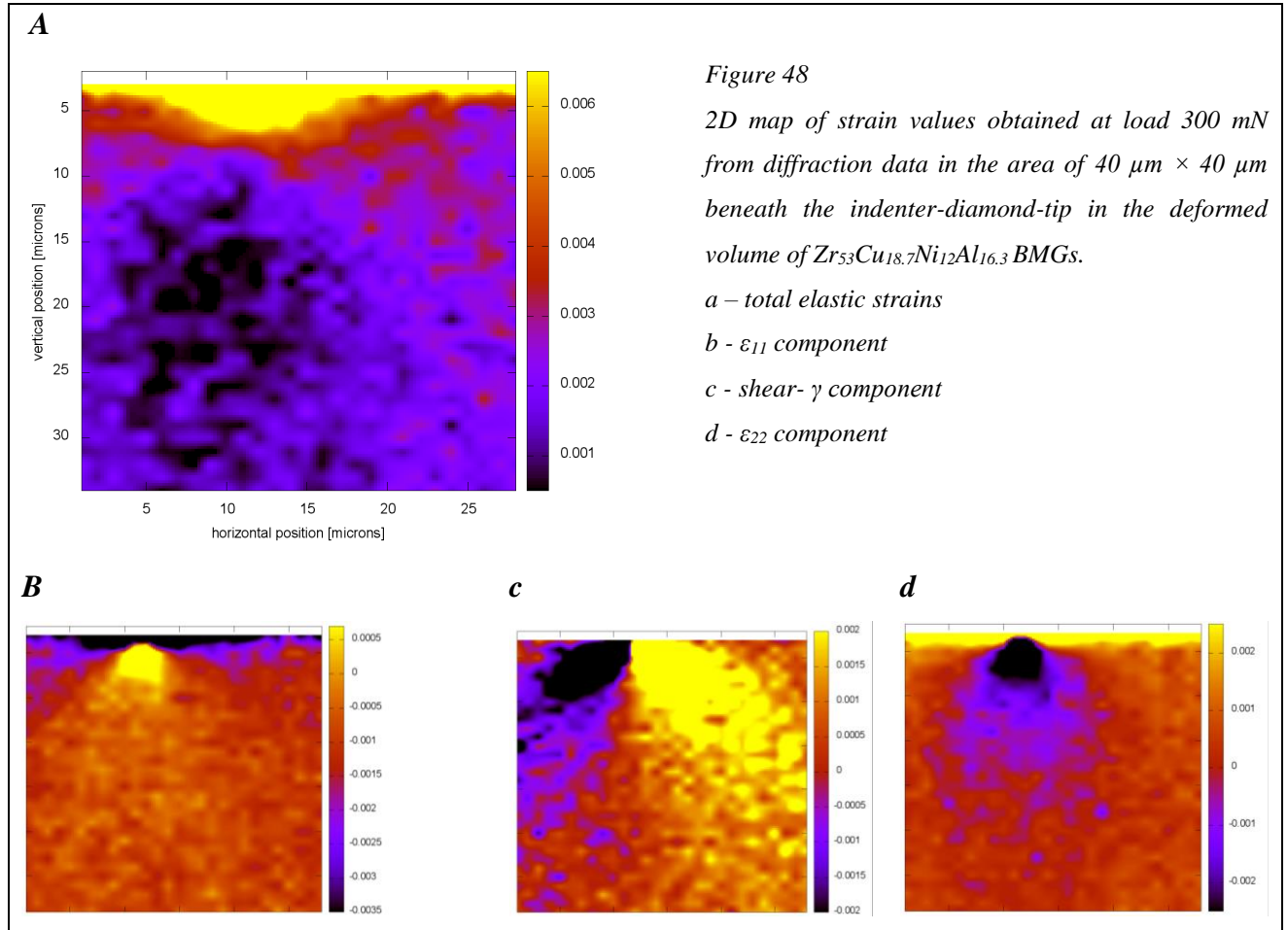


Figure 48 shows 2D maps of strain values and tensor components measured during the indentation at a load of 300 mN. The highest values of elastic deformation are observed more than seven microns from the indented top of sample (yellow colour in the *Figure 48 -a*). Then the deformation gradually decreases. The fact that the strain field in *Figure 48 -a* extends more to the side (in contrary to previous in-situ experiment) is connected with the wedge shape of the indenter-diamond-tip which covers the full thickness of the sample. All material within the sample thickness is pushed to the side, which is detectable by X-ray – elastic deformation. The maximal strain value is 0,0064. Values for the other deformation tensor components also increase with increasing load.

During the experiment, at load 200 mN, we had problem with beam and physically we do not have data for 2D map as in the other loads. Fortunately, the data for draw the *Figure 46* were recorded and gradual increase of strains with increasing of load is evident.



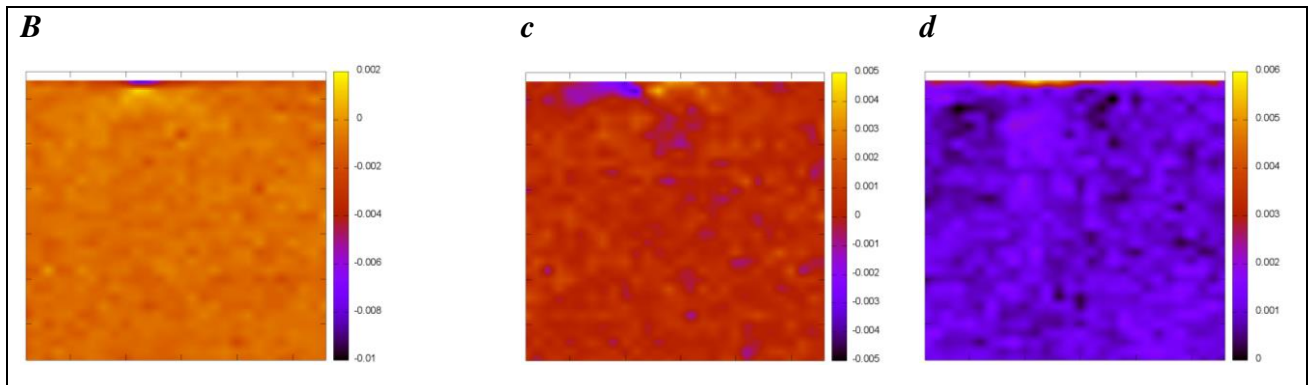


Figure 49 show 2D maps of strain values and tensor components measured after the indentation. Values of all components of the deformation tensor oscillate around zero. Only a small gradient of strain values at the place where the sample was indented is observable – these are residual strains induced to the sample. This measurement was done immediately after the load 300 mN was removed and we can see that elastic deformation vanishes, as it should be.

The centre of the strain field is localized at the horizontal coordinate $Y = 12 \mu\text{m}$ for each load. The most impacted area around the centre of deformation is continuously growing with increasing of load. This behaviour is demonstrated in Figure 50, showing the position dependence of the deformation for a selected fixed vertical and horizontal position.

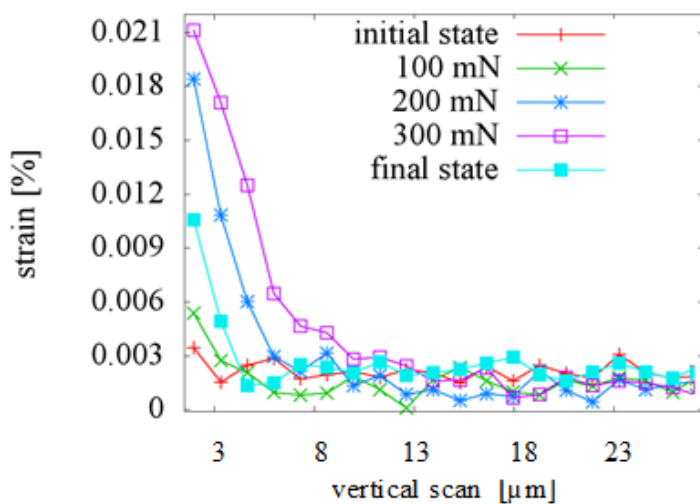


Figure 50:
Position dependence of the strains measured for horizontal coordinate $Y=12 \mu\text{m}$. X coordinate determines the distance from the top (surface) of the sample.

Most representative is the curve measured at 300 mN which can be divided into two parts. The first part ends 10 microns from the indented surface of the sample. The first part is characterized by the maximal change of strains. The depth of indent is 0.8 micron. According to literature, the deformation of materials extends nine times the depth of the indent which is in our case 7.2 micron. This is exactly displayed part of curve in *Figure 50*. The behaviour of elastic strains at 300 mN will be compared with FEM analysis in the next Chapter.

Discussion

Discussion will follow and explain individual steps and clarify partial results presented in the experimental section. These results, especially mechanical readings are compared with results obtained from available literature. More or less the literature discusses mostly shear bands initialization and shear flow, the effect of uniaxial compression and compares properties of bulk and ribbon material and computational modelling. To our knowledge, *in-situ* characterization of amorphous materials by diffraction methods and nanoindentation has not been reported, so the confrontation with literature is in some cases not possible. Therefore, using Finite Element Method, the theoretical strain-fields were calculated and compared with experimental readings.

The aim of this work was to implement and to test a set-up for experiments on the connection of mechanical and structural properties of materials. We decided to do it by connection of nanoindentation and diffraction. Strain calculation on disordered systems obtained from position of diffuse maximum was reported only few times, mostly from a theoretical viewpoint [71]. We found that diffuse maxima are equally sensitive to applied load as Bragg peaks in crystalline materials.

By comparing of experimentally obtained strain fields and FEM simulated strain fields we see almost perfect matches (*Figures 53, 54, 58, 59, 60*). This we assume as important step for the further development of this method.

In this work FEM was used to correlate mechanical and structural properties of amorphous materials. FEM analysis was not done by myself but by my colleague from Slovak Academy of science, Dušan Németh [66]. FEM simulation included in this work have one specific feature, these were calculated only on the base of sample characteristics like their chemical composition and thicknesses, without concrete information about their mechanical behaviour.

Such strategy was chosen with the aim not to influence calculations and thus to obtain completely independent result from our experimental findings.

Ex – situ experiments

Ex – situ experiments, employing endstations P06 and P02 in DESY, were done on the same sample $Zr_{52.5}Ti_5Cu_{17.9}Ni_{14.6}Al_{10}$. One sample had the form of a rod and the second sample the form of a plate. In both cases samples were indented before the X-ray experiment.

P06 - DESY

The main reason for the lack of studies which aims to extract “strain information” from diffraction patterns is that the signal obtained from amorphous materials has been considered too broad to provide such information. Moreover the amorphous signal from laboratory X-ray sources is too weak in intensity compared to the unavoidable background for extracting such information.

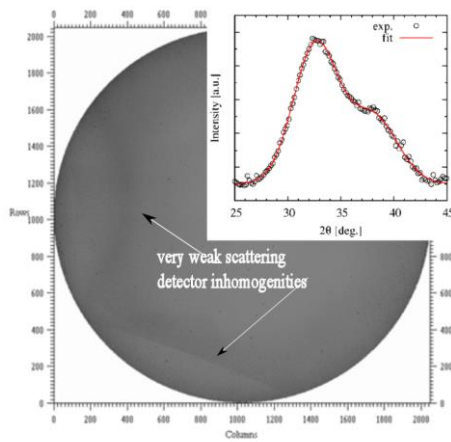


Figure 51: Diffraction pattern obtained from the detector and integrated diffraction pattern.

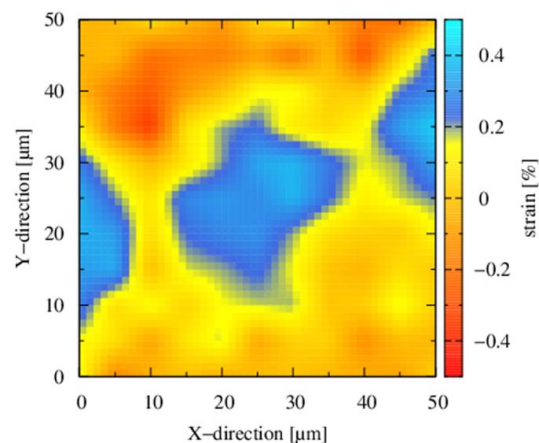


Figure 52: 2D strain map calculated from second diffuse maxima.

The aim of our first ex-situ experiment, described in section 3.3, was to clarify if there is the possibility to see the subtle difference between deformed and non-deformed amorphous material by X-ray diffraction. Only this one experiment was done in reflection mode therefore

the obtained results cannot directly be compared with the other experiments. Nevertheless the method of data evaluation is similar like in the other experiments. *Figure 51* shows the raw 2D diffraction pattern. As one can see, the diffraction pattern is characterized by a very weak scattering signal indicated by the arrow at the right side of the detector. Moreover, due to the geometry of the experiment, the first diffuse diffraction ring was not measured, so our strain calculations are based on the position change of the second diffuse ring, *insert Figure 51*.

From this experiment we found that using X-ray diffraction we are able to localize the indent on the base of relative changes of elastic residual strains within the measured 2D maps. From our experiments we can only qualitatively evaluate the residual elastic strains which are induced in the sample during the indentation.

P02.2 and P02.1 - DESY

The aim of experiments was to detect the deformation field in amorphous material around the indent. From high quality diffraction data we have calculated axial, plane and tangential components of deformation tensors and we compared experimental data with FEM analysis.

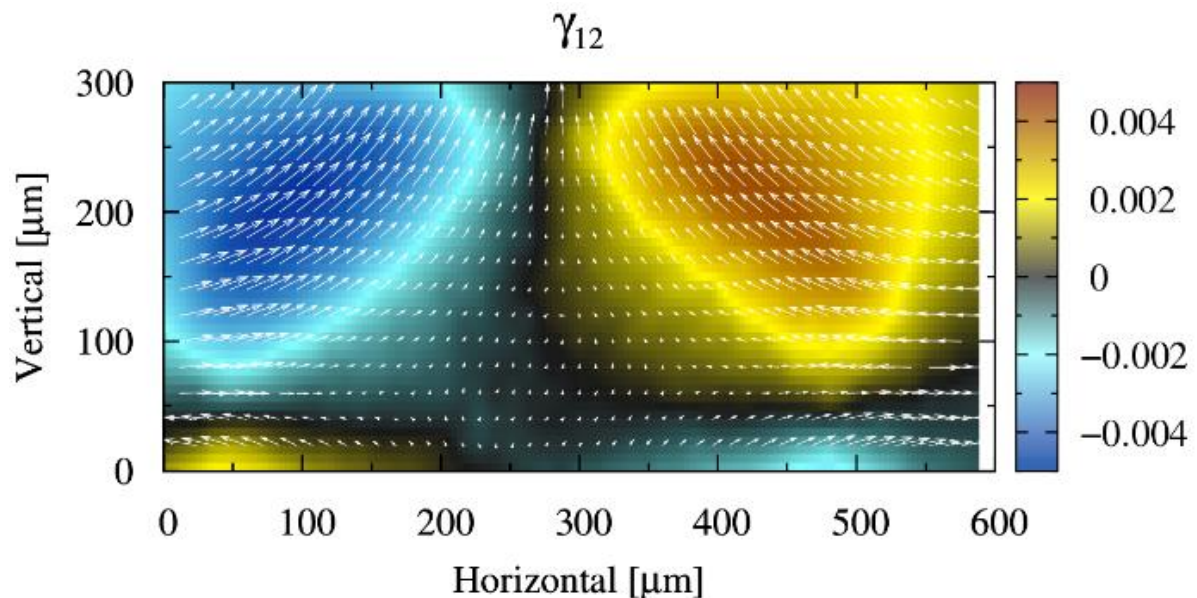
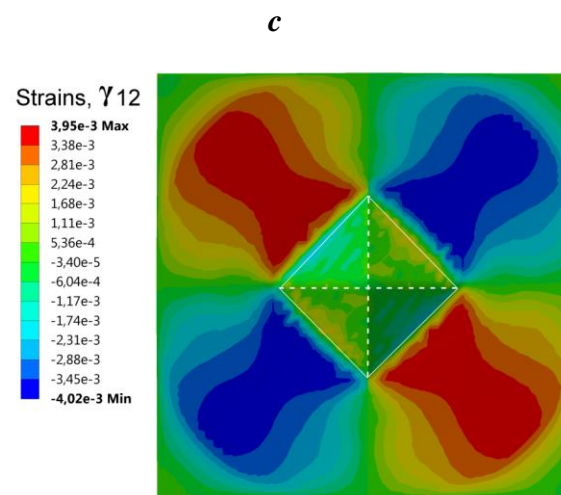
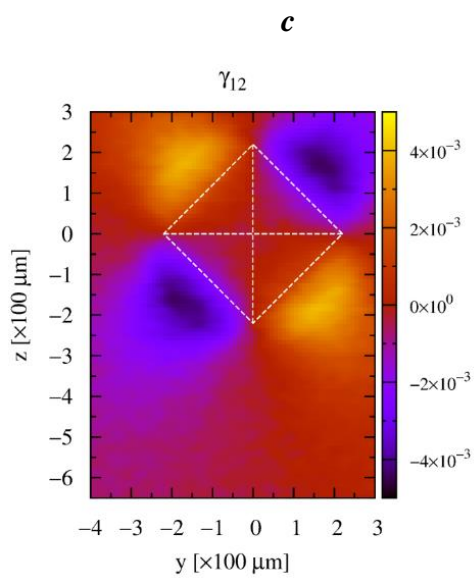
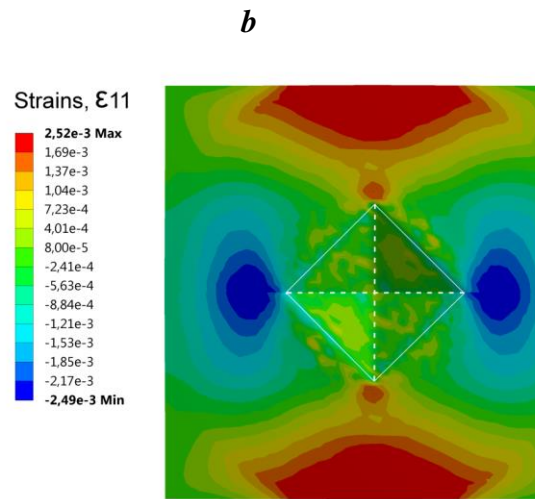
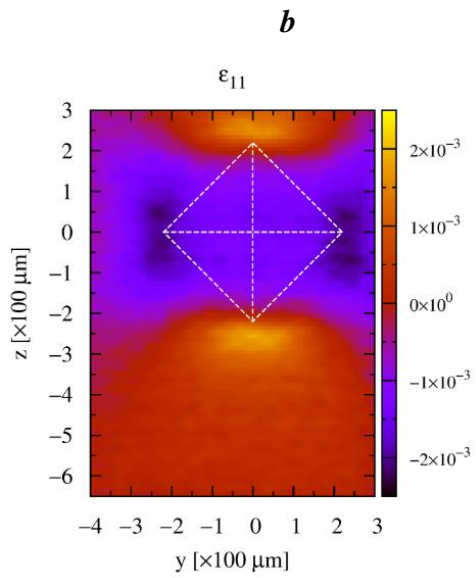
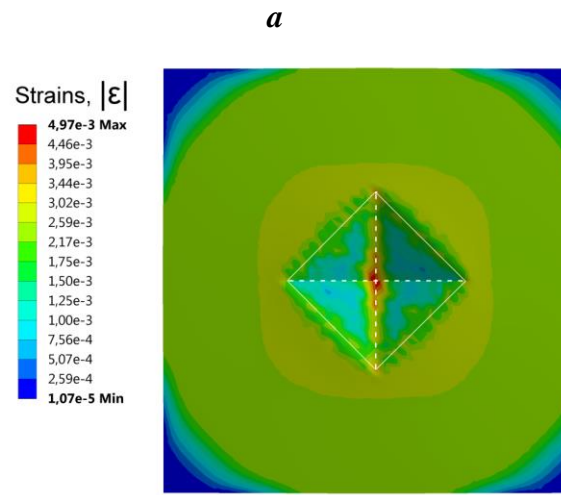
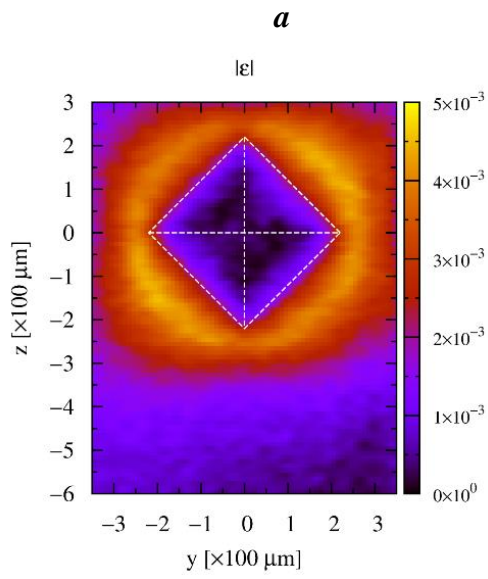


Figure 53: Shear component (γ_{12}) of the deformation tensor displayed in tensor format for each diffraction pattern measured at P02.2.

Our analysis, deformation tensor calculation, offers the feature to determine from each diffraction pattern not only the size of the elastic strain but also its direction, *Figure 53*.



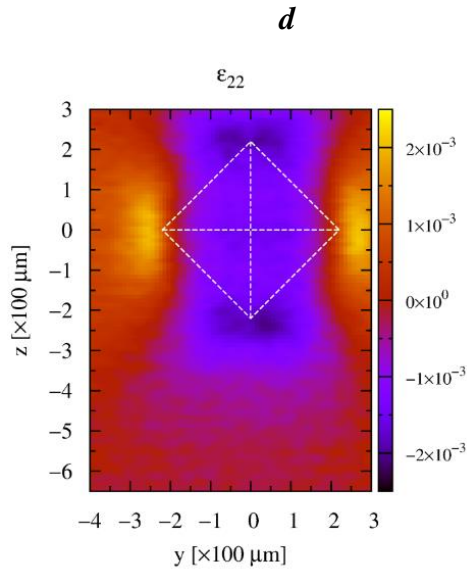


Figure 54: 2D map of total strain values $|\epsilon|$ and axial (ϵ_{11}), planar (γ_{12}) and tangential (ϵ_{22}) components of the deformation tensor, obtained from diffraction data in the indented $Zr_{52.5}Ti_5Cu_{17.9}Ni_{14.6}Al_{10}$ BMGs.

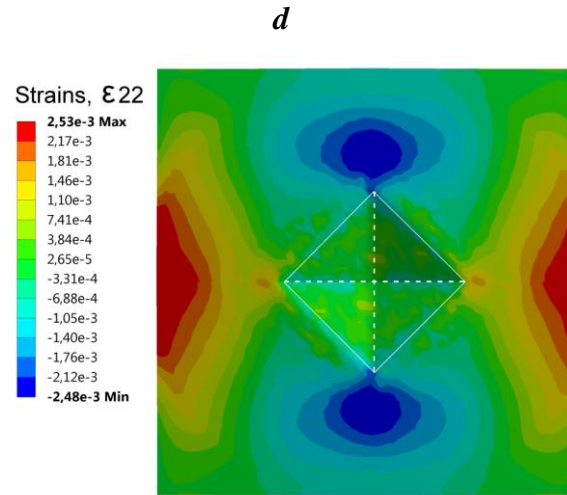


Figure 55: 2D map of total strain values $|\epsilon|$ and axial (ϵ_{11}), planar (γ_{12}) and tangential (ϵ_{22}) components of the deformation tensor, calculated using FEM on $Zr_{52.5}Ti_5Cu_{17.9}Ni_{14.6}Al_{10}$ BMGs.

Comparing the experimentally obtained 2D maps *Figure 54* with theoretically calculated 2D map (each value of strain is the average value obtained from 25 values simulated within the thickness of sample) *Figures 55* shows that the strain fields $|\epsilon|$, *Figures 54-a* and *55-a*, and tensor components, *Figures 54-b, c, d* and *55-b, c, d*, are very similar. From $|\epsilon|$ one can clearly identify not only the position of the indent but also its shape. Strains $|\epsilon|$ obtained experimentally and by FEM show only small differences in value. Very likely this is connected to the fact that with X-rays we see only the elastic part of the deformation, while FEM calculations take the total deformation into account (elastic and also plastic part). This effect can be seen most prominently at the location of the centre of the indent (the position $y=0$ and $z=0$ in *Figure 54-a*). In the calculated map (*Figures 55-a*) is clearly visible that at this place the total strains are maximal, but in the measured map total strains in the position of indent are minimal. On the position of the edge of the indent mostly plastic deformation is present – which is not reflected in a shift of the diffuse maximum measured by X-ray diffraction, so our data shows minimal strain values. When FEM is focused just on one component of the deformation tensor, axial (ϵ_{11}), planar (γ_{12}) or tangential (ϵ_{22}), the values are the same like in measured results.

In summary, from this ex-situ experiment we learned that using of high-energy X-rays and suitable analysis tools, the full strain tensor can be derived directly from the diffraction signal of amorphous materials. The strain resolution for this technique is of the order of 10^{-4} , comparable to strain scanning methods applicable to crystalline materials. Using X-ray diffraction the direction of the deformation tensor components can be calculated. Such information cannot be derived from other standard techniques which deal with mechanical properties of materials.

When we take into account that FEM is a many times verified method for simulation of mechanical properties of different materials, we can conclude from our analysis, that the established method for strain calculation is suitable and can be used for different material characterization. Moreover, we can say that the correlation of mechanical and structural properties in the suggested way (nanoindentation and diffraction) provides information about the structure and strain state of materials. From the qualitative and also the quantitative side the model follows the experimental data. In light of these results our next step was to design in-situ nanoindentation X-ray experiments in transmission geometry.

***In – situ* experiments**

In – situ experiments, employed the endstations P03 at DESY and ID11 at ESRF. As sample material we used amorphous $Zr_{53}Cu_{18.7}Ni_{12}Al_{16.3}$, $Zr_{51.9}Cu_{23.3}Ni_{10.5}Al_{14.3}$ and $Zr_{50.7}Cu_{28}Ni_9Al_{12.3}$ glasses. Samples in the form of plates $1 \times 1 \text{ cm}^2$ and with a thickness of $40 \mu\text{m}$ were used for the in-situ indentation experiments.

DESY-P03

The main objective of this in-situ experiment was to obtain a full picture of the strain distribution beneath a pyramidal (Berkovich) indenter. The strain field under the indenter in loaded condition was mapped by rastering a nano-beam and analysing the diffraction patterns.

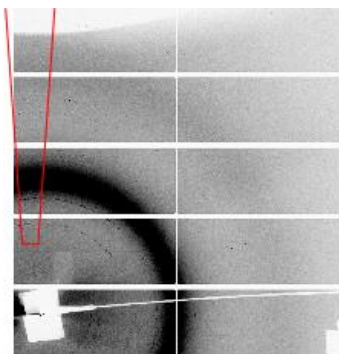


Figure 56:
Diffraction pattern on the 2D-detector. One can see its segment character. The red polygon indicated the cake which was radially integrated.

The data analysis was limited by the quality of the obtained diffraction patterns, *Figure 56*. Due to the segmented character of the employed detector and the fact that not the full diffraction pattern was detected, it was not possible to calculate all components of the deformation tensor. Therefore, we calculated strains induced in the sample during its deformation by following the position of first diffuse maxima in direction of the applied stress.

In *Figure 57* the FEM model of indented $Zr_{53}Cu_{18.7}Ni_{12}Al_{16.3}$ sample loaded at 1 N is shown. The similarity between experimentally obtained and calculated 2D maps is visible in *Figures 58* and *59*. The centre of the strain field is shifted towards the right side with the aim to observe the radius of the influenced area. One can see that the strain fields are very similar and also the centre of strains is similarly far-away from the top. According to literature the size of the strain field in the case of using a Berkovich indenter is directly connected to the depth of the indent. Its size is nine times the depth along the loading direction and four times to the side. In this case the indent has a depth of 4 microns, so the material is feeling the elastic deformation 36 microns from the indented surface of the sample and 8 micron to each side from the position of the indent. From experiment and also simulation, bottom *Figures 58* and *59*, radius of the main impact of elastic strains beneath the indenter is 10 microns (with the centre at 17 micron beneath the indenter tip). Then the strength of elastic strains gradually decreases.

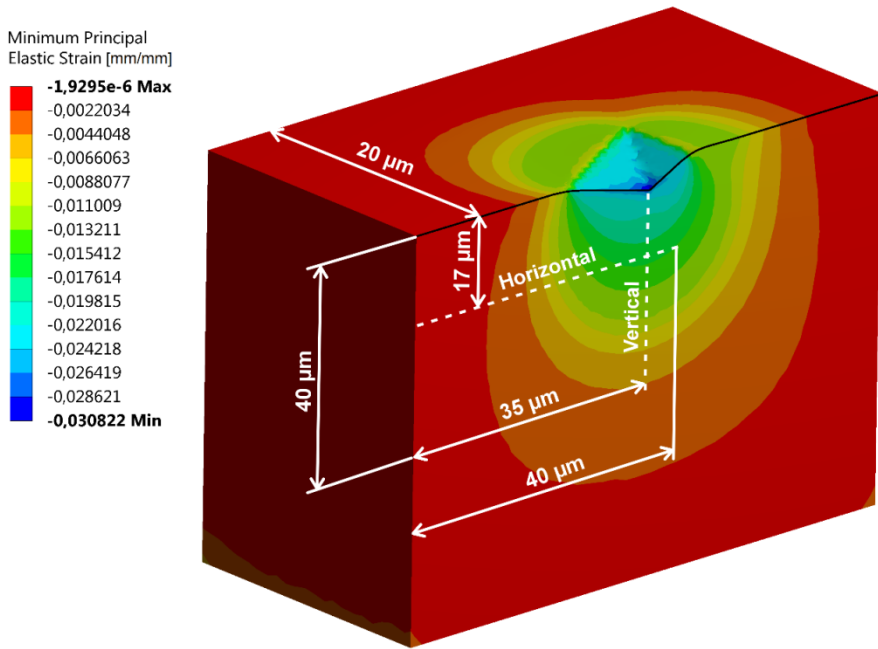


Figure 57:
FEM model of the middle cut of indented sample.

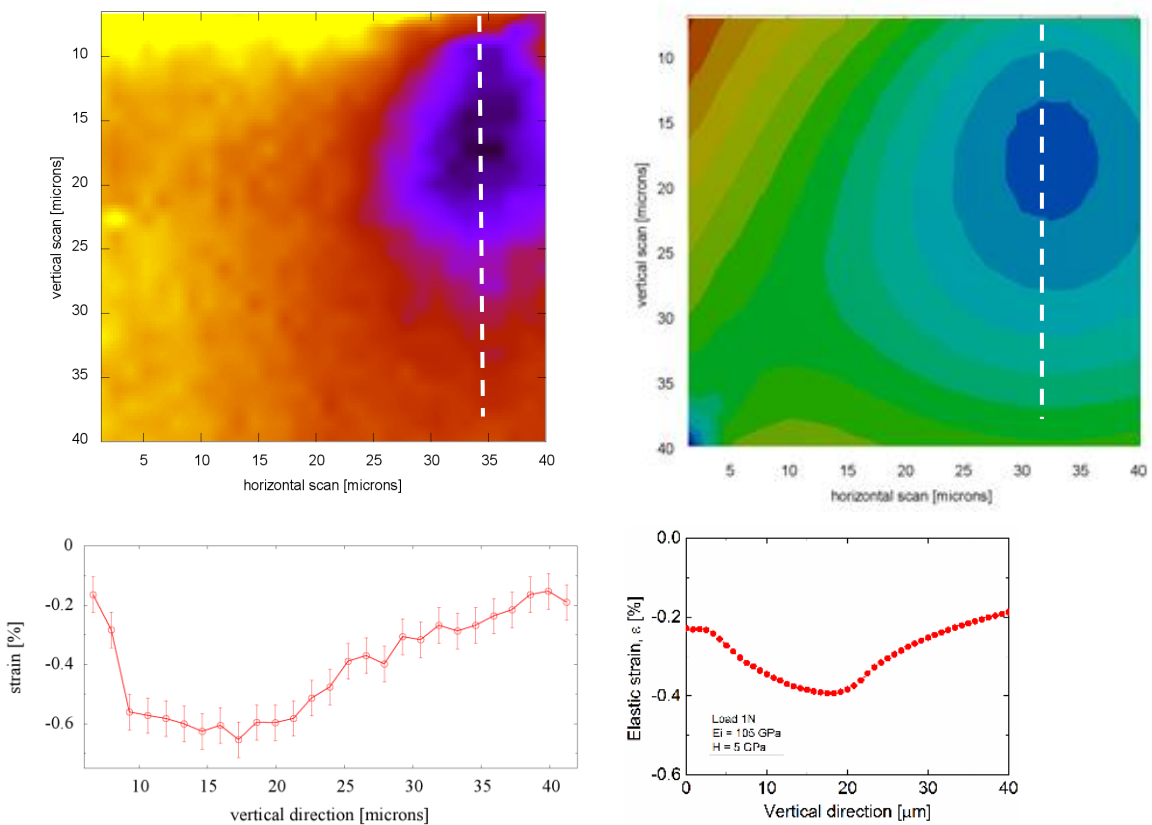


Figure 58: Top: Experimentally obtained strain field. Bottom: Strain values are taken from the position of the white dashes lines.

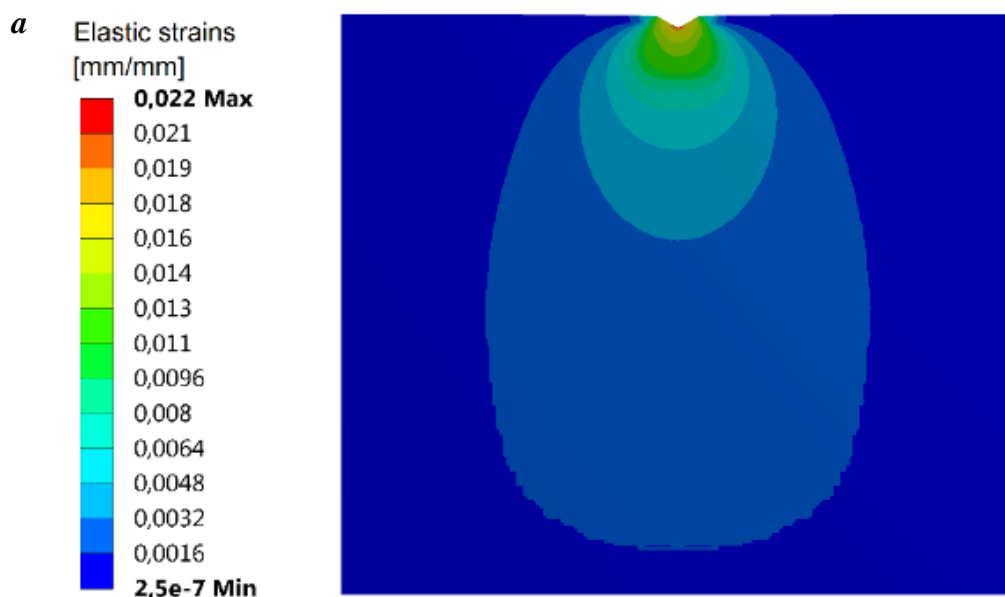
Figure 59: Top: Theoretically obtained strain field. Bottom: Strain values are taken from the position of the white dashes lines.

According to our knowledge, this type of experiment – the connection of nano-indentation and nano-beam, was done on amorphous materials for the first time. Ex-situ experiment on

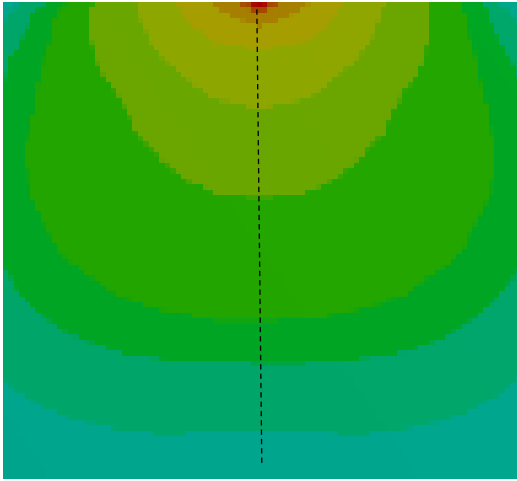
composite materials which combine indentation with X-ray diffraction was for the first time reported by Barabash [83]. Plastic deformation caused by indentation and visualized by X-ray computer tomography was reported by Vertyagina [84] and Mostafavi [85]. Elastically and plastically bent experiments on BMGs were reported by Wu [86] and Bednarcik [87]. A lot of these experiments were done during the last years. This fact also shows that an objective and routine technique which combine mechanical and structural properties is desired.

ESRF ID11

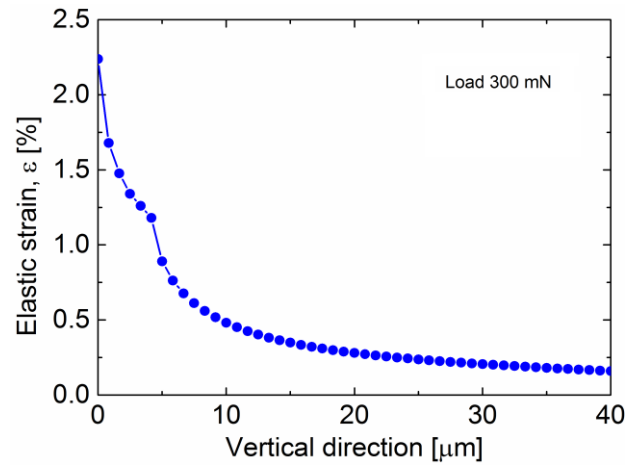
The experiment was done on amorphous $Zr_{53}Cu_{18.7}Ni_{12}Al_{16.3}$ metallic glass in quasi-dynamic mode. Our aim was to observe changes in the strain field as a function of the applied force on the tip. In contrast to the previous in-situ experiment, a wedge indenter was used. The thickness of the sample was 40 micron and the sharp-edge of the indenter had a length of 50 micron, therefore the sharp-edge of the indenter covered the whole thickness of the sample. By this way we reduced the 3D strain projection to a 2D problem. As a result of the data evaluation, three components of the strain tensor were determined, the axial ϵ_{11} , tangential ϵ_{22} and shear γ_{12} components.



b



c



d

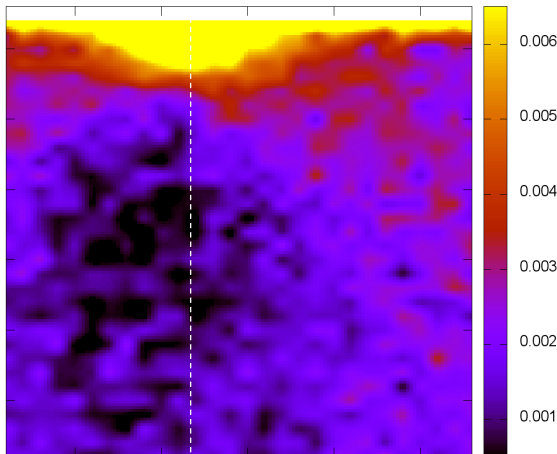


Figure 60 a-d: Data measured at a load of 300 mN

a) FEM 2D map of the strain in an area of 500 x 500 μm.

b) FEM 2D map of the strain in an area of 40 x 40 μm.

c) Position dependence of the strain taken from picture 59-b along the depicted line.

d) Measured 2D map of strains in an area of 40 x 40 μm.

The white dashed line indicates the position of the line in Figure 53.

Figure 60 a shows the calculated 2D map of strain in an area of 500 x 500 μm. For easier comparison *Figure 60 b* shows a zoom on an area of 40 x 40 microns, so we can directly compare the experimentally obtained 2D maps of strains at a load of 300 mN with the theoretically calculated 2D map. The position dependence of strains beneath the indenter along a line is depicted in *Figure 60 c* and *Figure 50*. Measured and modelled dependences are very similar. The main influence of elastic deformation ends 10 microns beneath the indenter tip.

By this experiment we verify the power of this method and we have visualized the evolution of elastic deformation during continuous increasing of load. We have calculated the deformation tensor from each diffraction pattern which contains information about mechanical behaviour of material.

FEM models were not done for all measured loads, only for maximal load 300 mN. Therefore we can only assume that strain fields for other loads will be comparable with measured strain fields.

Conclusion

A lot of mechanical properties of amorphous materials are influenced by strain fields which are created around their inhomogeneities, in our case indents. Nowadays, localized strain information is only available from surface probes such as optical or electron microscopy. But surface and bulk characteristics of materials are in general different. This work gives not only an example of an universal diffraction method for characterizing bulk stress and strain fields, but demonstrates its efficacy by work on a material of current interest in materials engineering.

The initial idea for this work, was to fill the missing piece of knowledge: “what is happening with a material during its deformation”, not after deformation. Therefore, we had to find an experimental system which allows to see the structural changes during controlled deformation. There are of course several different ways how to fulfil this task. In this work we followed the idea of using controlled deformation by employing of indentation. One advantage of this set up is its variability. It is possible to do experiments in-situ at X-ray beamlines, in a SEM and also off-line “on the table”. The set-up includes different diamond-tips (Berkovich, Wedge, Flat-punch) for different aims of experiments. From the X-ray diffraction data we can provide the true strain-picture of the material under investigation. Moreover the strain-pictures could be confirmed by FEM analysis, see *Figures 54, 58 and 59*. It was shown that the strain-picture is dependent on the geometry used in the diffraction measurement. From experiments, in reflection geometry we have information about surface strains (*Figures 21, 28 and 30*) and from experiment in transmission geometry we have information about volume-strains of the samples (*Figure 37-40 and 45-48*).

Our measurements were done on Zr-based bulk metallic glass. The maximal used load was 1 N, every studied composition retains an amorphous state. It means that small changes in

composition do not influence the stability of its structure. We did ex-situ experiments, with the aim to derive information about strains induced into the material. Once we investigated the surface of the sample (reflection geometry) and once the body of the sample (transmission geometry). We showed that a suitable analysis can reveal three (axial, longitudinal and tangential) components of deformation tensor and also its direction. The main benefits of the method used is that such information can not be derived from another standard techniques which deal with mechanical properties of the material, with the expectation of theoretically calculated models. Experimental data were compared with FEM analysis and quantitative and qualitative match was demonstrated, *Figure 53* and *54*. In-situ indentation X-ray experiments done in transmission geometry detected the strain distribution beneath sharp indenters. The similarity between FEM calculations and experiment is displayed in *Figures 57, 58* and *59*. The qualitative and quantitative analysis of our experiments showed that using a Berkovich indenter (three sides) is limiting the interpretation of the results, because it creates a gradient of deformation within the thickness of the material. This is reflected in the fact that the measured strain fields are very similar in shape to the FEM analysis, but the absolute strain values are different, *Figures 57* and *58*. In contrast, using a wedge indenter (which sharp edge covering the full thickness of the sample), the experimentally obtained strain maps and FEM strain maps show the same in shape and also strain values are similar, see *Figure 59*.

This work should built up an optimal set-up for the correlation of mechanical and structural properties of different amorphous materials. Also, the strategy for data evaluation was offered. This method was compared with FEM analysis and very good agreement was achieved. Of course, the procedures established here can equally be used for crystalline materials.

I consider as the biggest success, that we prepared a variable set-up, for different experimental stations and different materials, which can be further developed by scientific user groups.

Zusammenfassung

Strukturuntersuchungen auf der Skala von Nano- und Mikrometern sind die Werkzeuge welche uns erlauben das Verhalten von Materie zu verstehen und neue Stoffe mit verbesserten Eigenschaften zu schaffen. Ein neuer in-situ Ansatz mit nanofokussierter Synchrotronstrahlung zur Charakterisierung und Visualisierung von Verzerrungsfeldern in amorphen Festkörpern, welche durch nano-Indentierung erzeugt werden, wird vorgestellt. Die Verbindung dieser komplementären Methoden bietet die Möglichkeit ein weitgehend vollständiges Bild der atomaren Struktur und der mikroskopischen Verzerrungen der untersuchten Systeme zu gewinnen. Die Methode kombiniert die kontrollierte Verformung des Materials mit kontinuierlicher Beobachtung der mikroskopischen Struktur (mittels Röntgenbeugung). Dadurch können wir mechanische und strukturelle Eigenschaften der Materialien direkt miteinander verbinden. Somit kann ein entscheidender Schritt in der Untersuchung der Sprödigkeit von metallischen Volumengläsern gemacht werden und ein Beitrag zum Verständnis von Deformationsprozessen erbracht werden.

Es wurde eine Reihe von Untersuchungen an verschiedenen Experimentierstationen durchgeführt:

- Ex-situ nano-Indentierungsexperimente haben gezeigt, dass räumlich-aufgelöste Rasteruntersuchungen mit nanometerfokussierten Röntgenstrahlen Mikrometer kleine Eindrücke lokalisieren und den Verzerrungszustand quantitativ beschreiben können.
- In-situ nano-Indentierungsexperimente mit monochromatischer, sub-Mikrometer fokussierter Röntgenstrahlung wurden an metallischen Volumengläsern während des Verformungsprozesse durchgeführt. Feinmaschige Netzscans unterhalb des nano-Eindrucks konnten das elastische Verformungsfeld abbilden. Damit wurde, nach unserem besten Wissen, erstmals die elastische Verzerrung in einem metallischen Volumenglas in Echtzeit unter Belastungsbedingungen beobachtet.

Outlook

Future work will be focused on preparation, optimisation and careful description of the mechanical and structural properties of metallic glasses:

- At atomic structural description is possible for example by structural factor analysis on two- or three- components alloys. Such real space analysis of diffraction data will enable a better understanding of the deformation mechanisms and will provide important structural information and so contribute towards better understanding of deformation processes in such materials.

- Second interesting area, especially for industry, will be to map strain fields induced by different shape-indenter-tips. This means that we get information about how deep into the material the elastic deformation affects the structure and hence properties. This will be valuable for a comparison with analytical models and simulation studies on amorphous metals.

- One of our last in-situ experiment showed that despite the general opinion that relaxation processes in BMG are very slow, we observed relaxation processes in real time. This is also something what would be very interesting to focus attention. Using high brilliance beams relaxation processes in the second or even millisecond range could be observed.

- An important issue is also the optimisation of the set-up for different experiments and different experimental stations. Up to now, the set-up was successfully installed and tested at four experimental stations.

- One of the big challenges in the world of mechanical properties is high temperature nanoindentation. This will be also very interesting to incorporate into the existing set-up and

observe the change of the structure of different materials during controlled deformation (indentation) and controlled heating in the nano-range.

- For data description we want to employ different analysis (for example mentioned PDF, Monte Carlo simulation, ...).

Another interesting outcome of our work is the fact that FEM analysis, under certain conditions, perfectly fits the experimental data. There is a lot of theoretical work about modelling in the nano-range, and also a lot of diffraction experiments in the nano-range. Our analysis shows that time demanding, and very expensive X-ray experiments can be in future gradually replaced by FEM confirmed by few benchmark experiments. However, this will require a lot of effort on both sides.

Ausblick

Weitere Arbeiten werden sich auf die Präparation, Optimierung und sorgfältige Beschreibung der mechanischen und strukturellen Eigenschaften von metallischen Gläsern fokussieren.

- Eine Beschreibung der atomaren Struktur von zwei- oder dreikomponentigen Legierungen kann zum Beispiel durch eine detaillierte Analyse des Strukturfaktors erfolgen. Diese Ortsraumanalyse von Beugungsdaten erlaubt ein besseres Verständnis des Verformungsmechanismus verbunden mit vertieften Strukturinformationen in dieser Substanzklasse.
- Ein weiteres sehr interessantes Feld, speziell für anwendungsorientierte Forschung, ist die Abbildung von Verzerrungsfeldern die durch unterschiedlich geformte Druckspitzen hervorgerufen werden. Das heißt, wir wollen verstehen wie tief die elastische Verformung und damit die Modifikation der mechanischen Eigenschaften in das Material eindringt. Diese Ergebnisse liefern auch wertvolle Vergleichsdaten für analytische Modelle und strukturelle Simulationen von amorphen Metallen.
- Eines unserer letzten in-situ Experimente hat gezeigt, dass, entgegen der verbreiteten Meinung, dass Relaxationen in metallischen Gläsern ein sehr langsamer Prozess sind, wir Verformungen in Echtzeit beobachten konnten. Auch dies eröffnet ein hochinteressantes Forschungsfeld. Mit Hilfe von brillanten Synchrotronstrahlen können Relaxationsprozesse auf der Sekunden oder sogar Millisekunden Skala beobachtet werden.
- Ein weiterer wichtiger Gesichtspunkt betrifft die Optimierung der experimentellen Möglichkeiten und Diffraktionsinstrumente. Bisher konnte der Aufbau an vier Instrumenten erfolgreich eingesetzt werden.

- Eine der großen Herausforderungen auf dem Feld der Forschung an mechanischen Eigenschaften ist die Hochtemperatur-Nano-Indentierung. Eine Erweiterung des Aufbaus in dieser Richtung wäre ebenso von hohem Interesse um die Strukturänderungen während der kontrollierten Verformung bei hohen Temperaturen auf der Nanometerskala zu verfolgen.
- Zur Beschreibung der Daten sollen verschiedene Analysemethoden eingesetzt werden (z.B. PDF Analyse, Monte-Carlo Simulation, ...)

Ein weiteres wichtiges Ergebnis unserer Arbeit ist die Tatsache, dass finite-Elemente-Analysen, unter gut definierten Bedingungen, die experimentelle Daten sehr gut beschreiben können. Es gibt eine Vielzahl theoretischer Arbeiten auf dem Gebiet der Modellierung von Nanostrukturen, ebenso wie eine Vielzahl von Beugungsexperimenten auf der Nanoskala. Unsere Analyse hat gezeigt, dass aufwändige und langwierige Experimente mit Röntgenstrahlung in der Zukunft Schritt für Schritt durch Simulationen ersetzt werden können - die jedoch weiterhin von exemplarischen Experimenten verifiziert werden müssen. Bis dieses Ziel erreicht ist, ist jedoch auf beiden Seiten noch ein weiter Weg zurück zu legen.

Appendix A

Acknowledgement

First and foremost, I offer my sincerest gratitude to my excellent supervisor, Dr. Hermann Franz, who has supported me during my study with his patience and knowledge whilst allowing me the space to work in my own way. One simply could not wish to have a better, understanding and friendlier supervisor which always has given priority to my needs before his duties.

My big thank belongs to Dr. Jozef Bednarčík, Dr. Štefan Michalik and doc. Ondrej Milkovič, they were willing to help me with different troubles not only in my work and study, but also in my privacy. They have been an invaluable help. Their willingness to help me contributed not only to completion of this dissertation thesis but also to non-problematic stay in Hamburg.

I would like to thank you also to Zuzana Konôpková, Hanns-Peter Liermann, Karel Saks, Gaurav Mohanty, Martin Domaracký and the other people from beamlines. Each of this people support my self-realization and had a big contribution to finishing my PhD thesis and smooth running of my study and work.

My last but not the least thank you belongs to Professor Wilfried Wurth and Professor Ralf Roehlsberger which help me with smooth running of my study on University.

Appendix B

Bibliography

- [1] M. Stoica, *Casting and characterization of Fe-(Cr,Mo,Ga)-(P,C,B) soft magnetic bulk metallic glasses* (PhD-Thesis, Technischen Universität Dresden, 2005).
- [2] J. F. Löffler, *Intermetallics* **11**, 529 (2003).
- [3] W. H. Wang, C. Dong, C. H. Sheck, *Materials Science and Engineering R*, **44**, 45 (2004).
- [4] W. Klement, R. Willens, P. Duwez, *Nature* **187**, 869 (1960).
- [5] H. S. Chen, D. Turnbull, *Acta Metall* **17**, 1021 (1969).
- [6] D. Turnbull, *Contemporary Physics* **10**, 437 (1969).
- [7] H. S. Chen, *Acta Metall* **22**, 1505 (1974).
- [8] H. W. Kui, A. L. Greer, D. Turnbull, *Apply Physics Letter* **45**, 615 (1984).
- [9] A. Inoue, T. Zhang, T. Masumoto, *Materials Transactions JIM* **30**, 965 (1989).
- [10] A. Inoue, A. Kato, T. Zhang, S. G. Kim, T. Masumoto, *Materials Transactions JIM* **32**, 609 (1991).
- [11] T. Zhang, A. Inoue, T. Masumoto, *Materials Transactions JIM* **32**, 1005 (1991).
- [12] A. Peker, W. L. Johnson, *Apply Physics Letter* **63**, 2342 (1993).
- [13] A. Inoue, N. Nishiyama, H. Kimura, *Materials Transactions JIM*, **38**:179-183, 1997.
- [14] F. Q. Guo, S. J. Poon, G. J. Shiflet, *Apply Physics Letter* **84**, 37 (2003).
- [15] J. Pu, J. F. Wang, J. Z. Xiao, *Nonferrous Metals Society* **13**, 1056 (2003).
- [16] M. B. Tang, D. Q. Zhao, M. X. Pan, W. H. Wang, *Chinese Physics Letter* **21**, 901 (2004).
- [17] A. Inoue, W. Zhang, *Materials Transactions* **45**, 584 (2004).

- [18] D. Xu, B. Lohwongwatana, G. Duan, W. L. Johnson, C. Garland, *Acta Materialia* **52**, 2621 (2004).
- [19] A. Inoue, *Acta Materialia* **48**, 279 (2000).
- [20] A. L. Greer, *Nature* **366**, 303 (1993).
- [21] X. Xiao, F. Shoushi, W. Guoming, H. Qin, D. Yuanda, *Journal of Alloys and Compounds* **376**, 145 (2004).
- [22] M. Telford, *Materials Today* **7**, 36 (2004).
- [23] M. H. Cohen, D. Turnbull, *The Journal of Chemical Physics* **31**, 1164 (1959).
- [24] R. Schilling, *Collective Dynamics of Nonlinear and Disordered Systems* (Springer, Berlin, 2003).
- [25] G. Adam, J. H. Gibbs, *The Journal of Chemical Physics* **43**, 139 (1965).
- [26] A. Inoue, A. Takeuchi, *Materials Transactions: The Japan Institute of Metals* **43**, 1892 (2002).
- [27] Y. He, C. E. Price, S. J. Poon, *Philosophical Magazine Letter* **70**, 371 (1994).
- [28] Y. Li, S. C. Ng, Z. P. Lu, Y. P. Feng, K. Lu, *Philosophical Magazine Letters* **78**, 213 (1998).
- [29] B. C. Wei, W. Löser, L. Xia, S. Roth, M. X. Pan, W. H. Wang, J. Eckert, *Acta Materialia* **50**, 4357 (2002).
- [30] L. Q. Xing, J. Eckert, W. Löser, S. Roth, L. Schult, *Journal of Applied Physics* **88**, 3565 (2000).
- [31] A. Inoue, T. Zhang, A. Takeuchi, W. Zhang, *Materials Transactions Japan Institute of Metals* **37**, 636 (1996).
- [32] B. C. Wei, W. H. Wang, M. X. Pan, B. S. Han, *Physical Review B* **64**, 012406 (2001).
- [33] B. C. Wei, Y. Zhang, Y. X. Zhuang, D. Q. Zhao, M. X. Pan, W. H. Wang, W. R. Hu, *Journal of Applied Physics* **89**, 3529 (2001).
- [34] A. Inoue, *Trans Tech Publications* **1**, 10 (1998).
- [35] A. Inoue, T. Zhang, A. Takeuchi, *Materials Science Forum* **269**, 855 (1998).
- [36] J. Xu, M. H. Manghnani, *Physical Review B* **45**, 640 (1992).
- [37] R. C. Purdom, E. W. Prohofsky, *Physical Review B* **2**, 551 (1970).
- [38] M. Grimsditch, K. E. Gray, R. Bhadra, R. T. Kampwirth, L. E. Rehn, *Physical Review B* **35**, 883 (1987).
- [39] Z. Bian, R. J. Wang, M. X. Pan, D. Q. Zhao, W. H. Wang, *Advanced Materials* **15**, 616 (2003).

- [40] N. V. Steenberge, *Study of structural changes of Zr-based bulk metallic glasses upon annealing and deformation treatments* (PhD-Thesis, Universitat Autònoma de Barcelona, 2008).
- [41] INSTRON Deutschland GmbH, www.instron.de.
- [42] ISO – International Organization for Standardization, www.iso.org.
- [43] Z. Y. Shen, G. Y. Chen, Y. Zhang, X. J. Yin, *Physical Review B* **39**, 2714 (1989).
- [44] W. K. Wang, H. Iwasaki, K. Fukamichi, *Journal of Material Science* **15**, 2701 (1980).
- [45] W. H. Wang, *Journal of Metastable and Nanocrystalline Materials* **73**, 15 (2003).
- [46] W. H. Wang, D. W. He, D. Q. Zhao, Y. S. Yao, M. He, *Applied Physics Letters* **75**, 2770 (1999).
- [47] J. Zhang, K. Q. Qiu, A. M. Wang, H. F. Zhang, M. X. Quan, Z. Q. Hu, *Journal of Materials Research* **17**, 2935 (2002).
- [48] W. H. Wang, T. Okada, P. Wen, X. L. Wang, M. X. Pan, D. Q. Zhao, W. Utsumi, *Physical Review B* **68**, 184105 (2003).
- [49] J. Z. Jiang, Y. X. Zhuang, J. Saida, A. Inoue, *Physical Review B* **64**, 094208 (2001).
- [50] J. Z. Jiang, K. Saksl, H. Rasmussen, T. Watanuki, N. Ishimatsu, O. Shimomara, *Apply Physics Letter* **79**, 1112 (2001).
- [51] Liquidmetal Technologies, <http://liquidmetal.com>.
- [52] NASA's Genesis spacecraft, <http://genesismission.jpl.nasa.gov/>.
- [53] TAG Heuer Watch, www.tagheuer.com.
- [54] W. L. Johnson, *Metals and Alloys* **1**, 383 (1996).
- [55] NASA, www.nasa.gov
- [56] DePuy Orthopaedics, Inc, www.depuysynthes.com.
- [57] Y. Kawamura, Y. Ohno, *Scripta Materialia* **45**, 127 (2001).
- [58] Y. Kawamura, Y. Ohno, *Scripta Materialia* **45**, 279 (2001).
- [59] Y. Kawamura, Y. Ohno, *Materials Transactions* **42**, 2476 (2001).
- [60] Y. Kawamura, S. Kagao, Y. Ohno, *Materials Transactions* **42**, 2649 (2001).
- [61] Y. Kawamura, T. Shoji, Y. Ohno, *Journal of Non-Crystalline Solids* **317**, 152 (2003).
- [62] C. H. Wong, C. H. Shek, *Scripta Materialia* **49**, 393 (2003).
- [63] A. C. Fischer-Cripps, *Nanoindentation* (Springer New York, 2011).
- [64] J. F. Beringues, *Metallic glasses and derived composite materials: a correlation between microstructure and mechanical properties* (PhD-Thesis, Universitat Autònoma de Barcelona, 2012).

- [65] S. Fluegge, *Principles of Classical Mechanics and Field Theory* (Springer Berlin Heidelberg 1960).
- [66] G. P. Nikishov, *Introduction to the Finite Element Method* (University of Aizu, Japan, 2004)
- [67] F. R. Elder, A. M. Gurewitsch, R. V. Langmuir, H. C. Pollock, *Physical Review* **71**, 829 (1947).
- [68] Deutsches Elektronen Synchrotron, www.desy.de.
- [69] J. Als-Nielsen, D. Mcmorrow. *Elements of Modern X-ray Physics* (John Wiley & Sons, Ltd, 2011).
- [70] A. P. Hammersley, S. O. Svensson, A. Thompson, *Nuclear Instruments and Methods in Physics Research Section A* **346**, 312 (1994).
- [71] H.F.Poulsen, J.A.Wert, J.Neuefeind, V.Honkimäki, M.Daymond, *Nature Materials* **4**, 33 (2004).
- [72] A. R. Yavari, M. Tonegaru, N. Lupu, A. Inoue, E. Matsubara, G. Vaughan, Å. Kwick, W. J. Botta, *Materials Research Society Symposium Proceedings* **306**, 203 (2004).
- [73] G. E. Dieter, D. Bacon, *Mechanical Metallurgy* (McGraw-Hill Book Co, 1988).
- [74] The European Synchrotron, www.esrf.eu.
- [75] C. G. Schroer, P. Boye, J. M. Feldkamp, J. Patommel, D. Samberg, A. Schropp, A. Schwab, S. Stephan, G. Falkenberg, G. Wellenreuther, N. Reimers, *Nuclear instruments & methods in physics research A* **616**, 93 (2010).
- [76] T.C.Hufnagel, R.T.Ott, J.Almer, *Physical Review B* **73**, 064204 (2006).
- [77] H.-P. Liermann, Z. Konôpková, W. Morgenroth, K. Glazyrin, J. Bednarcik, E. E. McBride, S. Petitgirard, J. T. Delitz, M. Wendt, Y. Bican, A. Ehnes, I. Schwark, A. Rothkirch, M. Tischer, J. Heuer, H. Schulte-Schrepping, T. Kracht and H. Franz, *Journal of synchrotron radiation* **22**, 22 (2015).
- [78] A.-C. Dippel, H.-P. Liermann, J. T. Delitz, P. Walter, H. Schulte-Schrepping, O. H. Seeck and H. Franz, *J. Synchrotron Rad.* **22**, 675 (2015).
- [79] X.H. Lin, W.L. Johnson, W.K. Rhim, *Mater. Trans. JIM* **5**, 473 (1997).
- [80] S.C. Glade, R. Busch, D.S. Lee, W.L. Johnson, R.K. Wunderlich, H. J. Fecht, *J. Appl. Phys.* **87**, 7242 (2000).
- [81] Z. Bian, M.X. Pan, Y. Zhang, W.H. Wang, *Appl. Phys. Lett.* **81**, 4739 (2002).
- [82] Y. Sun, Y. Huang, H. Fand, F. Liu, J. Shen, J. Sun, J. Chene, *Journal of Non-Crystalline Solids* **406**, 144 (2014).

- [83] R. I. Barabash, H. Bei, Y. F. Gao, and G. E. Ice, *Acta Mater.* 58, 6784 (2010).
- [84] Y. Vertyagina, M. Mostafavi, C. Reinhard, R. Atwood, and J. Marrow, *J. Eur. Ceram. Soc.* 34, 3127 (2014).
- [85] M. Mostafi, D. M. Collins, B. Cai, R. Bradley, R. C. Atwood, C. Reinhard, X. Jiang, M. Galano, P. D. Lee, and T. J. Marrow, *Acta Mater.* 82, 468 (2014).
- [86] Y. Wu, A. D. Stoica, Y. Ren, D. Ma, Y. F. Gao, and H. Bei, *Intermetallics* 67, 132 (2015).
- [87] J. Bednarcik, L. Chen, X. Wang, J. Jiang, and H. Franz, *Metall. Mater. Trans. A* 43, 1558 (2012).

Appendix C

Nomenclature

T_g	glass transition temperature
T_m	melting temperature
T_{rg}	reduced glass transition temperature
T_x	crystallization temperature
T_{liq}	liquidus temperature
γ	glass forming ability parameter
l_o	initial length
A	cross-section, projected area
P	applied load
E	(elastic) Young's modulus
σ	stress or strength
ε	strain
Δl	relative elongation
σ_e	yield strength
σ_f	fracture strength
ε_e	yield strain
ε_f	fracture strain
h_c	contact depth penetration
ξ	angle describing the sharpness of indenters-diamond-tips
a	length describing indenter-diamond-tip
P	load

E^*	indentation elastic modulus
H	hardness
d	dimension; interatomic distance
d_0	initial dimension
d_σ	dimension at load
h_{max}	depth from the original specimen surface at maximum load
h_r	depth of the residual impression
h_{rc}	depth of the residual impression for an equivalent punch
h_c	elastic displacement for an equivalent punch
P_{max}	maximal load
h_e	elastic displacement
$d\mathbf{r}$	volume element
\mathbf{r}	position vector
\mathbf{k}	wavevector
ϕ_{in}	incident wave
λ	wavelength
ϕ_{out}	outgoing wave
θ	half scattering angle
\mathbf{Q}	scattering vector
$f_0(\mathbf{Q})$	atomic form factor
$F^{mol}(\mathbf{Q})$	molecule form factor
$\rho(r)$	number density
$A(\mathbf{Q})$	scattering amplitude
Z	atomic number
$pV(2\theta)$	pseudo-Voight function
η	mixing parameter
$L(2\theta)$	Lorentzian function
$G(2\theta)$	Gauss function
α	intensity of Gauss function
β	intensity of Lorentzian function
δ_{hkl}	interplanar distance
Γ	full width at half maximum
$\langle e \rangle$	microstrains

$I(Q)$	scattered intensity
ε_{11}	longitudinal component of deformation tensor
ε_{22}	transversal component component of deformation tensor
γ_{12}	planar component component of deformation tensor
n	integer number

Appendix D

Brief user manual for SEM

ALEMNIS Nanoindenter

In this section, we would like to briefly introduce the ALEMNIS SEM Nanoindenter and its software interface. The indenter has a microscope installed on it that allows performing tip-to-optic calibration. This enables performing site-specific indents on the area of interest. We describe the most important steps for calibrating the indenter and performing experiments. Detailed manual describing each component of the indenter and its functional ability can be found online at: <http://www.alemnis.ch/products/situ-indenter/>, AMICS manual.

Figure a shows the picture of all components needed for setting up the ALEMNIS SEM nanoindenter. The indenter is normally stored in the black box, shown in *Figure b*, that has adequate cushion for protecting the indenter. A more detailed view of the most important parts from a usage point of view are indentation head/tip holder (*Figure b - part 2*) and sample holder (*Figure b - part 4*). The camera (*Figure b - part 1*) is removable. The microscope is necessary to position the tip on the area/site of interest. It can be removed when integrating the indenter in an SEM. The indenter can also be used as a table-top device for normal hardness and modulus measurements on the samples.



Figure a:

- 1- ALEMNIS SEM nanoindenter
- 2- SmarAct
- 3- National Instruments compactDAQ – NI cDAQ 9174
- 4- Noliac – Single Channel Dynamic Driver for Piezoelectric Actuators

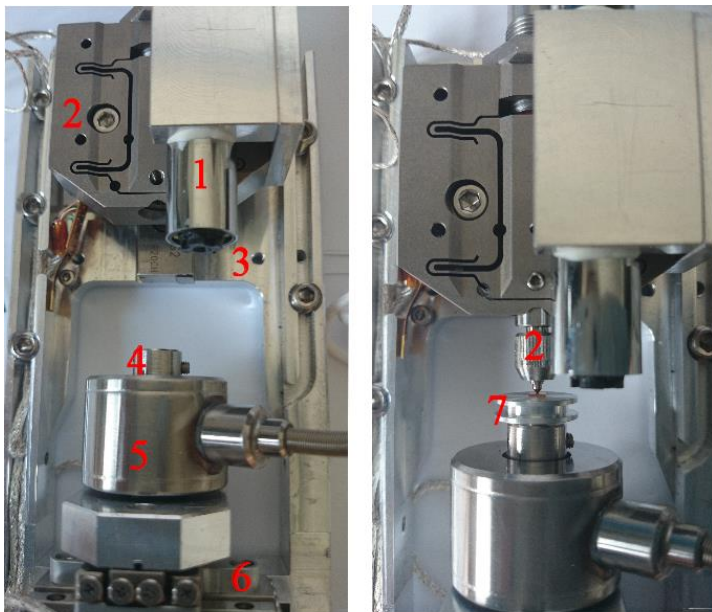


Figure b:

- 1- camera
- 2- indentation head/ tip holder
- 3- Z axis of indenter (up-down)
- 4- sample holder
- 5- load cell
- 6- XY axes of indenter (left-right, forward-backward)
- 7- aluminum sample holder



The software interface for controlling the indenter has been made in LabView® which allows users to incorporate their own changes to the software. The modular nature of both the instrumentation and the software makes it attractive for customizing experiments. Now, we would like to describe how to perform normal experiments using the instrument. Cases that

require specific positioning of the indenter on certain areas of the sample need microscope installation. Each of these experiments consists of calibrating the camera for tip to optic calibration before proceeding with the indents. The tip-to-optic calibration calculates the offset between the sample position beneath the indenter and the microscope. By performing this calibration, the desired area under the microscope can be accurately indented. This minimizes the offset between the desired and actual indentation position.

Before proceeding, the indenter needs to be connected and operationalized. There are 3 main cables that come out of the indenter: (a) load cell sensor, (b) piezo sensor and (c) piezo driver/actuator. These connections are adequately labelled to avoid mix ups. The piezo and load cell sensor cables are connected to the NI cDAQ module. The piezo actuator is connected to the Noliac amplifier. The Noliac amplifier is, in turn, connected to the NI cDAQ module. In terms of interfacing these with the computer, two USB cables are connected to the CPU of the indenter computer. After connecting and switching on all components of indenter and computer, the AMICS – Alemnis Micro Indenter Control Software AMICS can be started.



Figure c: Introductory screen of AMICS

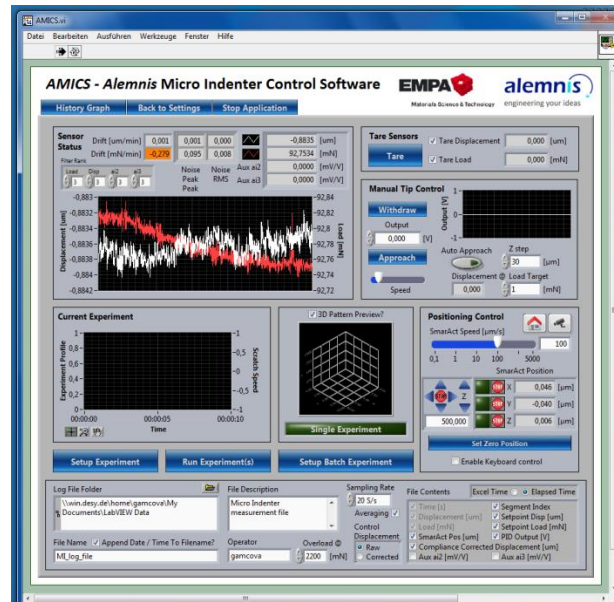


Figure d: Working screen in AMICS software.

The introductory screen is shown in Figure c. The input/output channels should be selected from the dropdown menu. The limits for load and displacement as well as compliance of

indenter can be added. By default, the axes will be defined. In case they are not, they can be selected from the drop down menu. When the rectangular button “SmarAct Connected” is green, all translation stages (SmarAct stages) are operational and connected to the software. Click on “Proceed to Setup” to proceed to the next screen which deals with setting up the experiments. This is shown in *Figure d*.

Here we can see the actual Time versus Displacement/Load graph (left-top window) and we can set/run the experiment in the window “Current Experiment” by pressing the button “Setup/Run Experiment”. The window “Manual Tip Control” is used for approaching the tip to the surface of the sample. If the tip is very high above the sample, it can be moved down manually. When the tip is close to the sample surface, it is better to perform an auto approach to avoid crashing the tip to the sample. By pressing the button “Auto Approach”, the indenter-head automatically starts to move towards the sample surface. The “Auto Approach” functionality works by extending the tip to the maximum displacement using the piezo stack and seeing if it touches the sample. The sample touching criteria is decided by the “load” cut off decided by the user. If it does not touch the sample surface, it moves the indenter head down using the SmarAct stage by a certain value (by default it is 30 microns). Since the range of piezo movement is ~ 36 microns (~40 microns), it is advisable to use “z-step” size less than 35 microns. The rate of tip sample approach using the piezo can be changed as well by changing the “speed”. Its movement is controlled by the speed of Z-axis-movement (*Figure b*) of indenter-head during the approaching the surface, “Speed” and the “Z step” which is the displacement-step between two approaches. When the indenter-tip registers the surface of the sample, it immediately stops all movements and retracts back to 0V. The actual distance between sample surface and indenter-tip can be calculated by subtracting the value for current displacement (the value for displacement in left right window) from “Displacement @ Load Target”.

The window “Positioning Control” is using for manual control of the indenter (the sample-stage is rigid). One can manipulate the head of the indenter using blue triangles about desired step. In this window is a small icon with camera (right-top). This icon transfers the user to the calibration section of software, Embarked Microscope Simple Vision. Before starting the calibration procedure, we have to initialize XZY stage of indenter, which means that indenter head will find its zero-position. We are doing it manually, using SmarAct (*Figure a – part 2*): Menu – Calibration – Initialize X/Y/Z – For/Backward.

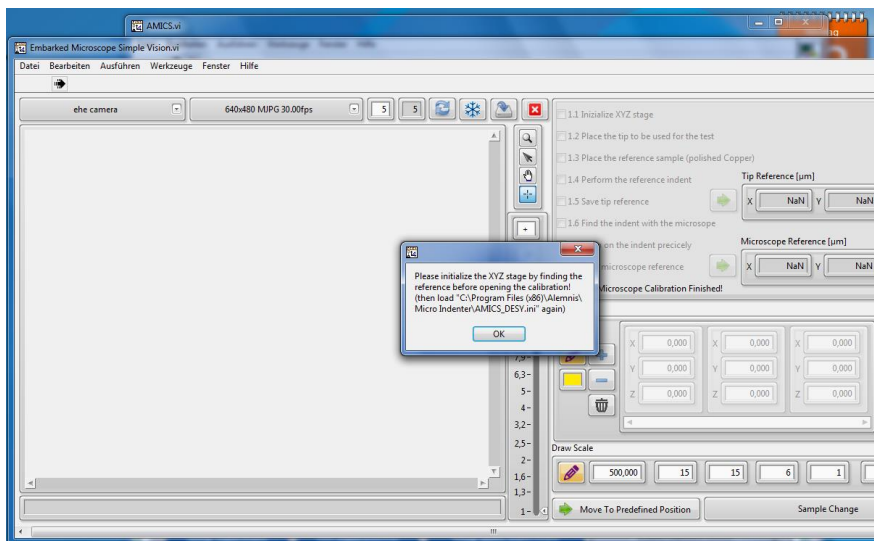


Figure e
The calibration section of software, Embarked Microscope Simple Vision.

After initializing the XZY stage, we can start with calibration according to sequences 1.1 – 1.9 indicated in calibration section of software, Figure f. The part 1.1 is unchecked, Figure f. In second part, 1.2, we have to place indenter-diamond-tip (Figure g) to the indenter head/tip holder (Figure b – part 2). In third part, 1.3, we have to place reference sample, a well polished copper fixed on the aluminum sample holder (Figure g) to the sample holder (Figure b – part 4). After these, the indenter is ready for performing reference indent, part 1.4. In this part we go back to AMICS section of software and we perform manually one indent. We move the head of indenter above the polished Copper (using panel “Positioning Control”), we press the blue button “Tare” (in panel “Tare Sensor”) for reset the Displacement and Load values, and we press the button “Approach” (in the panel “Manual Tip Control”). When the indenter approaches the sample, we make the reference indent by programming an indentation profile using “Setup Experiment”. This completes step 1.4 in the calibration procedure.

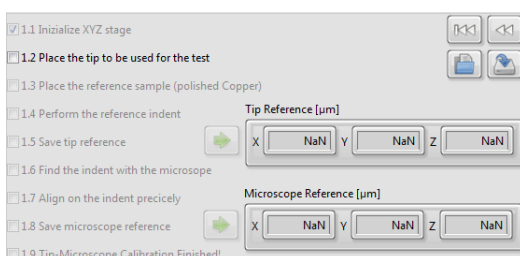


Figure f: Camera calibration sequence. After completion of individual parts, 1.1 - 1.9 the



Figure g: left – diamond tip and polished Copper on the aluminium sample holder; middle and right – tip-holder.

calibration is completed.

After indentation, we go back to the calibration part of software Embarked Microscope Simple Vision and here we save the XYZ coordinates of reference indent, part 1.5. Now in part 1.6, we have to find the reference indent with the microscope. From the drop down menu “Sample Change” (right-down), we pick up the option “Microscope Change” and we press the button “Move To Predefined Position”. The software will ask if we really want to drive from microscope to the position in reference indent, *Figure h*.



Figure h:
Software announcement about changing the position of the camera and indentation-head.

Using different graphically tools on the left part of this section of the software, we align the indent with the position of the green cross, part 1.7. For pillar compression using flat punch, circular cross hair can also be used. Then we save microscope references, part 1.8 and we see that the Tip Microscope Calibration Finished, part 1.9.

Now we can proceed to the experiment. We have to change reference sample for real sample. We click on the drop down menu from right-bottom button, we pick up the option “Sample Change” and press “Move To Predefined Position”. The sample will move to one corner making it easy to change the sample. From the drop down menu button, we pick up the option “Sample Change” and press “Move To Predefined Position”. The sample holder will change its position and we can see the sample in the microscope window. The contrast can be aligning by changing the luminous intensity of camera and by changing the distance between the camera and sample surface. Now, we have to decide where we want to do indent. When we find desired place for indentation we have to move the indentation head/tip holder above the sample (roll up the right-bottom button; pick up the option “Sample Change” and press “Move To Predefined Position”). At this point the indentation head/tip holder is above the sample and we can set the experiment.

For setting up the experiment, we go back to AMICS screen to the panel “Current Experiment” and by pressing “Setup Experiment” we see the part of software dedicated for setting the experiment, MI_ExperimenSetup, *Figure i* and *Figure j*. Here, in the window “Experimental Setup” we can decide how type of experiment we want to do. There are several options, two main options are “Load Control” and “Displacement Control”. For each type of control we have different options or setting of experiment which appear after choosing the type of control. Then in the panel “Segment Parameters” and using blue buttons bellow this panel, we set up the experiment. Experiment profile and its duration will be displayed in the bottom graphical window. When we press the blue button “FINISH”, we are back in AMISC screen, *Figure j*.

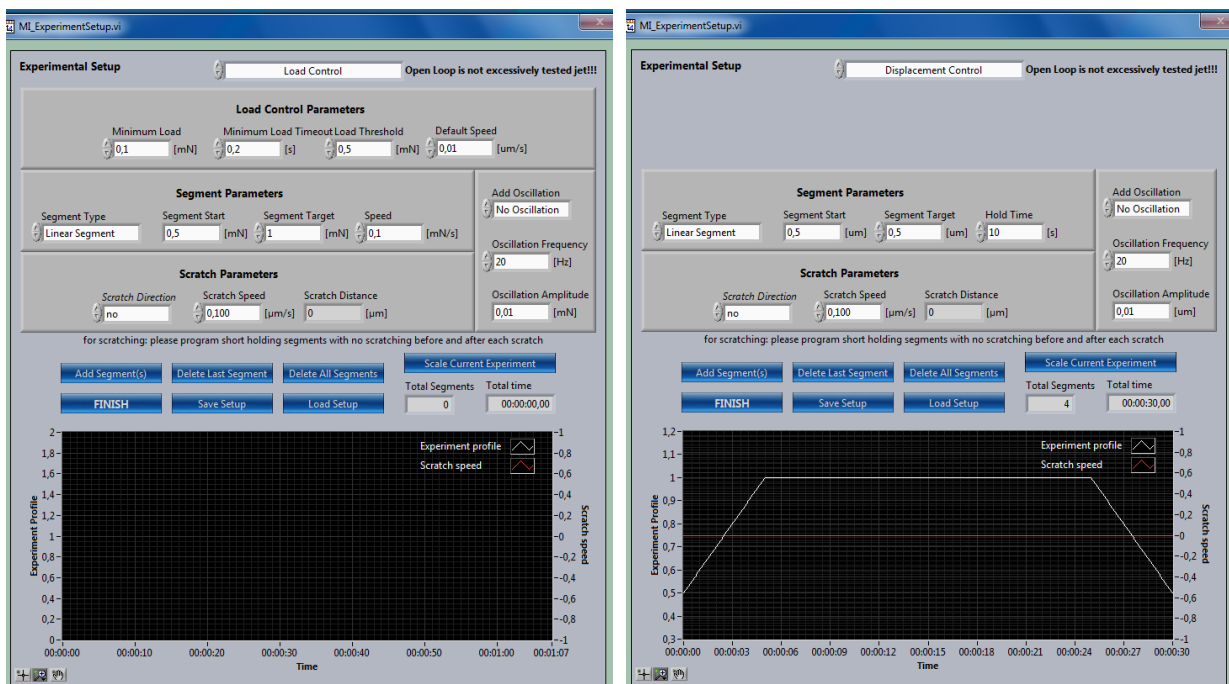


Figure i: The experiment setting of software, Figure j: The experiment setting of software after MI_ExperimenSetup.

When we press the button “Run Experiment(s)” we go to the part of software “In Situ Indenter Controller” responsible for control of the experiment, *Figure k*. In this section of software we can also see the current state of the experiment in the two graphical windows.

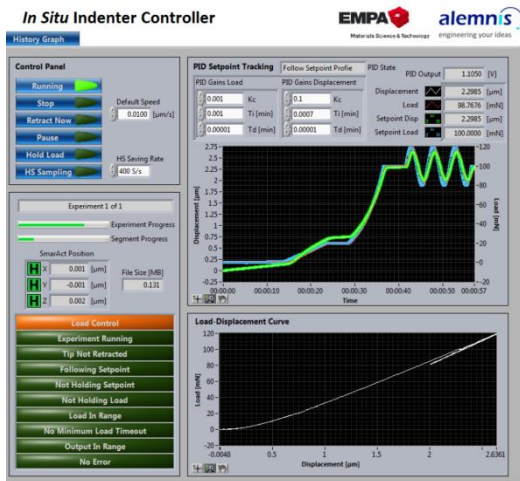


Figure k:
The experimental screen of software, In Situ Indenter Controller.

These are the main steps on how to use the ALEMNIS SEM nanoindenter for experiments.